Multiwavelength and Multimessenger emission from Active Galactic Nuclei

Contents

1 Topics

- High energy gamma-rays from active galactic nuclei
- High energy neutrinos from blazars
- High energy emission from gamma-ray bursts

1.1 ICRANet participants

- Sahakyan Narek
- Gasparyan Sargis
- Israyelyan Davit
- Harutyunyan Gevorg

1.2 Students

- Khachatryan Mher
- Vazgen Vardanyan
- Manvel Manvelyan
- Gayane Ghazaryan

1.3 Ongoing collaborations

- Damien Begue (Bar Ilan University, Israel)
- Razmik Mirzoyan (Max Planck Institute for Physics, Munich, Germany)

- Paolo Giommi (ASI Science Data Center)
- Ulisses Barres de Almeida (Centro Brasileiro de Pesquisas Fisicas - CBPF/MCT)
- Bernardo Fraga (Centro Brasileiro de Pesquisas Fisicas - CBPF)
- Karlica Mile (Nova Gorica)

2 Brief description

The main scientific activities of our group are focused on X-ray and gamma-ray Astrophysics, as well as Astroparticle Physics. We use the results from data analysis conducted with the Swift UVOT/XRT, NuStar, Chandra, and Fermi LAT telescopes to investigate particle acceleration and emission processes in various classes of active galactic nuclei. This analysis of available data enables us to explore emission processes and relativistic outflows in the most extreme regimes, ranging from keV to TeV.

Below, we present several abstracts from papers published in 2023, which also include collaborations with MAGIC.

- Origin of multiwavelength emission from flaring high redshift blazar PKS 0537-286

The high redhsift blazars powered by supermassive black holes with masses exceeding $10^9\ M_\odot$ have the highest jet power and luminosity and are important probes to test the physics of relativistic jets at the early epochs of the Universe. We present a multi-frequency spectral and temporal study of high redshift blazar PKS 0537-286 by analyzing data from Fermi LAT, NuSTAR Swift XRT and UVOT. Although the time averaged γ-ray spectrum of the source is relatively soft (indicating the high-energy emission peak is below the GeV range), several prominent flares were observed when the spectrum hardened and the luminosity increased above $10^{49}\ erg\ s^{-1}$. The X-ray emission of the source varies in different observations and is characterised by a hard spectrum ≤ 1.38 with a luminosity of $> 10^{47}\ erg\ s^{-1}$. The broadband spectral energy distribution in the quiescent and flaring periods was modeled within a one-zone leptonic scenario assuming different locations of the emission region and considering both internal (synchrotron radiation) and external (from the disk, broad-line region and dusty torus) photon fields for the inverse Compton scattering. The modeling shows that the most optimistic scenario, from the energy requirement point of view, is when the jet

energy dissipation occurs within the broad-line region. The comparison of the model parameters obtained for the quiescent and flaring periods suggests that the flaring activities are most likely caused by the hardening of the emitting electron spectral index and shifting of the cut-off energy to higher values.

- A multi-messenger study of the blazar PKS 0735+178: a new major neutrino source candidate

The blazar PKS 0735+178 is possibly associated with multiple neutrino events observed by the IceCube, Baikal, Baksan, and KM3NeT neutrino telescopes while it was flaring in the γ-ray, X-ray, ultraviolet and optical bands. We present a detailed study of this peculiar blazar to investigate the temporal and spectral changes in the multi-wavelength emission when the neutrino events were observed. The analysis of Swift-XRT snapshots reveal a flux variability of more than a factor 2 in about 5×10^3 seconds during the observation on December 17, 2021. In the γ-ray band, the source was in its historical highest flux level at the time of the arrival of the neutrinos. The observational comparison between PKS 0735+178 and other neutrino source candidates, such as TXS 0506+056, PKS 1424+240, and GB6 J1542+6129, shows that all these sources share similar spectral energy distributions, very high radio and γ-ray powers, and parsec scale jet properties. Moreover, we present strong supporting evidence for PKS 0735+178 to be, like all the others, a masquerading BL Lac. We perform comprehensive modelling of the multiwavelength emission from PKS 0735+178 within one-zone lepto-hadronic models considering both internal and external photon fields and estimate the expected accompanying neutrino flux. The most optimistic scenario invokes a jet with luminosity close to the Eddington value and the interactions of $\sim$ PeV protons with an external UV photon field. This scenario predicts ~ 0.067 muon and antimuon neutrinos over the observed 3-week flare. Our results are consistent with the detection of one very-high-energy neutrino like IceCube-211208A.

- Quasi-periodic oscillations in the γ-ray light curves of bright active galactic nuclei

The detection of quasi-periodic oscillations (QPOs) in the light curves of active galactic nuclei (AGNs) can provide insights on the physics of the supermassive black holes (SMBHs) powering these systems, and could represent a

signature of the existence of SMBH binaries, setting fundamental constraints on SMBH evolution in the Universe. Identification of long term QPOs, with periods of the order of months to years, is particularly challenging and can only be achieved via all-sky monitoring instruments that can provide unbiased, continuous light curves of astrophysical objects. The Fermi LAT satellite, thanks to its monitoring observing strategy, is an ideal instrument to reach such a goal, and we aim to identify QPOs in the γ-ray light curves of the brightest AGNs within the Fermi LAT catalog. We analyze the light curves of the thirty-five brightest Fermi LAT AGNs, including data from the beginning of the Fermi mission (August 2008) to April 2021, and energies from 100 MeV to 300 GeV. Two time binnings are investigated, 7 and 30 days. The search for quasi-periodic features is then performed using the continuous wavelet transform. The significance of the result is tested via Monte Carlo simulations of artificial light curves with the same power spectral density and probability distribution function as the original light curves. The significances are then corrected for the look-elsewhere effect and provided as post-trials. We identify twenty-four quasars with candidate QPOs. Several of our candidates coincide with previous claims in the literature: PKS 0537-441, S5 0716+714, Mrk 421, B2 1520+31, and PKS 2247-131. All our candidates are transient. The most significant multi-year QPO, with a period of about 1100 days, is observed in the quasar S5 1044+71, and is reported here for the first time.

- Gradient boosting decision trees classification of blazars of uncertain type in the fourth Fermi-LAT catalog

The deepest all-sky survey available in the γ-ray band - the last release of the Fermi-LAT catalogue (4FGL-DR3) based on the data accumulated in 12 years, contains more than 6600 sources. The largest population among the sources is blazar subclass - 3743, 60.1% of which are classified as BL Lacertae objects (BL Lacs) or Flat Spectrum Radio Quasars (FSRQs), while the rest are listed as blazar candidates of uncertain type (BCU) as their firm optical classification is lacking. The goal of this study is to classify BCUs using different machine learning algorithms which are trained on the spectral and temporal properties of already classified BL Lacs and FSRQs. Artificial Neural Networks, *XGBoost* and *LightGBM* algorithms are employed to construct predictive models for BCU classification. Using 18 input parameters of 2219 BL Lacs and FSRQs, we train (80% of the sample) and test (20%) these algorithms and find

that *LightGBM* model, state-of-the-art classification algorithm based on gradient boosting decision trees, provides the highest performance. Based on our best model, we classify 825 BCUs as BL Lac candidates and 405 as FSRQ candidates, however, 190 remain without a clear prediction but the percentage of BCUs in 4FGL is reduced to 5.1%. The γ-ray photon index, synchrotron peak frequency, and high energy peak frequency of a large sample are used to investigate the relationship between FSRQs and BL Lacs (LBLs, IBLs, and HBLs).

- Multi-messenger characterization of Mrk 501 during historically low X-ray and γ-ray activity

We study the broadband emission of Mrk 501 using multi-wavelength observations from 2017 to 2020 performed with a multitude of instruments, involving, among others, MAGIC, *Fermi*-LAT, *NuSTAR*, *Swift*, GASP-WEBT, and OVRO. Mrk 501 showed an extremely low broadband activity, which may help to unravel its baseline emission. Nonetheless, significant flux variations are detected at all wavebands, with the highest occurring at X-rays and very-high-energy (VHE) γ-rays. A significant correlation ($>3\sigma$) between X-rays and VHE γ-rays is measured, supporting leptonic scenarios to explain the variable parts of the emission, also during low activity. This is further supported when we extend our data from 2008 to 2020, and identify, for the first time, significant correlations between *Swift*-XRT and *Fermi*-LAT. We additionally find correlations between high-energy γ-rays and radio, with the radio lagging by more than 100 days, placing the γ-ray emission zone upstream of the radio-bright regions in the jet. Furthermore, Mrk 501 showed a historically low activity in X-rays and VHE γ-rays from mid-2017 to mid-2019 with a stable VHE flux (>0.2 TeV) of 5% the emission of the Crab Nebula. The broadband spectral energy distribution (SED) of this 2-year-long low-state, the potential baseline emission of Mrk 501, can be characterized with one-zone leptonic models, and with (lepto)-hadronic models fulfilling neutrino flux constraints from IceCube. We explore the time evolution of the SED towards the low-state, revealing that the stable baseline emission may be ascribed to a standing shock, and the variable emission to an additional expanding or traveling shock.

- A lower bound on intergalactic magnetic fields from time variability of 1ES 0229+200 from MAGIC and Fermi/LAT observations

Extended and delayed emission around distant TeV sources induced by the effects of propagation of γ ray s through the intergalactic medium can be used for the measurement of the intergalactic magnetic field (IGMF). We search for delayed GeV emission from the hard-spectrum TeV γ-ray emitting blazar 1ES 0229+200, with the goal to detect or constrain the IGMF-dependent secondary flux generated during the propagation of TeV γ ray s through the intergalactic medium. We analyze the most recent MAGIC observations over a 5 year time span, and complement them with historic data of the H.E.S.S. and VERITAS telescopes along with a 12-year long exposure of the *Fermi*/LAT telescope. We use them to trace source evolution in the GeV-TeV band over one-and-a-half decade in time. We use Monte Carlo simulations to predict the delayed secondary γ-ray flux, modulated by the source variability, as revealed by TeV-band observations. We then compare these predictions for various assumed IGMF strengths to all available measurements of the γ-ray flux evolution. We find that the source flux in the energy range above 200 GeV experiences variations around its average on the 14 years time span of observations. No evidence for the flux variability is found in $1 - 100$ GeV energy range accessible to *Fermi*/LAT. Non-detection of variability due to delayed emission from electromagnetic cascade developing in the intergalactic medium imposes a lower bound of $B > 1.8 \times 10^{-17}$ G for long correlation length IGMF and $B > 10^{-14}$ G for an IGMF of the cosmological origin. Though weaker than the one previously derived from the analysis of *Fermi*/LAT data, this bound is more robust, being based on a conservative intrinsic source spectrum estimate and accounting for the details of source variability in the TeV energy band. We discuss implications of this bound for cosmological magnetic fields which might explain the baryon asymmetry of the Universe.

3 Publications-2023

- Sahakyan N., Harutyunyan G., Israyelyan D., Origin of multiwavelength emission from flaring high redshift blazar PKS 0537-286, Monthly Notices of the Royal Astronomical Society, Volume 521, Issue 1, pp.1013-1022, 2023
- Sahakyan N., Vardanyan V., Khachatryan M., Gradient boosting decision trees classification of blazars of uncertain type in the fourth Fermi-LAT catalogue, Monthly Notices of the Royal Astronomical Society, Volume 519, Issue 2, pp.3000-3010, 2023
- Aimuratov Y., Becerra L., Bianco C., Cherubini C., Della Valle M., Filippi S., Li, Liang, Moradi R., Rastegarnia F., Rueda J., Ruffini R., Sahakyan N., Wang Y., Zhang S., GRB-SN Association within the Binary-driven Hypernova Model, The Astrophysical Journal, Volume 955, Issue 2, id.93, 29 pp., 2023.
- Sahakyan N., Giommi P., Padovani P., Petropoulou M., Bégué D., Boccardi B., Gasparyan S., A multimessenger study of the blazar PKS 0735+178: a new major neutrino source candidate, Monthly Notices of the Royal Astronomical Society, Monthly Notices of the Royal Astronomical Society, Volume 519, Issue 1, pp.1396-1408, 2023
- Ren H., Cerruti M., Sahakyan N., Quasi-periodic oscillations in the γ-ray light curves of bright active galactic nuclei, Astronomy & Astrophysics, Volume 672, id.A86, 31 pp., 2023
- Harutyunyan G., Multiwavelength Properties of Selected High Redshift Blazars, Astrophysics, Volume 66, Issue 2, p.181-193, 2023
- MAGIC Collaboration, Abe H., Abe, K., Abe S.,..... Gasparyan S.,.... Sahakyan N.,....., Performance of the joint LST-1 and MAGIC observations evaluated with Crab Nebula data, Astronomy & Astrophysics, Volume 680, id.A66, 21pp., 2023

- MAGIC Collaboration, Abe H., Abe S., Acciari V., ... Gasparyan S.,.... Sahakyan N.,....., MAGIC observations provide compelling evidence of hadronic multi-TeV emission from the putative PeVatron SNR G106.3+2.7, Astronomy & Astrophysics, Volume 671, id.A12, 12pp., 2023

- MAGIC Collaboration, Abe H., Abe S., Acciari V., ... Gasparyan S.,.... Sahakyan N.,....., Search for Gamma-Ray Spectral Lines from Dark Matter Annihilation up to 100 TeV toward the Galactic Center with MAGIC, Physical Review Letters, Volume 130, Issue 6, article id.061002, 2023

- MAGIC Collaboration, Abe H., Abe S., Acciari V., ... Gasparyan S.,.... Sahakyan N.,....., Multimessenger Characterization of Markarian 501 during Historically Low X-Ray and γ-Ray Activity, The Astrophysical Journal Supplement Series, Volume 266, Issue 2, id.37, 43pp., 2023.

- MAGIC Collaboration, Acciari V., Ansoldi S., Antonelli L.,..... Gasparyan S.,.... Sahakyan N.,....., Study of the GeV to TeV morphology of the γ Cygni SNR (G 78.2+2.1) with MAGIC and Fermi-LAT. Evidence for cosmic ray escape, Astronomy & Astrophysics, Volume 670, id. A8, 20pp., 2023.

- MAGIC Collaboration, Acciari V., Aniello T., Ansoldi S.,..... Gasparyan S.,.... Sahakyan N.,....., Long-term multi-wavelength study of 1ES 0647+250, Astronomy & Astrophysics, Volume 670, id. A49, 20pp., 2023.

- MAGIC Collaboration, Acciari V., Agudo I., Aniello T.,..... Gasparyan S.,.... Sahakyan N.,....., A lower bound on intergalactic magnetic fields from time variability of 1ES 0229+200 from MAGIC and Fermi/LAT observations, Astronomy and Astrophysics, Volume 670, id. A145, 8pp., 2023.

- Gasparyan S., Begue D. and Sahakyan N., Time-dependent lepto-hadronic modeling of the emission processes in blazar jets, The Sixteenth Marcel Grossmann Meeting, World Scientific Publishing, ISBN 9789811269776, pp. 429-444, 2023

- Rueda J., Ruffini R., Liang L., Moradi R., Sahakyan N., Wang Y., The white dwarf binary merger model of GRB 170817A, World Scientific Publishing, ISBN 9789811269776, pp. 217-241, 2023

- Harutyunyan G., Israyelyan D., Multiwavelength study of high-redshift blazars, World Scientific Publishing, ISBN 9789811269776, pp. 445-461, 2023

- Ruffini R., Aimuratov Y., Becerra L., Bianco C., Cherubini Ch., Filippi S., Liang L., Moradi R., Rastegarnia F., Punsly B., Rueda J. Sahakyan N., Wang Yu, Xue Sh., The role of a standard family of Ic supernovae in BDHN I, BDHN II, and BDHN III GRBs, Astronomische Nachrichten, Volume 344, Issue 1-2, article id. e20220099, 2023

3.1 Publications-2012-2022

- Sahakyan, N., Israyelyan, D., Harutyunyan, G., Gasparyan, S., Vardanyan, V., Khachatryan, M. 2022. Modelling the time variable spectral energy distribution of the blazar CTA 102 from 2008 to 2022. Monthly Notices of the Royal Astronomical Society 517, 2757–2768. doi:10.1093/mnras/stac2875

- Sahakyan, N., Giommi, P. 2022, A 13-yr-long broad-band view of BL Lac, Monthly Notices of the Royal Astronomical Society 513, 4645–4656. doi:10.1093/mnras/stac1011

- Gasparyan, S., Bégué, D., Sahakyan, N. 2022. Time-dependent lepto-hadronic modelling of the emission from blazar jets with SOPRANO: the case of TXS 0506 + 056, 3HSP J095507.9 + 355101, and 3C 279. Monthly Notices of the Royal Astronomical Society 509, 2102–2121. doi:10.1093/mnras/stab2688

- Middei R., Giommi P., Perri M., Turriziani S., Sahakyan N., Chang Y., Leto C., Verrecchia F., 2022 The first hard X-ray spectral catalogue of Blazars observed by NuSTAR. Monthly Notices of the Royal Astronomical Society 514, 3179–3190. doi:10.1093/mnras/stac1185

- Rueda, J. A., Li, L., Moradi, R., Ruffini, R., Sahakyan, N., Wang, Y. 2022. On the X-Ray, Optical, and Radio Afterglows of the BdHN I GRB 180720B Generated by Synchrotron Emission. The Astrophysical Journal 939. doi:10.3847/1538-4357/ac94c9

- Wang, Yu, Rueda J., Ruffini R., Moradi R., Liang L., Aimuratov Y., Rastegarnia F., Eslamzadeh S., Sahakyan N., Zheng Y., 2022 GRB 190829A-

A Showcase of Binary Late Evolution, The Astrophysical Journal 936. doi:10.3847/1538-4357/ac7da3

- MAGIC Collaboration, Acciari V., Ansoldi S.,.... Gasparyan, S.,...Sahakyan N.,.... 2022, Investigating the Blazar TXS 0506+056 through Sharp Multiwavelength Eyes During 2017-2019. The Astrophysical Journal 927. doi:10.3847/1538-4357/ac531d
- MAGIC Collaboration, Abe H., Abe S.,.... Gasparyan, S.,...Sahakyan N.,.... 2022, Gamma-ray observations of MAXI J1820+070 during the 2018 outburst. Monthly Notices of the Royal Astronomical Society 517, 4736–4751. doi:10.1093/mnras/stac2686
- MAGIC Collaboration, Adams C., Batista P.,.... Gasparyan, S.,...Sahakyan N.,.... 2022, Multiwavelength Observations of the Blazar VER J0521+211 during an Elevated TeV Gamma-Ray State, The Astrophysical Journal 932. doi:10.3847/1538-4357/ac6dd9
- MAGIC Collaboration, Acciari V., Ansoldi S.,.... Gasparyan, S.,...Sahakyan N.,.... 2022, Proton acceleration in thermonuclear nova explosions revealed by gamma rays. Nature Astronomy 6, 689–697. doi:10.1038/s41550-022-01640-z
- MAGIC Collaboration, Acciari V., Ansoldi S.,.... Gasparyan, S.,...Sahakyan N.,.... 2022, Multi-epoch monitoring of TXS 0506+056 with MAGIC and MWL partners. 37th International Cosmic Ray Conference. doi:10.22323/1.395.0875
- MAGIC Collaboration, Acciari V., Ansoldi S.,.... Gasparyan, S.,...Sahakyan N.,.... 2022, Multiwavelength variability and correlation studies of Mrk421 during historically low X-ray and γ-ray activity in 2015–2016. 37th International Cosmic Ray Conference. doi:10.22323/1.395.0866
- MAGIC Collaboration, Acciari V., Ansoldi S.,.... Gasparyan, S.,...Sahakyan N.,.... 2022. Combined searches for dark matter in dwarf spheroidal galaxies observed with the MAGIC telescopes, including new data from Coma Berenices and Draco. Physics of the Dark Universe 35. doi:10.1016/j.dark.2021.100912
- MAGIC Collaboration, Acciari V., Ansoldi S.,.... Gasparyan, S.,...Sahakyan N.,.... 2022, Multiwavelength study of the gravitationally lensed blazar QSO B0218+357 between 2016 and 2020. Monthly Notices of the Royal Astronomical Society 510, 2344–2362. doi:10.1093/mnras/stab3454

- Rueda J., Ruffini R., Li L., Moradi R., Sahakyan, N., Wang Y., 2022. The white dwarf binary merger model of GRB 170817A, International Journal of Modern Physics D 31. doi:10.1142/S0218271822300130

- Sahakyan, N., Modelling the broad-band emission of 3C 454.3, Monthly Notices of the Royal Astronomical Society, Volume 504, Issue 4, 2021, pp.5074-5086.

- Sahakyan, N. and Giommi, P., The strange case of the transient HBL blazar 4FGL J1544.3-0649, Monthly Notices of the Royal Astronomical Society, Volume 502, Issue 1, 2021, pp.836-844.

- Giommi, P.....sahakyan, N....., X-ray spectra, light curves and SEDs of blazars frequently observed by Swift, Monthly Notices of the Royal Astronomical Society, Volume 507, Issue 4, 2021, pp.5690-5702.

- Ruffini, R..... Sahakyan, N....., The morphology of the X-ray afterglows and of the jetted GeV emission in long GRBs, Monthly Notices of the Royal Astronomical Society, Volume 504, Issue 4, 2021, pp.5301-5326.

- MAGIC Collaboration, Adams, C.....Sahakyan, N....., Observation of the Gamma-Ray Binary HESS J0632+057 with the H.E.S.S., MAGIC, and VERITAS Telescopes, The Astrophysical Journal, Volume 923, Issue 2, id.241, 2021, 30 pp.

- MAGIC Collaboration, Acciari V., Ansoldi S.,.... Gasparyan, S.,...Sahakyan N.,.... Search for Very High-energy Emission from the Millisecond Pulsar PSR J0218+4232, The Astrophysical Journal, Volume 922, Issue 2, id.251, 2021, 14 pp.

- MAGIC Collaboration, Acciari V., Ansoldi S.,.... Gasparyan, S.,...Sahakyan N.,.... Investigation of the correlation patterns and the Compton dominance variability of Mrk 421 in 2017, Astronomy & Astrophysics, Volume 655, id.A89, 2021, 36 pp.

- MAGIC Collaboration, Acciari V., Ansoldi S.,.... Gasparyan, S.,...Sahakyan N.,.... First detection of VHE gamma-ray emission from TXS 1515-273, study of its X-ray variability and spectral energy distribution, Monthly Notices of the Royal Astronomical Society, Volume 507, Issue 1, 2021, pp.1528-1545.

- MAGIC Collaboration, Acciari V., Ansoldi S.,.... Gasparyan, S.,...Sahakyan N.,.... Multiwavelength variability and correlation studies of Mrk 421 during historically low X-ray and γ-ray activity in 2015-2016, Monthly Notices of the Royal Astronomical Society, Volume 504, Issue 1, 2021, pp.1427-1451.
- MAGIC Collaboration, Algaba J., Anczarski J.,.... Gasparyan, S.,...Sahakyan N.,.... Broadband Multi-wavelength Properties of M87 during the 2017 Event Horizon Telescope Campaign, The Astrophysical Journal Letters, Volume 911, Issue 1, id.L11, 2021, 43 pp.
- Abdalla H., Adam R.,.... Gasparyan, S.,...Sahakyan N.,.... H.E.S.S. and MAGIC observations of a sudden cessation of a very-high-energy γ-ray flare in PKS 1510-089 in May 2016, Astronomy & Astrophysics, Volume 648, id.A23, 2021, 22 pp.
- MAGIC Collaboration, Acciari V., Ansoldi S.,.... Gasparyan, S.,...Sahakyan N.,...., VHE gamma-ray detection of FSRQ QSO B1420+326 and modeling of its enhanced broadband state in 2020, Astronomy & Astrophysics, Volume 647, id.A163, 2021, 19 pp.
- MAGIC Collaboration, Acciari V., Ansoldi S.,.... Gasparyan, S.,...Sahakyan N.,...., MAGIC Observations of the Nearby Short Gamma-Ray Burst GRB 160821B, The Astrophysical Journal, Volume 908, Issue 1, id.90, 2021, 11 pp.
- Sahakyan N., Israyelyan D., Harutyunyan G., Khachatryan M., Gasparyan S., Multiwavelength study of high-redshift blazars, Monthly Notices of the Royal Astronomical Society, olume 498, Issue 2, 2020, p.2594-2613.
- Sahakyan N., Broad-band study of high-synchrotron-peaked BL Lac object 1ES 1218+304, Monthly Notices of the Royal Astronomical Society, Volume 496, Issue 4, 2020, pp.5518-5527
- Sahakyan, N., Investigation of the γ-ray spectrum of CTA 102 during the exceptional flaring state in 2016-2017, Astronomy and Astrophysics, Volume 635, id.A25, 2020, 10 pp.
- Sahakyan N., Israyelyan D., Harutyunyan G., A Multiwavelength Study of Distant Blazar PKS 0537-286, Astrophysics, volume 63, 2020, p. 459–469

- Sahakyan N., Harutyunyan G., Israelyan D., Khachatryan M., Exploring the Origin of Multiwavelength Emission from High-Redshift Blazar B3 1343 + 451, Astrophysics, Volume 63, Issue 3, 2020, p.334-348

- Giommi P., Chang Y., Turriziani S., Glauch T., Leto C., Verrecchia F., Padovani P., Penacchioni A., Arneodo F., Barres de Almeida U., Brandt C., Capalbi M., Civitarese O., D; Elia V., Di Giovanni A., De Angelis M., Del Rio Vera J., Di Pippo S., Middei R., Perri M., Pollock A., Puccetti S., Ricard N., Ruffini R., Sahakyan N., Open Universe survey of Swift-XRT GRB fields: Flux-limited sample of HBL blazars, Astronomy and Astrophysics, Volume 642, id.A141, 2020, 9 pp.

- Sahakyan N., High Energy γ-ray variability of NGC 1275 and 3C 120, Proceedings of the International Astronomical Union, Volume 342, 2020, pp. 172-175

- MAGIC Collaboration, VERITAS Collaboration, Abeysekara, A., Benbow, W.,.... Gasparyan, S.,...Sahakyan N.,.... Villata, M., The Great Markarian 421 Flare of 2010 February: Multiwavelength Variability and Correlation Studies, The Astrophysical Journal, Volume 890, Issue 2, id.97, 2020, 21 pp.

- MAGIC Collaboration, Acciari V., Ansoldi S.,.... Gasparyan, S.,...Sahakyan N.,.... Lien, A., Multiwavelength variability and correlation studies of Mrk 421 during historically low X-ray and γ-ray activity in 2015-2016, Monthly Notices of the Royal Astronomical Society, DOI: 10.1093/mnras/staa3727

- MAGIC Collaboration, Acciari V., Ansoldi S.,.... Gasparyan, S.,...Sahakyan N.,.... Zarić, D., The Great Markarian 421 Flare of 2010 February: Multiwavelength Variability and Correlation Studies, Astronomy and Astrophysics, Volume 635, id.A158, 2020, 10 pp.

- MAGIC Collaboration, Acciari V., Ansoldi S.,.... Gasparyan, S.,...Sahakyan N.,.... Lohfink A., New Hard-TeV Extreme Blazars Detected with the MAGIC Telescopes, The Astrophysical Journal Supplement Series, Volume 247, Issue 1, id.16, 2020, 24 p.

- MAGIC Collaboration, Acciari V., Ansoldi S.,.... Gasparyan, S.,...Sahakyan N.,.... Walker R., Monitoring of the radio galaxy M 87 during a low-

emission state from 2012 to 2015 with MAGIC, Monthly Notices of the Royal Astronomical Society, Volume 492, Issue 4, 2020, p.5354-5365

- MAGIC Collaboration, Acciari V., Ansoldi S.,.... Gasparyan, S.,...Sahakyan N.,.... Tammi J., Study of the variable broadband emission of Markarian 501 during the most extreme Swift X-ray activity, Astronomy and Astrophysics, Volume 637, id.A86, 2020, 27 pp.
- MAGIC Collaboration, Acciari V., Ansoldi S.,.... Gasparyan, S.,...Sahakyan N.,.... Zarić, D., A search for dark matter in Triangulum II with the MAGIC telescopes, Physics of the Dark Universe, Volume 28, article id. 100529, 2020.
- MAGIC Collaboration, Acciari V., Ansoldi S.,.... Gasparyan, S.,...Sahakyan N.,.... Zarić, D., Broadband characterisation of the very intense TeV flares of the blazar 1ES 1959+650 in 2016, Astronomy and Astrophysics, Volume 638, id.A14, 2020, 16 pp.
- MAGIC Collaboration, Acciari V., Ansoldi S.,.... Gasparyan, S.,...Sahakyan N.,.... Reinthal R., Unraveling the Complex Behavior of Mrk 421 with Simultaneous X-Ray and VHE Observations during an Extreme Flaring Activity in 2013 April, The Astrophysical Journal Supplement Series, Volume 248, Issue 2, 2020, id.29
- MAGIC Collaboration, Acciari V., Ansoldi S.,.... Gasparyan, S.,...Sahakyan N.,.... Zheng W., An intermittent extreme BL Lac: MWL study of 1ES 2344+514 in an enhanced state, Monthly Notices of the Royal Astronomical Society, Volume 496, Issue 3, 2020, pp.3912-3928
- MAGIC Collaboration, Acciari V., Ansoldi S.,.... Gasparyan, S.,...Sahakyan N.,.... Zarić, D., Studying the nature of the unidentified gamma-ray source HESS J1841-055 with the MAGIC telescopes, Monthly Notices of the Royal Astronomical Society, Volume 497, Issue 3, 2020, p. 3734-3745
- MAGIC Collaboration, Acciari V., Ansoldi S.,.... Gasparyan, S.,...Sahakyan N.,.... Zarić, D., Bounds on Lorentz Invariance Violation from MAGIC Observation of GRB 190114C, Physical Review Letters, Volume 125, Issue 2, 2020, article id.021301
- MAGIC Collaboration, Acciari V., Ansoldi S.,.... Gasparyan, S.,...Sahakyan N.,.... Kehusmaa P., Testing two-component models on very high-energy

gamma-ray-emitting BL Lac objects, Astronomy and Astrophysics, Volume 640, id.A132, 2020, 29 pp.

- MAGIC Collaboration, Acciari V., Ansoldi S.,.... Gasparyan, S.,...Sahakyan N.,.... Zarić, D., MAGIC observations of the diffuse γ-ray emission in the vicinity of the Galactic center, Astronomy and Astrophysics, Volume 642, id.A190, 2020, 9 pp.

- MAGIC Collaboration, Acciari V., Ansoldi S.,.... Gasparyan, S.,...Sahakyan N.,.... Parkinson P., Detection of the Geminga pulsar with MAGIC hints at a power-law tail emission beyond 15 GeV, Astronomy and Astrophysics, Volume 643, id.L14, 2020, 6 p.

- V. Acciari,.....S. Gasparyan...N. Sahakyan, ... D. Zaric, "Testing emission models on the extreme blazar 2WHSP J073326.7+515354 detected at very high energies with the MAGIC telescopes", Monthly Notices of the Royal Astronomical Society, Volume 490, Issue 2, p.2284-2299, 2019.

- R. Ruffini, R. Moradi, J. Rueda, L. Becerra, C. Bianco, C. Cherubini, S. Filippi, Y. Chen, M. Karlica, N. Sahakyan, Y. Wang, S. Xue, "On the GeV Emission of the Type I BdHN GRB 130427A", The Astrophysical Journal, Volume 886, Issue 2, article id. 82, 13 pp., 2019.

- V. Acciari,.....S. Gasparyan...N. Sahakyan, ... D. Zaric, "Observation of inverse Compton emission from a long γ-ray burst", Nature, Volume 575, Issue 7783, p.459-463, 2019.

- V. Acciari,.....S. Gasparyan...N. Sahakyan, ... D. Zaric, "Teraelectronvolt emission from the γ-ray burst GRB 190114C", Nature, Volume 575, Issue 7783, p.455-458, 2019.

- N. Sahakyan, "Origin of the multiwavelength emission of PKS 0502+049", accepted for publication in Astronomy and Astrophysics, doi.org/10.1051/0004-6361/201936715, arXiv:1911.12087, 2019.

- V. Acciari,.....S. Gasparyan...N. Sahakyan, ... D. Zaric, "New hard-TeV extreme blazars detected with the MAGIC telescopes", accepted for publication in Astrophysical Journal Supplement, arXiv:1911.06680, 2019.

- P. Giommi, C. Brandt, U. Barres de Almeida, A. Pollock, F. Arneodo, Y. Chang, O. Civitarese, M. Angelis, V. DElia, J. Del Rio Vera, S. Di Pippo,

R. Middei, A. Penacchioni, M. Perri, R. Ruffini, N. Sahakyan, S. Turriziani, "Open Universe for Blazars: a new generation of astronomical products based on 14 years of Swift-XRT data", Astronomy and Astrophysics, Volume 631, id.A116, 11 pp., 2019.

- T. Glauch, P. Padovani, P. Giommi, E. Resconi, B. Arsioli, N. Sahakyan, M. Huber, "Dissecting the region around IceCube-170922A: the blazar TXS 0506+056 as the first cosmic neutrino source", EPJ Web of Conferences, Volume 207, id.02003, 2019.

- V. Acciari,.....S. Gasparyan...N. Sahakyan, ... D. Zaric, "Constraints on Gamma-Ray and Neutrino Emission from NGC 1068 with the MAGIC Telescopes", The Astrophysical Journal, Volume 883, Issue 2, article id. 135, 9 pp., 2019.

- V. Acciari,.....S. Gasparyan...N. Sahakyan, ... D. Zaric, "Measurement of the extragalactic background light using MAGIC and Fermi-LAT gamma-ray observations of blazars up to z = 1", Monthly Notices of the Royal Astronomical Society, Volume 486, Issue 3, p.4233-4251, 2019.

- V. Acciari,.....S. Gasparyan...N. Sahakyan, ... D. Zaric, "Deep observations of the globular cluster M15 with the MAGIC telescopes", Monthly Notices of the Royal Astronomical Society, Volume 484, Issue 2, p.2876-2885, 2019.

- J. Rueda, R. Ruffini, Y. Wang, C. Bianco, J. Blanco-Iglesias, M. Karlica, P. Loren-Aguilar, R. Moradi, N. Sahakyan, "Electromagnetic emission of white dwarf binary mergers", Journal of Cosmology and Astroparticle Physics, Issue 03, article id. 044, 2019.

- N. Sahakyan, "Origin of the multiwavelength emission of PKS 0502+049", Astronomy and Astrophysics, Volume 622, id.A144, 10 pp. 2019.

- R. Ruffini, M. Karlica, N. Sahakyan, J. Rueda, Y. Wang, G. Mathews, C. Bianco, M. Muccino, "A GRB Afterglow Model Consistent with Hypernova Observations", The Astrophysical Journal, Volume 869, Issue 2, article id. 101, 9 pp. 2018.

- A. Abeysekara, ... N. Sahakyan, ... D. Zaric, "Periastron Observations of TeV Gamma-Ray Emission from a Binary System with a 50-year Pe-

riod", The Astrophysical Journal Letters, Volume 867, Issue 1, article id. L19, 8 pp., 2018.

- P. Padovani, P. Giommi, E. Resconi, T. Glauch, B. Arsioli, N. Sahakyan, M. Huber, "Dissecting the region around IceCube-170922A: the blazar TXS 0506+056 as the first cosmic neutrino source", Monthly Notices of the Royal Astronomical Society, Volume 480, Issue 1, p.192-203, 2018.

- N. Sahakyan, "Lepto-hadronic γ-Ray and Neutrino Emission from the Jet of TXS 0506+056", The Astrophysical Journal, Volume 866, Issue 2, article id. 109, 6 pp. 2018.

- S. Gasparyan, N. Sahakyan, V. Baghmanyan, D. Zargaryan, "On the Multiwavelength Emission from CTA 102", The Astrophysical Journal, Volume 863, Issue 2, article id. 114, 11 pp., 2018.

- M. Aartsen, ... N. Sahakyan, ... T. Yuan, "Neutrino emission from the direction of the blazar TXS 0506+056 prior to the IceCube-170922A alert", Science, Volume 361, Issue 6398, pp. 147-151, 2018.

- V. Baghmanyan, M. Tumanyan, N. Sahakyan, Y. Vardanyan, "High-Energy γ -Ray Emission from PKS 0625-35", Astrophysics, Volume 61, Issue 2, pp.160-170, 2018.

- N. Sahakyan, V. Baghmanyan, D. Zargaryan, "Fermi-LAT observation of nonblazar AGNs", Astronomy & Astrophysics, Volume 614, id.A6, 11 pp., 2018.

- B. Fraga, U. Barres de Almeida, S. Gasparyan, P. Giommi, N. Sahakyan, "Time-Evolving SED of MKN421: a multi-band view and polarimetric signatures", Frontiers in Astronomy and Space Sciences, Volume 5, id.1, 2018.

- S. Gasparyan, N. Sahakyan, P. Chardonnet, "The origin of HE and VHE gamma-ray flares from FSRQs", International Journal of Modern Physics D, Volume 27, Issue 10, id. 1844007, 2018.

- D. Zargaryan, N. Sahakyan, H. Harutyunian, "Chandra observations of gamma-ray emitting radio galaxies", International Journal of Modern Physics D, Volume 27, Issue 10, id. 1844022, 2018.

- V. Baghmanyan, N. Sahakyan, "X-ray and γ-ray emissions from NLSy1 galaxies", International Journal of Modern Physics D, Volume 27, Issue 10, id. 1844001, 2018.

- D. Zargaryan, S. Gasparyan, V. Baghmanyan and N. Sahakyan, "Comparing 3C 120 jet emission at small and large scales", Astronomy & Astrophysics, Volume 608, id. A37, 10, 2017.

- U. Barres de Almeida, F. Bernardo, P. Giommi, N. Sahakyan, S. Gasparyann and C. Brandt, "Long-Term Multi-Band and Polarimetric View of Mkn 421: Motivations for an Integrated Open-Data Platform for Blazar Optical Polarimetry", Galaxies, vol. 5, issue 4, p. 90, 2017.

- V. Baghmanyan, S. Gasparyan and N. Sahakyan, "Rapid Gamma-Ray Variability of NGC 1275", The Astrophysical Journal, Volume 848, Issue 2, article id. 111, 8, 2017.

- N. Sahakyan and S. Gasparyan "High energy gamma-ray emission from PKS 1441+25", Monthly Notices of the Royal Astronomical Society, 470, 3, p.2861-2869, 2017.

- N. Sahakyan, V. Baghmanyan, and D. Zargaryan, "Gamma-ray Emission from Non-Blazar AGNs", AIP Conference Proceedings, Volume 1792, Issue 1, id.050002, 2017.

- N. Sahakyan and S. Gasparyan, "High Energy Gamma-Rays From PKS 1441+25", AIP Conference Proceedings, Volume 1792, Issue 1, id.050005, 2017.

- V. Baghmanyan, "Gamma-Ray Variability of NGC 1275", AIP Conference Proceedings, Volume 1792, Issue 1, id.050007, 2017.

- D. Zargaryan, "The Gamma-Ray Emission from Broad-Line Radio Galaxy 3C 120",AIP Conference Proceedings, Volume 1792, Issue 1, id.050008, 2017.

- N. Sahakyan, "Galactic sources of high energy neutrinos: Expectation from gamma-ray data", EPJ Web of Conferences, Volume 121, id.05005, 2016.

- Sahakyan, N., Zargaryan, D. and Baghmanyan, V. "On the gamma-ray emission from 3C 120", Astronomy & Astrophysics, Volume 574, id.A88, 5 pp., 2015.
- Sahakyan, N., Yang, R., Rieger, F., Aharonian, F. and de Ona-Wilhelmi, E. "High Energy Gamma Rays from Centaurus a" Proceedings of the MG13 Meeting on General Relativity ISBN 9789814623995, pp. 1028-1030, 2015.
- Sahakyan, N., Piano, G. and Tavani, M. "Hadronic Gamma-Ray and Neutrino Emission from Cygnus X-3", The Astrophysical Journal, Volume 780, Issue 1, article id. 29, 2014.
- Sahakyan, N., Rieger, F., Aharonian, F., Yang, R., and de Ona-Wilhelmi, E. "On the gamma-ray emission from the core and radio lobes of the radio galaxy Centaurus A", International Journal of Modern Physics: Conference Series, Volume 28, id. 1460182, 2014.
- Sahakyan, N., Yang, R. Aharonian, F. and Rieger, F., " Evidence for a Second Component in the High-energy Core Emission from Centaurus A?", The Astrophysical Journal Letters, Volume 770, Issue 1, L6, 2013.
- Yang, R.-Z., Sahakyan, N., de Ona Wilhelmi, E., Aharonian, F. and Rieger, F., "Deep observation of the giant radio lobes of Centaurus A with the Fermi Large Area Telescope", Astronomy & Astrophysics, 542, A19, 2012.
- Sahakyan, N., "High energy gamma-radiation from the core of radio galaxy Centaurus A", Astrophysics, 55, 14, 2012.
- Sahakyan, N., "On the Origin of High Energy Gamma-Rays from Giant Radio Lobes Centarus A", International Journal of Modern Physics Conference Series, 12, 224, 2012.

4 Origin of multiwavelength emission from flaring high redshift blazar PKS 0537-286

4.1 Introduction

Blazars are radio-loud quasars with powerful relativistic jets that make a small angle to the observer's line of sight [160]. They are among the most energetic sources in the Universe and a dominant class of extragalactic sources in the high energy (HE; $>$ 100 MeV) γ-ray sky [e.g., 6]. The new possibility of extensive multiwavelength observations coupled with multi-messenger observations have the potential to widen our understanding of blazars.

Historically, blazars are sub-grouped in two large sub-classes: BL Lacs and flat-spectrum radio quasars (FSRQs) [160]. BL Lacs have nearly featureless optical spectra (very weak or no lines are observed) while the FSRQs have bright and broad lines with equivalent widths of $|EM| > 5$ Å. One of the most distinguishable features of blazars is the very strong variability of their emission in almost all the observed bands in various times scales, from minute to week or month scales; [e.g., 19, 16, 11, 148, 105]. This variability is stochastic in nature but a recent detection of quasi-periodic oscillations was reported [e.g., see 117, 127].

Being powerful emitters, blazars are frequently monitored in all the accessible wavelengths which resulted in accumulation of a substantial amount of data. The emission from blazars, predominantly of a nonthermal nature [e.g., 111], is dominated by Doppler-amplified emission from the jet, typically showing two broad peaks: the first at radio to X-ray bands, and the second at γ-rays. The low-energy component peak (ν^p_{syn}) is used to further classify blazars as low- (LBL/LSP), intermediate- (IBL/ISP) or high- (HBL/HSP) peaked sources when $\nu^p_{syn} < 10^{14}$ Hz, 10^{14} Hz $< \nu^p_{syn} < 10^{15}$ and $\nu^p_{syn} > 10^{15}$ Hz, respectively [112, 2]. However, ν^p_{syn} can be well above 2.4×10^{17} in ex-

treme blazars [e.g., 73, 50, 31, 121, 132] which are interesting as they challenge our current understanding of particle acceleration and emission processes. In addition, the remarkable γ-ray blazar 4FGL J1544.3-0649, which was undetected in the X-ray and γ-rays until May 2017, showed a transient-like behaviour, becoming a very bright source for a few months and detected by Fermi Large Area telescope (Fermi-LAT) and MAXI X-ray sky monitor [136]. This suggests the existence of an undiscovered blazar population which may occasionally flare.

The broadband spectral energy distribution (SED) of blazars can be modeled within different scenarios involving the interaction of electrons and protons in a single or multiple zone. Although, there is a consensus that the low-energy component is due to the synchrotron emission of ultra-relativistic charged electrons in the blazar jet, the origin of the second component is highly debated. In the leptonic scenarios, this component is due to inverse Compton scattering of low-energy photons which might be the produced synchrotron photons [synchrotron-self Compton model, SSC; 69, 99, 34] or be of an external origin [e.g., 150], such as photons directly emitted from the accretion disk [53, 54] or reflected from the broad-line region [150] or emitted from the dusty torus [33]. Alternatively, the second component can be due to either the synchrotron emission of the energetic protons inside the jet [107] or due to the secondaries generated in photo-pion and photo-pair interactions [97, 98, 107, 108, 36, 120, 63]. These hadronic models [especially lepto-hadronic models, e.g., **?** 86, 109**?** , 130, 129, 41, 131, 62, 63] have become more attractive after the observations of IceCube-170922A neutrino event from the direction of TXS 0506+056 [82, 81**?**] as well as after the observations of multiple neutrino events from the direction of PKS 0735+178 when it was bright in the optical/UV, X-ray and γ-ray bands [138].

Due to the extreme luminosities of blazars, even very high redshift ones can be observed [e.g., see 10]. The observation of distant blazars is of particular interest as they allow i) to study the relativistic jets as well as their connection with accretion disk/black hole in the early epochs of the Universe, ii) to measure the suppression of the γ-ray flux which can be used to estimate or constraint the density of the extragalactic background light (EBL) [88, 103, 61] and understand its cosmological evolution, iii) to investigate, in general, the properties of γ-ray emitting active galactic nuclei (AGN), which is important for the understanding of the cosmological evolution of the γ-ray background [4].

Due to their faintness, high redshift blazars are rather difficult to observe

and identify, limiting the number of already associated high redshift blazars. For example, in the fourth catalog of AGNs detected by Fermi-LAT [data release 3 (DR3); 6] only 110 blazars are observed beyond $z = 2.0$ and only 10 beyond $z = 3.0$. The most distant blazar observed in the γ-ray band is GB1508+5714 at $z = 4.31$. The physical properties of these high redshift blazars have been frequently investigated using multi-frequency data [e.g., 68, 70, 113, 116, 100, 10, 94, 115]. For example, in **(author?)** [114] by studying nine γ-ray emitting blazars and 133 candidate blazars with soft X-ray spectra it is shown that these high redshift blazars host massive black holes ($M_{BH} > 10^9\, M_\odot$) and have an accretion disk luminosity of $> 10^{46}\, erg\, s^{-1}$. Or, in **(author?)** [141], by studying the spectral and temporal properties of thirty-three distant blazars ($z > 2.5$) and modeling their SEDs, it is found that the emission region size is ≤ 0.05 pc, while the magnetic field and the Doppler factor are correspondingly within $0.10 - 1.74$ G and $10.0 - 27.4$.

Although the number of observed high redshift blazars is not high enough to perform statistically sound population studies, the investigation of the properties of individual objects provides interesting peaces to understand the general physics of high redshift blazars. The multiwavelength monitoring of several high redshift blazars opens wide opportunities for investigation of their multiwavelength spectral and temporal properties as well as for performing detailed theoretical modeling and interpretation of the results. For example, the continuous monitoring of these sources in the HE γ-ray band by Fermi-LAT [22] allows to select various emission states, or their observations in the X-ray band with Neil Gehrels Swift Observatory [65, hereafter Swift], and Nuclear Spectroscopic Telescope Array [NuSTAR; 78] combined with the γ-ray data allows a precise estimation of the second emission component peak, or the data in the optical/UV bands can be used to constrain the high energy tail of the synchrotron component and/or the direct thermal emission from the accretion disk [70]. Therefore, the data available in different bands can be used to put tighter constraints on the physics of individual high redshift blazars.

Here we present a broadband study of PKS 0537-286; at $z = 3.10$ [165] it is one of the brightest high redshift blazars. It was observed in the X-ray band with various instruments (e.g., Einstein observatory [170], ASCA [39, 149], ROSAT [59], etc.) showing a particularly hard X-ray spectrum (~ 1.2). In the γ-ray band, with an energy flux of $(1.44 \pm 0.006) \times 10^{-11}\, erg\, cm^{-2}\, s^{-1}$ in the fourth catalog of Fermi-LAT AGNs [DR3; 6], it is the brightest blazar beyond $z = 3.0$. Moreover, in several occasions γ-ray flares were observed when

the daily flux was above 10^{-6} *photon* cm^{-2} s^{-1} [163, 18, 45] which makes PKS 0537-286 the most distant γ-ray flaring blazar [94, 139].The broadband emission from PKS 0537-286 was successfully modeled within a one-zone synchrotron and external inverse Compton scenario where the excess in optical/UV band was interpreted as emission from bright thermal accretion disk [35].

In general, the peak of the second component in the SED of high redshift blazars is at MeV energies, which implies their HE γ-ray spectrum is soft, so they are not ideal sources for γ-ray observations. Therefore, the observation of the γ-ray flaring activity of distant blazars, which is crucial for testing different emission scenarios of relativistic jets, is even more interesting as compared with that of the nearby sources. Motivated *i)* by the availability of multiwavelength data from PKS 0537-286 observations - since 2008 in the HE γ-ray band by Fermi-LAT, multiple observations of PKS 0537-286 by Swift X-Ray Telescope (XRT) and Ultra-violet Optical Telescope (UVOT) instruments and two observations of PKS 0537-286 with NuSTAR, and *ii)* by the observed multiple flaring activities of PKS 0537-286, we decided to investigate the spectral and temporal properties of PKS 0537-286 by analyzing the data accumulated in the optical/UV, X-ray and γ-ray bands and put, through theoretical modeling, a constraint on the physical processes responsible for the PKS 0537-286 emission in the quiescent and flaring states.

The paper is structured as follows. The data extraction and analysis in the γ-ray, X-ray and optical/UV bands are presented correspondingly in Sections 4.2, 4.3 and 4.4. The SED of PKS 0537-286 and its evolution in time is presented in Section 4.5, and the origin of the emission is discussed in Section 4.6. The results are presented and discussed in section 6.4 while the summary is given in Section 4.8.

4.2 Fermi-LAT observations and data analyses

Fermi satellite launched in 2008 carries two instruments- the Large Area Telescope (LAT) is the main instrument on board designed to scan the entire sky in γ-ray band, and the Gamma-ray Burst Monitor (GBM) is designed to study gamma-ray bursts. LAT is a pair-conversion γ-ray telescope sensitive in the energy range from 20 MeV to 300 GeV with a field of view of $\sim$ 2.4 sr. It is by default in the all sky scanning mode which allows to study the HE properties of various sources, including blazars. For more details on the LAT see

(author?) [22].

We have analyzed the γ-ray data collected between August 4 2008 and September 9 2022 (MET=239557417–686130659). The data was reduced and analyzed following the standard procedures described in the Fermi-LAT documentation with *fermitools* version 2.0.8 using P8R3_SOURCE_V3 instrument response functions. The events in the energy range from 100 MeV to 300 GeV are selected from a circular region of interest (ROI) of 12° radius centered at the γ-ray location of PKS 0537-286 (RA$=$ 89.99, Dec$=$ $-$28.65), retrieving only events classified as evclass=128 and evtype= 3. A zenith angle cut less than 90° was introduced to remove the secondary γ-rays from the earth limb. The model file that includes point-like sources and background models was created based on the Fermi-LAT fourth source catalog (4FGL) incremental version [DR 3; 6], which is based on 12 years of initial Fermi-LAT operation and includes best-fit spectral parameters of all known 4FGL γ-ray sources in the ROI. The sources which are within 17° from the PKS 0537-286 location were included in the model file; the spectral parameters of the sources within $12^\circ - 17^\circ$ are fixed to their values reported in 4FGL while they are left free for the sources falling within $< 12^\circ$ radius. The galactic background and isotropic galactic emissions were modeled with the latest version available files, gll_iem_v07 and iso_ P8R3_SOURCE_V3_v1, respectively.

The γ-ray analysis is performed with gtlike tool, following the binned likelihood method. Initially, the spectrum of PKS 0537-286 was modeled with a log-parabolic model as in 4FGL. However, the fit was also performed when assuming a power-law model for PKS 0537-286 γ-ray emission and the resulting model file was used in the light-curve calculations, because for shorter periods a power-law can be a good approximation of the spectrum. The significance of the source emission is estimated using test statistic (TS), which is defined by $TS = 2(lnL_1 - lnL_0)$ where L_1 and L_0 are maximum likelihoods with and without the source, respectively [102].

In order to investigate the variability pattern of the source, the light curves were generated by two different methods. Initially, the whole time interval was divided into 5-day intervals and the photon index and flux of PKS 0537-286 were estimated by the unbinned analysis method from gtlike tool. Next, in order to obtain a deeper insight into the γ-ray flux evolution in time, the adaptively binned light curve was computed [95]. In this method, the bin widths above the optimal energy (E_{opt}) are adjusted to have fixed uncertainty, so in the case of flux increase shorter intervals are estimated, whereas in the quiescent/normal states time bins are wider. This method has been proven

to be a powerful tool in finding flaring periods in blazars [e.g., see 125, 37, 135, 171, 25, 64, 134, 133, 140, 137].

The adaptively binned light curve ($> E_{opt} = 168.19$ MeV) is shown in Fig. 4.1 upper panel. Up to MJD 57740 the γ-ray flux was in its average level of $(1-3) \times 10^{-8}\ photon\ cm^{-2}\ s^{-1}$ with no significant changes, while then, in several occasions, the γ-ray flux increased substantially. The light curve with 5-day (> 100 MeV) and adaptive bins ($> E_{opt} = 168.19$ MeV) for the period when the source was active in the γ-ray band are shown correspondingly in Fig. 4.1 panels a) and b). The first flaring period was between MJD 57876-57883 when the flux increased with a maximum of $(5.26 \pm 1.13) \times 10^{-7}\ photon\ cm^{-2}\ s^{-1}$. Starting from MJD 59170, the source entered an active emission state with several bright flaring periods between MJD 59204-59233, MJD 59301-59411 and MJD 59721-59738. The maximum γ-ray flux of the source, $(6.32 \pm 1.11) \times 10^{-7}\ photon\ cm^{-2}\ s^{-1}$ was also observed in these γ-ray flaring periods.

Fig. 4.1 panel c shows the γ-ray photon index estimated for the adaptively binned periods; it varies in time as well. In the non-flaring periods, the γ-ray spectrum is characterised by a soft spectrum with a mean of $\Gamma \simeq 2.83$ but the photon index hardens during the bright periods as can be seen from Fig. 4.1 panel c. For example, during the first flare between MJD 57876-57883 the hardest index of 2.49 ± 0.23 was observed on MJD 57879.9 or during the second flare between MJD 59204-59233 the hardest index was 2.25 ± 0.21 when the source was in an active state with a flux of $(6.12 \pm 1.22) \times 10^{-7}\ photon\ cm^{-2}\ s^{-1}$. During the hardest γ-ray emission period, 2.23 ± 0.18 was detected on MJD 59322 which is unusual for this source.

4.3 NuSTAR data analysis

NuSTAR is a hard X-ray telescope sensitive in the 3-79 keV energy range [78]. NuSTAR with two focal plane modules (FPMs), FPMA and FPMB, observed PKS 0537-286 on 28 December 2020 (MJD 59211.99) and on 24 October 2020 (MJD 59146.17) for 97.1 ks and 24.3 ks, respectively. It should be noted that around these observations PKS 0537-286 was also monitored with Swift (see dashed blue lines in Fig. 4.1 panel d), so the X-ray spectrum of the source can be obtained in a large range of 0.3-79 keV.

The NuSTAR data was analyzed applying the standard procedure and using *NuSTAR_Spectra* tool developed in **(author?)** [106]. *NuSTAR_Spectra* script

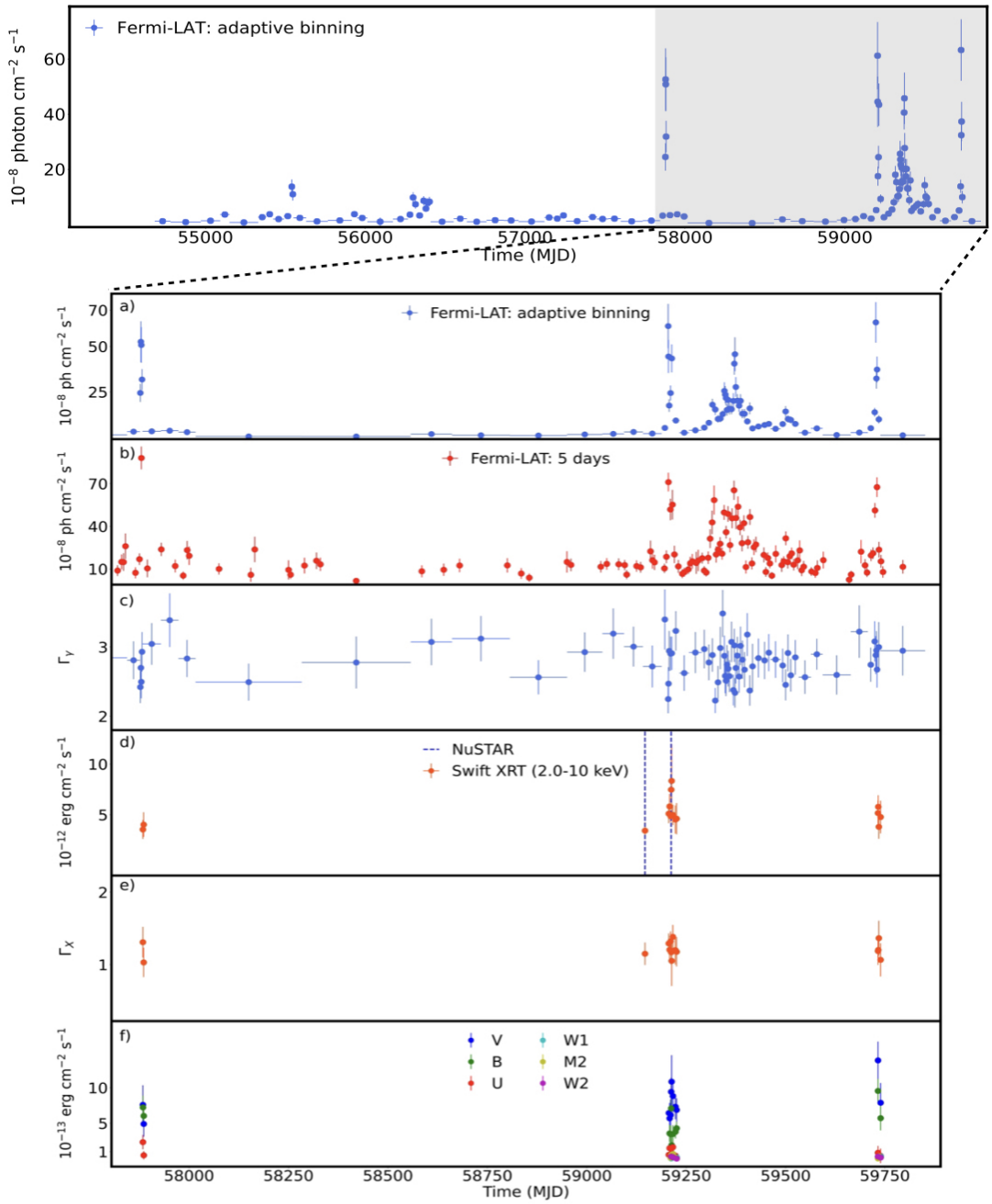

Figure 4.1: Multiwavelength light curve of PKS 0537-286. Top panel shows the long-term adaptively binned γ-ray light curve above 168.19 MeV. The other panels show the light curves after MJD 57800 (16 February 2017) when the source was active in the γ-ray band. *a)* adaptively binned γ-ray light curve, *b)* 5-day binned γ-ray light curve ($>$ 100 MeV), *c)* γ-ray photon index measured for the adaptive time bins, *d)* and *e)* X-ray flux (2-10 keV) and photon index in different Swift observations. The dashed blue lines show the NuSTAR observation times. *f)* Swift UVOT fluxes in V, B, U, W1, M2, and W2 bands.

downloads calibrated and filtered event files from the SSDC repository, uses *XIMAGE* package to precisely locate the source's coordinate then extracts high-level scientific products for the detected sources using nuproducts routine. The script automatically sets the source extraction region radius depending on the source counts (usually in the range of 30-70 arcsec). The background is computed in an annulus centered on the source with a minimum separation of 50 arcsec between the inner and outer radii. Then, a spectral analysis is performed using the XSPEC package [20] adopting Cash statistics [40]. More details on *NuSTAR_Spectra* are available in **(author?)** [106].

The analysis shows that the X-ray photon index of PKS 0537-286 is the same in both observations - 1.26 ± 0.06 and 1.26 ± 0.02 on MJD 59146.17 and MJD 59211.99, respectively. The X-ray flux between 3-10 keV measured on MJD 59146.17 is $F_{3-10\,keV} = (2.72 \pm 0.06) \times 10^{-12}\,erg\,cm^{-2}\,s^{-1}$ and on MJD 59211.99, it increased by about a factor of two, $F_{3-10\,keV} = (5.10 \pm 0.04) \times 10^{-12}\,erg\,cm^{-2}\,s^{-1}$. Similarly, the flux between 10-30 keV also increased in these two observations, being correspondingly $F_{10-30\,keV} = (5.79 \pm 0.20) \times 10^{-12}\,erg\,cm^{-2}\,s^{-1}$ and $F_{10-30\,keV} = (1.08 \pm 0.01) \times 10^{-11}\,erg\,cm^{-2}\,s^{-1}$. This shows that the source in the 3.0-30 keV range was in an enhanced state on 28 December 2020.

4.4 Swift data analysis

Swift is a space-based observatory with three main instruments onboard, namely burst alert telescope (BAT) sensitive in the energy range of 3.0-150.0 keV, XRT sensitive in the energy range of 0.3-10.0 keV, and UVOT sensitive in the optical/UV band 170 - 650 nm [65]. Swift performed 29 observations of PKS 0537-286 among which nine observations were performed before the lunch of Fermi-LAT. However, in order to investigate the flux changes in different years, we have analyzed all the data from Swift observations of PKS 0537-286.

4.4.1 Swift XRT

All the XRT observations were processed with Swift_xrtproc tool applying standard analysis procedure [74]. Swift_xrtproc downloads the raw data for each snapshot and for the whole observation, generates exposure maps and

calibrated data product using the XRTPIPELINE task adopting standard parameters and filtering criteria. The source region counts are estimated from a circle of a radius of 20 pixels while the background counts from an annular region centred around the source with a radius sufficiently large to avoid contamination from source photons. The resultant ungrouped data is loaded in XSPEC [20] for spectral fitting using Cash statistics [40], modeling the source spectrum as power-law and log-parabola. As a result, the X-ray photon index in the energy range 0.3-10 keV and the flux in various bands are estimated.

The 2-10 keV X-ray flux variation is shown in Fig. 4.1 panel d). Although in the X-ray band there is a limited number of observations, the flux variation is evident. The X-ray emission of the source in the 2.0-10 keV band was at the level of $\sim 3.0 \times 10^{-12}\, erg\, cm^{-2}\, s^{-1}$ but during the bright periods it is $\geq 5.0 \times 10^{-12}\, erg\, cm^{-2}\, s^{-1}$. The highest X-ray flux of $(8.34 \pm 3.59) \times 10^{-12}\, erg\, cm^{-2}\, s^{-1}$ was observed on MJD 59213.18. The X-ray spectrum of the source is hard (Fig. 4.1 panel e) and during all the observations $\Gamma_{X-ray} \leq 1.38$. Therefore, as it is typical for FSRQs, the X-ray band defines the rising part of the second component in the SED.

4.4.2 Swift UVOT

In the same periods, UVOT observed PKS 0537-286 in V (500-600 nm), B (380- 500 nm), U (300- 400 nm), W1 (220-400 nm), M2 (200-280 nm) and W2 (180–260 nm) filters. All the available 28 observations were downloaded and reduced using HEAsoft version 6.29 with the latest release of HEASARC CALDB. Photometry was computed using a five-arcsecond source region centered on the sky position of PKS 0537-286 and the background counts are estimated from a twenty-arcsecond region away from the source. The magnitudes were derived using uvotsource tool, then the fluxes were obtained using the conversion factors provided by **(author?)** [123] which were corrected for extinction using the reddening coefficient $E(B-V)$ from the Infrared Science Archive [1].

Fig. 4.1 panel f) shows the light curve of PKS 0537-286 in optical/UV bands. The source is relatively faint in all the filters with the flux around $\simeq 10^{-13}\, erg\, cm^{-2}\, s^{-1}$. In some cases, coinciding with the flares in the γ-ray band, the flux increased several times. The highest flux of the source was observed in V-band; on MJD 59213.18 and MJD 59732.67 it was $(1.08 \pm 0.37) \times$

[1] http://irsa.ipac.caltech.edu/applications/DUST/

$10^{-12}\,erg\,cm^{-2}\,s^{-1}$ and $(1.38 \pm 0.26) \times 10^{-12}\,erg\,cm^{-2}\,s^{-1}$, respectively. In addition, VOU-Blazar tool, which allows to search and collect all spectral information accessible through virtual observatory services and build the multiwavelength SEDs of blazars [43] was used to investigate the source emission properties in the infrared band. In particular, data extracted from the Wide-field Infrared Survey Explorer (WISE) and NEOWISE surveys [96] show that the source emission at 3.4 and 4.6 μm wavelengths (infrared) was at the level of several times $10^{-13}\,erg\,cm^{-2}\,s^{-1}$.

4.5 Multiwavelength SEDs

The data analyzed in this paper allows to build the SEDs of PKS 0537-286 in different periods. The single snapshot SED provides substantial information on the source emission properties whereas the variation of these SEDs in time is crucial for understanding the dynamical changes in the emission components. For this purpose, we generated SED/Light curve animation of PKS 0537-286 by showing the γ-ray spectra with all available data sets. For each adaptively binned interval we performed γ-ray spectral analysis using the unbinned likelihood method implemented in gtlike tool. Then, for each γ-ray period, together with the γ-ray data we plotted the Swift XRT, NuSTAR and Swift UVOT data as well as archival data extracted with VOU-blazar tool. By going from one to another γ-ray period we can investigate the changes in the multiwavelength SED of PKS 0537-286.

The SED/light curve animation is available here `youtube.com/4UPqf-C7EWc` . As the blazar is at $z = 3.10$ the UVOT flux could be affected by absorption of neutral hydrogen in intervening Lyman-α absorption systems [e.g., 70] which was corrected using the attenuation calculated in **(author?)** [67] for the UVOT filters. The SED/light curve animation shows the high amplitude changes observed in the γ-ray band; the gray background data points show the γ-ray flux estimated in different periods. Also, the spectral hardening in several bright γ-ray periods can be seen.

4.6 Origin of broadband emission

In the previous section, the generated multiwavelength SEDs show the features of PKS 0537-286 emission in different periods. It is especially important

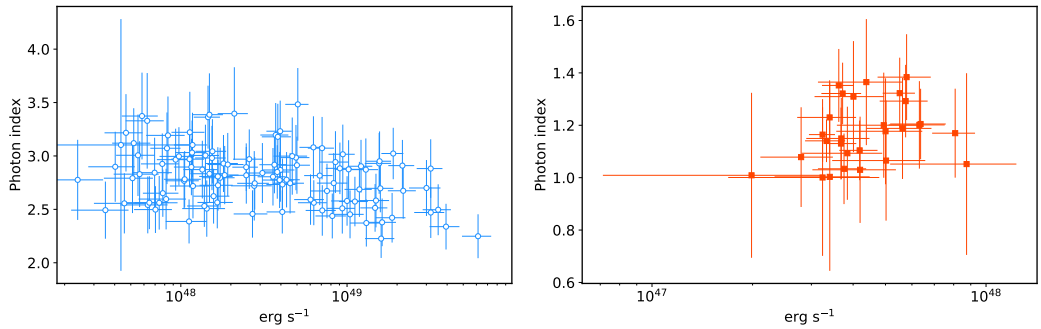

Figure 4.2: The luminosity versus the spectral index in the γ-ray (left panel) and X-ray bands (right panel).

to investigate the processes taking place in the jet of high redshift blazars as they could provide information on the jet plasma state in the early Universe. For this reason, the following periods were considered for modeling:

- The SED between MJD 55150-55330 when the source was in the quiescent state, i.e., the γ-ray flux above 100 MeV was $(2.77 \pm 0.84) \times 10^{-8}\ photon\ cm^{-2}\ s^{-1}$ and the 2-10 keV X-ray flux was $(3.29 \pm 1.11) \times 10^{-12}\ erg\ cm^{-2}\ s^{-1}$.

- The SED between MJD 59208-59212 when the source was bright in the γ-ray and X-ray (2-10 keV) bands with corresponding fluxes of $(5.46 \pm 0.83) \times 10^{-8}\ photon\ cm^{-2}\ s^{-1}$ and $(7.47 \pm 1.18) \times 10^{-12}\ erg\ cm^{-2}\ s^{-1}$. This period coincides with the NuSTAR observation on MJD 59211.99 which showed that the source was in an elevated X-ray emission state also in the 3-30 keV range.

The broadband SEDs were modeled using a one-zone leptonic scenario. In this model, it is assumed that the emission originates from a spherical blob of radius R moving with a bulk Lorentz factor of Γ at a small inclination angle of θ with respect to the observer. Due to the relativistic motion and small θ the radiation will be Doppler amplified by a factor of $\delta \simeq \Gamma$. The emission region magnetized with a field strength of B is filled with relativistic electrons whose energy distribution is given by

$$N_e = N_0\, \gamma^{-p}\, exp(-\frac{\gamma}{\gamma_{cut}}) \qquad \gamma > \gamma_{min} \tag{4.6.1}$$

where $\gamma = E_e/m_ec^2$ is the electron Lorentz factor, p is the power-law index, γ_{min} and γ_{cut} are the minimum and cut-off energy, respectively. The parameter N_0 defines the electron energy density through $U_e = m_ec^2 \int \gamma N_e(\gamma) d\gamma$.

The electrons with energy distribution given by Eq. 4.6.1 undergo synchrotron losses under the magnetic field, producing the data observed between radio to X-ray bands. Instead, the second component in the SED, from X-rays to γ-rays, is from the inverse Compton scattering of internal and external photons on the same population of the electrons. When the electrons upscatter the synchrotron photons, the second component is explained by the SSC component [69, 99, 34]. Alternatively, if the emission region is within the BLR, the second component can be due to external Compton scattering of direct disk radiation [EIC-disk; 53, 54] and/or due to external Compton scattering of photon reflected from BLR clouds [EIC-BLR; 150]. Instead, if the jet energy dissipation occurs at larger distances it can be due to external Compton scattering of dusty torus photons [EIC-torus; 33].

In this paper, for a general view we consider three different scenarios: *i)* the broadband emission from PKS 0537-286 is entirely due to synchrotron/SSC radiation, *ii)* the jet dissipation region is close to the central black hole, and SSC, EIC-disk and EIC-BLR are contributing to the HE component and iii) the emission region is beyond the BLR and the HE component is due to EIC-torus. It is assumed that BLR is a spherical shell [e.g., 56] with lower and upper boundaries of $0.9 \times R_{BLR}$ and $1.2 \times R_{BLR}$, respectively. R_{BLR} is assumed to scale as $R_{BLR} = 10^{17}\, L^{0.5}_{disc,45}$ cm where $L_{disc,45} = L_{disc}/10^{45}\, erg\, s^{-1}$ is the accretion disk luminosity [71]. Similarly, we assume that the distance of dusty torus is $2 \times 10^{18}\, L^{0.5}_{disc,45}$ [71] which emits $\eta = 0.5$ fraction of disk luminosity in the IR range for which we adopted $T_{torus} = 10^3$ K effective temperature. The disk luminosity and effective temperature are correspondingly $8.7 \times 10^{46}\, erg\, s^{-1}$ and $T_{disk} = 1.9 \times 10^4$ K estimated by fitting the thermal blue-bump component in the SED with a black-body component.

The remaining free model parameters are p, γ_{min}, γ_{cut}, U_e, B and R which should be constrained during the fitting. The SED fitting is performed using publicly available code JetSet which is a numerical code allowing to fit the radiative models to data and obtain the parameters statistically better explaining them [101, 157, 158, 159]. These parameters are initially constrained by using the Minuit optimizer and then improved by Markov Chain Monte Carlo (MCMC) sampling of their distributions. We applied the EBL model from **(author?)** [61] to correct the attenuation in the HE γ-ray band, but as the

γ-ray data extends to several tens of GeV it affects only the model extrapolation to higher energies.

4.7 Results and Discussions

At $z = 3.10$, PKS 0537-286 is one of the most powerful FSRQs in the extragalactic γ-ray sky; the time-averaged γ-ray luminosity of the source is $1.90 \times 10^{48}\, erg\, s^{-1}$ (assuming a distance of 27.08 Gpc). However, in several occasions, the source shows bright γ-ray flares when the flux substantially increases and the spectrum hardens. Fig. 4.2 left panel shows the γ-ray luminosity of PKS 0537-286 versus the photon index. During the bright periods, the luminosity increases, being above $10^{49}\, erg\, s^{-1}$; the maximum γ-ray luminosity corresponds to $6.14 \times 10^{49}\, erg\, s^{-1}$. It should be noted that among 113 adaptively binned intervals, the source luminosity was above $10^{49}\, erg\, s^{-1}$ in 25 intervals amounting 61.8 days when extreme γ-ray luminosity was observed. Photon index hardening with increasing luminosity/flux can be noticed in Fig. 4.2 left panel. In order to test possible correlation/anti-correlation between the luminosity and photon index, a Pearson correlation test was applied which yielded -0.39 with a probability of $P = 1.2 \times 10^{-5}$. This indicates moderate anti-correlation between the luminosity and photon index, that is when the source emission becomes brighter the photon index hardens (harder-when-brighter trend). It should be noted that for blazars such trend is frequently observed in different bands [e.g., 3, 1, 25, 136, 133, 64, 137] which can be interpreted as interplay between acceleration and cooling of the electrons [87].

PKS 0537-286 shows also interesting features in the X-ray band. The X-ray photon index versus the $0.3 - 10$ keV X-ray luminosity is shown in Fig. 4.2 right panel. The X-ray emission is characterized by a hard spectrum ($\Gamma_{X-ray} < 1.38$) with a high luminosity ($> 10^{47}\, erg\, s^{-1}$). It should be noted that *XMM-Newton* observations of PKS 0537-286 also showed a high luminosity of $2 \times 10^{47}\, erg\, s^{-1}$ with a spectral index of 1.27 ± 0.02 [126]. There is no evidence of softening or hardening when the source gets brighter in the X-ray band; the highest luminosity in the X-ray band is $8.74 \times 10^{47}\, erg\, s^{-1}$ observed on MJD 59213.18. Similarly, the $3 - 30$ keV X-ray luminosity was $1.40 \times 10^{48}\, erg\, s^{-1}$ on MJD 59211.99 and $7.47 \times 10^{47}\, erg\, s^{-1}$ on MJD 59146.17.

The SED of PKS 0537-286 was assembled in the flaring and quiescent periods (see Fig. 4.3). Comparing and contrasting the jet parameters obtained

through modeling of the SED in different periods is crucial, allowing to understand the processes at work in the jet of PKS 0537-286.

4.7.1 Synchrotron/SSC emission from the jet

Fig. 4.3 panels a and b show the results of the modeling when the entire emission is due to synchrotron/SSC emission from a compact region of the jet when the source is in a quiescent and flaring state, respectively. The corresponding model parameters are given in Table 4.1. In the quiescent state, the SED modeling shows that the spectral slope of the emitting particle distribution is 1.8 ± 0.1 and their distribution extends up to $(1.2 \pm 0.1) \times 10^4$. The strength of the magnetic field is found to be $(9.3 \pm 0.8) \times 10^{-3}$ G. The emission region size is $(2.0 \pm 0.1) \times 10^{17}$ cm, which is consistent with the flux variability of $t_{var} = (1+z) \times R/c\,\delta \approx 18.7$ days. The Doppler boosting factor is 16.8 ± 1.2 which is not different from the values usually estimated for FSRQs [e.g., see 71]. In this case, the synchrotron component decreases at $< 10^{14}$ Hz and it does not take into account the observed optical/UV data which are interpreted as thermal emission from the accretion disk (see the next subsection).

In the flaring period (Fig. 4.3 panel b), the SED modeling shows that the emitting electrons have a harder spectrum with $p = 1.6 \pm 0.03$ as compared with that in the quiescent state. The electrons are accelerated up to $\gamma_{cut} = (1.1 \pm 0.1) \times 10^4$ which is not significantly different from that in the quiescent state. In the flaring state, the magnetic field also increased, $B = (1.7 \pm 0.1) \times 10^{-2}$ G, which is caused by the increase of the synchrotron flux. Also, the Doppler boosting factor increased from 16.8 ± 1.2 to 24.9 ± 1.1 in order to explain the slight shift of the HE peak towards higher energies; above 100 MeV the γ-ray spectrum in the flaring period has a photon index of $\Gamma_\gamma = 2.73 \pm 0.17$ as compared with that of $\Gamma_\gamma = 2.91 \pm 0.16$ is the quiescent state. The modeling shows that during the flare, the emission is produced from a smaller region with a radius of $(1.6 \pm 0.1) \times 10^{17}$ cm corresponding to $t_{var} \simeq 10.0$ days, which indicates that the flaring emission is from a compact and faster moving region.

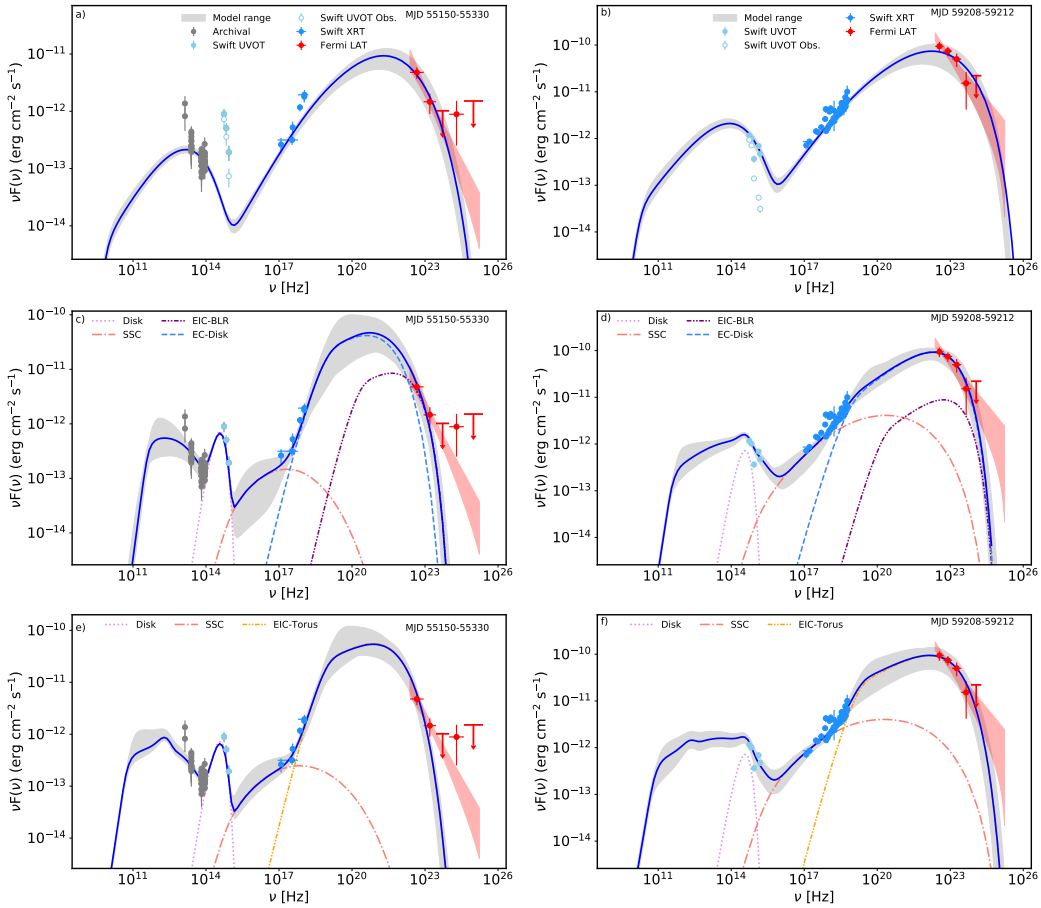

Figure 4.3: The broadband SEDs of PKS 0537-286 in the quiescent (left panels) and flaring (right panels) states. Panels a and b correspond to SED modeling when the emission is entirely due to synchrotron/SSC radiation. The SED modeling when the emission region is within the BLR is shown in panels c and d, while in panels e and f it is outside the BLR. The blue solid curve shows the sum of all components and the gray shaded area is the uncertainty region from MCMC sampling of the parameters. The color code of the other components is given in the legends. In panels a and b, the observed and absorption-corrected Swift UVOT fluxes are shown with empty and filled light blue circles, respectively.

Table 4.1: Parameters best describing the PKS 0537-286 multiwavelength emission in the scenarios shown in Fig. 4.3.

	SSC		EIC-BLR		EIC Torus	
	quiescent	flare	quiescent	flare	quiescent	flare
p	1.8 ± 0.1	1.6 ± 0.03	2.3 ± 0.2	2.2 ± 0.1	2.4 ± 0.1	2.4 ± 0.1
$\gamma_{cut}/10^3$	11.8 ± 0.8	11.5 ± 0.6	0.3 ± 0.1	2.5 ± 0.2	1.3 ± 0.1	6.7 ± 0.7
γ_{min}	9.5 ± 1.0	1.3 ± 0.1	26.1 ± 3.8	30.1 ± 2.5	65.7 ± 3.4	103.9 ± 9.0
δ	16.8 ± 1.2	24.9 ± 1.1	13.4 ± 1.3	11.4 ± 0.7	15.3 ± 0.7	14.2 ± 1.0
$B[G]$	$(9.3 \pm 0.8) \times 10^{-3}$	$(1.7 \pm 0.1) \times 10^{-2}$	3.5 ± 0.4	3.0 ± 0.2	0.2 ± 0.01	0.2 ± 0.02
$R[cm]/10^{17}$	2.0 ± 0.1	1.6 ± 0.1	0.2 ± 0.02	0.1 ± 0.01	2.0 ± 0.1	1.4 ± 0.1
$L_e[erg\,s^{-1}]$	1.2×10^{47}	1.2×10^{47}	1.3×10^{45}	2.0×10^{45}	1.1×10^{46}	1.3×10^{46}
$L_B[erg\,s^{-1}]$	3.5×10^{42}	1.8×10^{43}	2.2×10^{45}	5.3×10^{44}	1.3×10^{45}	7.9×10^{44}

4.7.2 Emitting region within the BLR

Fig. 4.3 panels c and d show the SED modeling assuming the jet dissipation occurred close to the central source. In this case, the density of disk-emitted and BLR-reflected photons in the jet frame (taking into account Doppler amplification) is comparable with or larger than that of synchrotron photons, so their inverse Compton scattering has a non-negligible contribution. The thermal emission from the accretion disk, modeled as a black body, is shown with a pink dashed line. In the quiescent state (Fig. 4.3 panel c), the low-energy component of the spectrum (up to 10^{16} Hz) can be reasonably well explained by combined synchrotron and black body components. The data in the X-ray band is mostly dominated by the EIC-disk component (blue dashed line in Fig. 4.3) with SSC contributing in the soft X-ray band, whereas the emission in the γ-ray band is due to EIC-disk and EIC-BLR components (blue dashed and purple dot-dot-dashed lines in Fig. 4.3, respectively). As compared with the synchrotron/SSC model, the distribution of the electrons is narrower with $p = 2.3 \pm 0.2$ and $\gamma_{cut} = (0.3 \pm 0.1) \times 10^3$, because the average energy of the external photons is larger than that of the synchrotron one. The Doppler boosting factor is $\delta = 13.4 \pm 1.3$ but the magnetic field is significantly larger, $B = 3.5 \pm 0.4$ G. Since the flux in the HE band depends on the photon and particle density and the content of external photons is higher (inferred from the observed high Compton dominance, i.e., the ratio between the peak flux of inverse Compton and synchrotron components), the number of emitting electrons is reduced; to produce the synchrotron emission at the same level higher magnetic field is required. The emission is produced in a more compact region with a radius of $(0.2 \pm 0.02) \times 10^{17}$ cm, smaller than $R_{BLR} = 9.3 \times 10^{17}$ cm.

During the flaring period, in the optical/UV band, the synchrotron emission from the jet dominates over the thermal emission from the accretion disk (Fig. 4.3 panel d). As the synchrotron emission extends to higher frequencies, the SSC component makes a non-negligible contribution in the X-ray band (orange dot-dashed line in Fig. 4.3 panel d). The γ-ray emission is mostly due to the EIC-disk component (blue dashed line in Fig. 4.3 panel d) and EIC-BLR contributes at higher γ-ray energies (purple dot-dot-dashed line in Fig. 4.3 panel d). In this case, the electron distribution is nearly flat with $p = 2.2 \pm 0.1$ and extends up to $(2.5 \pm 0.2) \times 10^3$. The increase of the energy up to which the electrons are effectively accelerated (γ_{cut}) resulted in the shift of the synchrotron component to higher frequencies and domination over the

disk thermal emission. The Doppler boosting is $\delta = 11.4 \pm 0.7$, the magnetic field is $B = 3.0 \pm 0.2$ G and the emission region radius is $(0.1 \pm 0.01) \times 10^{17}$ cm. This is smaller than that estimated in the quiescent state and corresponds to 1.5 days variability.

4.7.3 Emitting region outside BLR

Fig. 4.3 panels e and f show PKS 0537-286 SED modeling assuming the emission region is beyond the BLR. In the quiescent state, the HE component is entirely dominated by EIC-torus (yellow dot-dot-dashed line in Fig. 4.3 panel e) and SSC contributing in the soft X-ray band (orange dot-dashed line in Fig. 4.3 panel e). In the flaring state, the peak of the SSC component is around $\sim 10^{22}$ Hz (orange dot-dashed line in Fig. 4.3 panel f) making a non-negligible contribution to the X-ray band, but again, the HE γ-ray data is solely explained by the EIC-torus component (yellow dot-dot-dashed line in Fig. 4.3 panel f). The model parameters given in Table 4.1 show that in the quiescent and flaring states the electron distribution has a similar power-law index $p \simeq 2.4$, but in the flaring state the cut-off energy is larger, $\gamma_{cut} = (6.7 \pm 0.7) \times 10^3$ as compared to $\gamma_{cut} = (1.3 \pm 0.1) \times 10^3$. This is because *i)* the synchrotron component should extend beyond the optical/UV band and *ii)* during the flare the γ-ray spectrum is harder, shifting this component towards higher frequencies. Also, the modeling shows that the Doppler boosting and magnetic field do not substantially change, correspondingly being $\delta = 15.3 \pm 0.7$ and $B = 0.2 \pm 0.01$ G and $\delta = 14.2 \pm 1.0$ and $B = 0.2 \pm 0.02$ G for the flaring and quiescent states. However, again in the flaring state, the emission region has a slightly smaller radius $(1.4 \pm 0.1) \times 10^{17}$ cm as compared with $(2.0 \pm 0.1) \times 10^{17}$ cm.

4.7.4 Jet luminosity

The parameters estimated during the modeling are used to compute the jet luminosity. The jet power carried by the electrons, calculated as $L_e = \pi c R_b^2 \Gamma^2 U_e$, and by magnetic field, calculated as $L_B = \pi c R_b^2 \Gamma^2 U_B$, are given in Table 4.1. In the case of synchrotron/SSC scenario (Fig. 4.3 panels a and b), the jet should be strongly particle dominated with a luminosity of the order of $\simeq 10^{47}\, erg\, s^{-1}$ where the magnetic luminosity has a marginal contribution ($L_e/L_B \simeq 3 \times 10^4$). This is natural, given the SED of PKS 0537-286 in both

quiescent and flaring periods shows strong Compton dominance. Relatively high luminosity is also estimated in the modeling when the emitting region is outside the BLR; $L_e + L_B = 1.2 \times 10^{46}\, erg\, s^{-1}$ with $L_e/L_B = 8.1$ and $L_e + L_B = 1.4 \times 10^{46}\, erg\, s^{-1}$ with $L_e/L_B \simeq 17$ for the quiescent and flaring states, respectively. When the emitting region is within the BLR, a lower jet luminosity is required, $L_e + L_B = 6.3 \times 10^{45}\, erg\, s^{-1}$ and $L_e + L_B = 2.5 \times 10^{45}\, erg\, s^{-1}$ for the quiescent and flaring states, respectively, and the system is close to equipartition with $L_e/L_B = 0.5$ and $L_e/L_B = 3.7$ for the quiescent and flaring states, respectively.

Also, the total kinetic energy of the jet, defined as $L_{kin} = L_e + L_B + L_{p,cold}$, can be evaluated. Assuming a proton-to-electron comoving number density ratio of $N_p/N_e \simeq 0.1$, in the most energy demanding model (synchrotron/SSC) $L_{kin} = 3.2 \times 10^{47}\, erg\, s^{-1}$ and $L_{kin} = 4.4 \times 10^{47}\, erg\, s^{-1}$ are estimated for the quiescent and flaring states, respectively. In the most optimistic scenario (EIC-BLR), $L_{kin} = 1.1 \times 10^{46}\, erg\, s^{-1}$ and $L_{kin} = 6.0 \times 10^{45}\, erg\, s^{-1}$ for the quiescent and flaring states, respectively. In this case, even if assuming $N_p/N_e \simeq 1$, one would obtain $L_{kin} = 4.8 \times 10^{46}\, erg\, s^{-1}$ and $L_{kin} = 3.8 \times 10^{46}\, erg\, s^{-1}$ for the quiescent and flaring states, respectively. It is interesting that this luminosity is still lower than the disk luminosity estimated from the optical/UV data fitting. However, considering that the presence of the pairs can reduce the jet power [e.g., 122], the estimated jet luminosity will be by several factors lower than the accretion disk luminosity.

In **(author?)** [35], the broadband SED of PKS 0537-286 was modeled assuming the particles are injected into the emitting region, which is inside the BLR, and interact with the internal and external photon fields. The disk luminosity was estimated to be $1.7 \times 10^{47}\, erg\, s^{-1}$ and $8.4 \times 10^{46}\, erg\, s^{-1}$ by fitting the data observed in 2008 and 2006, respectively; the latter value is similar to the disk luminosity estimated in the current study. Their modeling showed that L_e is in the range of $(2.5 - 4.0) \times 10^{46}\, erg\, s^{-1}$ and L_B in $(1.0 - 2.0) \times 10^{45}\, erg\, s^{-1}$. L_e is slightly larger than that estimated in the current study (see Table 4.1) which is related with different assumptions made in the modelings (e.g., emitting region radius, Doppler boosting factor, etc.).

4.8 Summary

In this work, we have performed a broadband study of the high redshift blazar PKS 0537-286. The main findings are summarized as follows:

- PKS 0537-286 is among the highest redshift blazars detected by Fermi-LAT. Its γ-ray emission, monitored since 2008, appeared relatively constant until 2017, then multiple powerful γ-ray flares were observed. Starting from MJD 59170, the source was in an enhanced γ-ray emission state when the γ-ray luminosity reached $6.14 \times 10^{49}\, erg\, s^{-1}$. During the considered fourteen years, the γ-ray luminosity of the source exceeded $10^{49}\, erg\, s^{-1}$ for 61.8 days in total.

- The γ-ray photon index of the source varies as well. The mean of the γ-ray photon index during non flaring periods is $\simeq 2.83$ which substantially hardens during the flares: the hardest index of 2.23 ± 0.18 was observed on MJD 59322. There is a moderate anti-correlation between the γ-ray photon index and luminosity.

- The source is very luminous in the X-ray band with a $0.3 - 10$ keV luminosity between $10^{47} - 10^{48}\, erg\, s^{-1}$ and with a hard spectrum ($\Gamma_{X-ray} < 1.38$). The available NuSTAR observations show that the hard X-ray spectrum extends up to 30 keV with $\Gamma_{X-ray} = 1.26$ with a luminosity between $(0.75 - 1.40) \times 10^{48}\, erg\, s^{-1}$.

- In order to understand the underlying physical processes at work in the jet of PKS 0537-286, the SEDs during the quiescent and flaring states were reproduced using a simple one-zone leptonic emission model considering different locations of the emission region. In the quiescent state, the combined synchrotron and thermal accretion disk components can explain the IR-optical-UV data, whereas X-ray to HE γ-ray data are due to inverse-Compton scattering of the disk and BLR-reflected photons. Instead, in the flaring state, the jet synchrotron emission dominates in the optical/UV band and the X-ray to HE γ-ray emission is due to combination of SSC, EIC-disk and EIC-BLR components. The modeling in the quiescent to flaring states showed that the flare was caused by the electron distribution changes, i.e., the electron power-law index hardened to $p = 2.2 \pm 0.1$ and the cut-off energy was $\gamma_{cut} = (2.5 \pm 0.2) \times 10^3$.

- From the required jet energy point of view, the model with the emission region within the BLR is preferred. During the flaring event, the emitting region is nearly in equipartition with $L_e/L_B = 3.7$ and the jet

total luminosity is $L_{tot} = 3.8 \times 10^{46}\, erg\, s^{-1}$ when assuming a proton-to-electron comoving number density ratio of $N_p/N_e \simeq 1$. This luminosity is slightly lower than the accretion disk luminosity of $L_{disc} = 8.7 \times 10^{46}\, erg\, s^{-1}$ estimated through fitting of UV/optical data.

Among the high red-shift blazars, PKS 0537-286 is exceptional, having a reach multiwavelength data set (especially in the X-ray and γ-ray bands) which allows to investigate the processes taking place in the jet. Further multiwavelength monitoring of such distant and powerful sources will improve our understanding of the radiative processes at work in the relativistic jets in the early Universe.

5 Quasi-periodic oscillations in the γ-ray light curves of bright active galactic nuclei

5.1 Introduction

Super-massive black holes (SMBHs) dwell at the center of all galaxies, and when accreting material they are observed from Earth as active galactic nuclei (AGNs). In a minority of AGNs the accretion of matter onto the black hole is associated with the launching of a pair of relativistic jets of plasma along the polar axis [see 32, for a recent review]. Studying the inflows and outflows of matter on and from black holes provides an indirect access to the physics of these compact objects.

SMBHs have their low-mass analog in stellar-mass black holes produced in star collapses. These low-mass black holes, when in binary systems, have also been observed accreting surrounding matter and launching plasma jets. These systems are observationally classified as X-ray binaries and microquasars. A peculiar characteristic of X-ray binaries is the presence of quasi-periodic oscillations (QPOs) in their X-ray light curves, with periods of the order of 0.1-10 Hz [see e.g. the review by 83, and references therein]. Such a period is consistent with the innermost stable orbit of the black hole and suggests that QPOs can be used to access the region closest to the horizon and to study the physics of black hole accretion. Given the analogy between stellar-mass black holes and SMBHs, QPOs are also expected in the latter, although with much longer periods due to the larger size of the Schwarzschild radius that scales linearly with the mass of the compact object. Several observational claims have been made for QPOs in the X-ray light curves of Seyfert galaxies (radio-quiet AGNs), with periods of the order of hours [72, 17]. The much longer periods in AGNs make it difficult to unequivocally measure QPOs in

their light curves: an uninterrupted sampling over several periods is needed in order to have a statistically significant measurement.

In the last decade the *Fermi*-LAT instrument [22] has revolutionized our view of the γ-ray sky in the 100 MeV-100 GeV band thanks to its unprecedented sensitivity and all-sky monitoring observing strategy. Fourteen years after its launch we have now access to continuous light curves on hundreds of AGNs. In the GeV band the extra-galactic sky is dominated by a peculiar AGN class: blazars. Blazars are AGNs whose relativistic jet is closely aligned with our line of sight. The relativistic Doppler effect boosts the emission and makes these type of AGNs among the brightest sources in the Universe. From an observational point of view, blazars are divided into two sub-classes: BL Lacertae objects (BL Lacs for short), with weak or absent broad emission lines in their optical/UV spectrum; and Flat Spectrum Radio Quasars (FSRQs), with strong broad emission lines [161].

Searches for periodicities in the light curves of *Fermi*-LAT blazars have been an active research topic since the beginning of the mission but the first claim had to wait six years of data taking: **(author?)** [7] presented the first evidence (at about 3σ) for a periodic 2-years modulation in the light curve of the blazar PG 1553+113, coincident in period with a QPO seen at longer wavelengths. Interestingly, this first hint for a QPO in a blazar γ-ray light curve is at frequencies much lower than the ones detected in X-rays in Seyfert galaxies, suggesting that its origin is intrinsically different. Since 2015, several research groups have investigated QPOs in *Fermi*-LAT light curves resulting in several positive claims. All γ-ray QPO candidates in blazars shown a period of the order of years. A notable exception is represented by the highly-significant (5.2σ) QPO seen in PKS 2247-131 which has a period of about a month and, most importantly, seems to be a transient phenomenon [176].

The details of the radiative mechanism(s) at the origin of the γ-ray emission in blazars are a subject of investigation, but there is consensus on the fact that this high-energy emission is produced in the relativistic jet and far from the SMBH [see 42, for a recent review on blazar emission models]. The physical mechanisms for the production of QPOs in γ-ray blazars will thus be intrinsically different from the ones at work in radio-quiet AGNs, and linked to the physics of jets. Several models have been developed to explain these quasi-periodicities. They can be associated to the movement of plasmoids in the jet

along helical paths [128], or related to precession of the jet itself. This precession could be driven by the gravitational perturbation of another SMBH [26, 152], meaning that QPOs will provide key constraints on SMBH binaries in the Universe. SMBH binaries are expected to form during galaxy mergers, and it is thus clear how important their detection is to understand galaxy and SMBH evolution through the history of the Universe. Alternatively, the periodicities could be related to a regular change in the accretion of matter onto the SMBH that is then translated into a QPO in the γ-ray emission in the jet. In this case as well, SMBH binaries can be the source of this periodicity via perturbation of the accretion flow [162]. The SMBH binary can also imprint a QPO in the light curve via gravitational stresses by one of the black holes on the jet of the other one [154]. The most promising SMBH binary candidate identified thanks to a twelve-years QPO in its optical light curve is the blazar OJ 287 [151]. The source is a known γ-ray emitter, but its famous 12-years QPO has not been seen in its *Fermi*-LAT light curve due to the long period, although claims of a γ-ray QPO with a period of about 300 days have been made [91].

The goal of this work is to systematically study the light curves of bright *Fermi*-LAT AGNs in order to identify QPO candidates. In order to get access to transient QPOs, and QPOs with varying periods that could be hidden in a time-integrated power spectral density, we make use of the continuous wavelet transform. The paper is organized as follows: in Section 5.2 we discuss the selection of the targets; in Section 5.3 we provide the details of the *Fermi*-LAT data analysis; in Section 5.4 we describe the wavelet analysis, whose results are presented in Section 5.5; the discussion and the conclusions are in Sections 5.6 and 5.7.

5.2 Sources

The only selection criterion applied is for the source to be bright enough to have continuous *Fermi*-LAT light curves with time bins of seven days or one month. The main issue is to avoid the effect of large gaps in the continuous wavelet transform (see Section 5.4). This aspect, together with the need to limit the total computing time, drives the choice to limit the analysis to the thirty-four brightest sources in the 4LAC catalog [data release 2, 13, sorting

them by integral energy flux above 100 MeV and removing sources with a test significance lower than 100]. The least bright source has an integral flux above 100 MeV equal to 8.95×10^{-11} erg cm^{-2} s^{-1}. The only exception in our source selection is represented by PKS 2247-131, which is manually added to our list due to the high significance QPO detected in this source by **(author?)** [176]. The source was not detected by *Fermi*-LAT before entering in an active state in 2016, and thus its long-term average flux is biased towards lower values. If we consider only its emission after 2016, this source is definitely among the brightest γ-ray AGNs, and clearly fulfills our requirement to have an uninterrupted light curve. This manual addition brings the total of our sample to thirty-five AGNs. The sources we included in our analysis are listed in Table 5.1 by their Right Ascension. The sample consists of 19 FSRQs, 15 BL Lacs, and 1 radio galaxy. For each source, together with the source name and 4FGL name, we provide the source class, coordinates in J2000 and the redshift (the three last quantities as provided in the 4LAC catalog).

5.3 Fermi/LAT Data Analysis

The Large Area Telescope (LAT) on board the Fermi Gamma-ray Space Telescope is a pair conversion telescope sensitive to γ-rays in the energy band from 20 MeV to 500 GeV. Since its launch on June 11, 2008, *Fermi*-LAT scans the sky every $\sim$3 hours, regularly monitoring the γ-ray emission from different sources. More details on the *Fermi*-LAT instrument are described in **(author?)** [22] and references therein.

In the current study, γ-ray data from the observation of the considered sources from August 8, 2008 to April 4, 2021 (from MJD 54686 to MJD 59308) were downloaded and analyzed using the standard analysis procedure provided by the *Fermi*-LAT collaboration. The data for each of the considered sources are analyzed in an identical manner. The Pass 8 data in the energy range from 100 MeV to 500 GeV are analyzed using Fermi ScienceTools (1.2.1) and the P8R3_SOURCE_V3 instrument response functions. We selected only events within a maximum zenith angle of 90°, to reduce contamination by photons from Earth's atmosphere and used the filter expression (DATAQUAL >0) and (LAT CONFIG==1) to select good time intervals. The photons from a circular region with a radius of 12° around each source under

consideration were selected. Then, the events are binned within a $16.9^\circ \times 16.9^\circ$ square region of interest (ROI) into $0.1^\circ \times 0.1^\circ$ pixels and into 37 equal logarithmically spaced energy bins. The model for which the likelihood is computed includes a combination of point-like and diffuse sources and standard templates describing the diffuse emission from the Galaxy (gll_iem_v07) and the isotropic γ-ray background (iso_P8R3_SOURCE_V3_v1). The model file for each source is created using the *Fermi*-LAT fourth source catalog [4FGL; 5] where all sources falling within ROI+5° were all included with the same spectral models as in the catalog. The normalization parameters of the diffuse Galactic and the isotropic component, and both the normalization and spectral parameters of the point sources within the ROI were set as free parameters while that of the sources outside ROI were fixed to the catalog values. The binned likelihood analysis implemented in gtlike tool is used to optimize the parameters to best match the observations for the whole time period.

The model file obtained from the full time analysis is used to compute the light curves. We produced the light curves binned into weekly and monthly intervals by applying unbinned likelihood analysis in the 0.1–300 GeV energy range with the appropriate quality cuts mentioned above.

5.4 Wavelet Analysis

5.4.1 Continuous Wavelet Transform

In this work we make use of the continuous wavelet transform (CWT) technique, which is the convolution of a time series with a dilated and translated wavelet function, to analyse time-frequency properties of the light curves. Acting as a band-pass filter, the CWT maps the power of any particular periodic behaviour at different times in the time-frequency space. This is notably useful, since the CWT technique not only gives access to the frequencies of potential QPOs, but also when the periodicities appear and end, and how they evolve in time.

We use the Python implementation `PyCWT` provided by **(author?)** [156] and as mother wavelet the Morlet wavelet. This wavelet consists of a plane wave modulated by a Gaussian and is shown in **??**. The *wavelet power spectrum* is

Source name	4FGL name	Source class	R.A. (J2000)	Dec. (J2000)	Redshift
4C +01.02	J0108.6+0134	FSRQ	$01^h08^m40.7^s$	$+01^d34^m54.8^s$	2.099
3C 66A	J0222.6+4302	BL Lac	$02^h22^m40.7^s$	$+43^d02^m08.5^s$	0.444
4C +28.07	J0237.8+2848	FSRQ	$02^h37^m53.7^s$	$+28^d48^m15.8^s$	1.206
PKS 0235+164	J0238.6+1637	BL Lac	$02^h38^m40.3^s$	$+16^d37^m04.4^s$	0.94
NGC 1275	J0319.8+4130	RDG FR-I	$03^h19^m49.8^s$	$+41^d30^m43.6^s$	0.018
PKS 0402-362	J0403.9-3605	FSRQ	$04^h03^m54.0^s$	$-36^d05^m13.2^s$	1.417
PKS 0426-380	J0428.6-3756	BL Lac	$04^h28^m41.5^s$	$-37^d56^m25.1^s$	1.11
PKS 0447-439	J0449.4-4350	BL Lac	$04^h49^m26.0^s$	$-43^d50^m06.0^s$	0.205
PKS 0454-234	J0457.0-2324	FSRQ	$04^h57^m02.6^s$	$-23^d24^m53.6^s$	1.003
PKS 0537-441	J0538.8-4405	BL Lac	$05^h38^m50.1^s$	$-44^d05^m10.3^s$	0.892
S5 0716+714	J0721.9+7120	BL Lac	$07^h21^m57.2^s$	$+71^d20^m25.8^s$	0.300
4C +55.17	J0957.6+5523	FSRQ	$09^h57^m39.9^s$	$+55^d23^m01.7^s$	0.896
1H 1013+498	J1015.0+4926	BL Lac	$10^h15^m04.3^s$	$+49^d26^m01.0^s$	0.212
S5 1044+71	J1048.4+7143	FSRQ	$10^h48^m25.6^s$	$+71^d43^m46.9^s$	1.15
Mrk 421	J1104.4+3812	BL Lac	$11^h04^m28.5^s$	$+38^d12^m25.2^s$	0.03
4C +21.35	J1224.9+2122	FSRQ	$12^h24^m54.6^s$	$+21^d22^m53.0^s$	0.434
3C 273	J1229.0+0202	FSRQ	$12^h29^m04.2^s$	$+02^d02^m43.4^s$	0.158
3C 279	J1256.1-0547	FSRQ	$12^h56^m10.0^s$	$-05^d47^m19.3^s$	0.536
B3 1343+451	J1345.5+4453	FSRQ	$13^h45^m34.6^s$	$+44^d53^m03.8^s$	2.534
PKS 1424+240	J1427.0+2348	BL Lac	$14^h27^m0.4^s$	$+23^d48^m0.6^s$	0.601
PKS 1424-418	J1427.9-4206	FSRQ	$14^h27^m56.8^s$	$-42^d06^m21.6^s$	1.522
PKS 1502+106	J1504.4+1029	FSRQ	$15^h04^m24.8^s$	$+10^d29^m52.1^s$	1.839
PKS 1510-089	J1512.8-0906	FSRQ	$15^h12^m51.5^s$	$-09^d06^m23.0^s$	0.36
B2 1520+31	J1522.1+3144	FSRQ	$15^h22^m10.9^s$	$+31^d44^m22.2^s$	1.489
PG 1553+113	J1555.7+1111	BL Lac	$15^h55^m43.5^s$	$+11^d11^m18.2^s$	0.36
4C +38.41	J1635.2+3808	FSRQ	$16^h35^m16.0^s$	$+38^d08^m24.4^s$	1.814
Mrk 501	J1653.8+3945	BL Lac	$16^h53^m53.7^s$	$+39^d45^m34.2^s$	0.033
1ES 1959+650	J2000.0+6508	BL Lac	$20^h00^m02.6^s$	$+65^d08^m52.5^s$	0.047
PKS 2155-304	J2158.8-3013	BL Lac	$21^h58^m51.4^s$	$-30^d13^m30.4^s$	0.116
BL Lac	J2202.7+4216	BL Lac	$22^h02^m46.7^s$	$+42^d16^m55.6^s$	0.069
CTA 102	J2232.6+1143	FSRQ	$22^h32^m36.6^s$	$+11^d43^m50.2^s$	1.037
PKS 2247-131	J2250.0-1250	BL Lac	$22^h50^m01.2^s$	$-12^d50^m54.6^s$	0.22
3C 454.3	J2253.9+1609	FSRQ	$22^h53^m59.1^s$	$+16^d09^m02.2^s$	0.859
PKS 2326-502	J2329.3-4955	FSRQ	$23^h29^m19.1^s$	$-49^d55^m56.6^s$	0.518
PMN J2345-1555	J2345.2-1555	FSRQ	$23^h45^m12.7^s$	$-15^d55^m05.5^s$	0.621

Table 5.1: The selected *Fermi*-LAT sources with the catalog name, blazar type, coordinate in J2000 and redshift extracted from the *Fermi*-LAT 4FGL catalog.

defined as the square of the amplitude of the wavelet coefficient. The *global wavelet spectrum* can then be computed as the time-average of the wavelet spectrum. The global wavelet spectrum provides an unbiased and consistent estimation of the true power spectrum of a time series [119]. Because of the finite length of the time series, border effects occur at the edges of the wavelet power spectrum. The cone of influence (COI) is defined as the region of the wavelet power spectrum in which edge effects become important, and is calculated as suggested by [156].

In **??** we show the CWT map and global wavelet spectrum of a periodic signal with two periods at 0.1 and 0.02 s (Fig. **??**) and a Dirac delta signal (Fig. **??**). The CWT has an intrinsic resolution in reconstructing a periodic signal, that can be visualized as broad bands in the CWT map. We estimate this uncertainty as half of the full-width at half-maximum (FWHM) of the global wavelet spectrum. For the Dirac delta function, a vertical feature appears in the wavelet power spectrum which reveals the response of this technique when a flare-like signal is present in the light curve. This response of the CWT to flares is of particular relevance for our study. A high power in the CWT by itself does not mean that a periodicity is present in the light curve: all CWT maps have to be inspected to visually confirm that the power is distributed horizontally, and is not related to a flaring behaviour.

5.4.2 Significance Estimation

To determine the significance and confidence levels of the analysis, we simulated artificial light curves following the work by **(author?)** [57], using the Python version provided by **(author?)** [48]. This algorithm generates artificial light curves having the same power spectral density (PSD) and probability distribution function (PDF) as the original light curve and represents an improvement of the procedure of [155], which produces normally distributed time series from a given PSD. The algorithm of [57] is able to precisely reproduce light curves which match both the PSD and the PDF of a given observed light curve or a theoretical model, where the PSD estimate is performed using a maximum likelihood methodology, and assuming a smoothly bending power-law model plus a constant.

For each *Fermi*-LAT light curve, we produced 10000 artificial light curves. In **??** we show a comparison of the PDF and PSD of one of the simulated light curve to the original one. The global wavelet spectrum is computed for each simulated light curve, such that a histogram of the power spectrum can be produced at every period, or scale. We then fit the histogram with a χ^2 distribution with k degrees of freedom

$$\chi(x,k)^2 = \frac{1}{2^{k/2}\Gamma(k/2)} x^{k/2-1} \exp(-x/2). \tag{5.4.1}$$

The confidence levels are obtained by using the percentiles of the power for each scale, which define the global significance of the results. An example of the χ^2 fitting to the histogram is included in **??**, as well as the resulting confidence levels for the AGN S5 0716+714.

When searching for significant results in physics, one needs to take into account the "look-elsewhere effect", which can be quantified in term of number of trials. We estimate the post-trial confidence levels of the global and local wavelet spectrum following the work presented by [23]. Taking into account the fact that the bins in the wavelet spectrum are not statistically independent, they showed that the post-trial probability P_G can be computed from the pre-trial one P_L as:

$$P_G = 1 - (1 - P_L^a)^n, \tag{5.4.2}$$

where a and n are empirically derived coefficients, which are relate to the number of bins in the spectrum and the resolution of the CWT that we are using δj, and are specific for each mother wavelet. The resolution δj in our analysis is $1/12$. Different parameterization for the global and local wavelet spectrum are needed, since in the local one, trials are made in the time-period bins of the power spectrum map, whereas after the time-average, only the period bins accounts for the global wavelet spectrum. [23] parameterized $a = 0.810\ (N_{out}\ \delta j)^{0.011}$ and $n = 0.491\ (N_{out}\ \delta j)^{0.926}$ for the local wavelet spectrum, and $a = 0.805 + 0.45 \times 2^{-S_{out}\delta j}$ and $n = 1.136\ (S_{out}\ \delta j)^{1.2}$ for the global one, where N_{out} and S_{out} are the time-period bins and the period bins of the wavelet spectrum outside the COI respectively. These coefficients are valid for time series affected by power-law noise, but adequate only for wavelet analysis using the Morlet wavelet [for more details see 23].

Additionally, we are considering 35 sources in this work and 2 time-binnings for each of them. Therefore, for each time-binning, we compute the number of bins N_{out} and S_{out}, and we multiply them to the number of sources in order to account the total number of trials made. One special case is the AGN PKS 2247-131, whose light curve is cut at MJD 57427, since there was no detection by *Fermi*-LAT before that date. Hence, the number of time-period bins N_{out} for this source is lower.

The total number of bins $N_{out,T}$ and $S_{out,T}$ are, thus, computed as:

$$\begin{aligned} N_{out,T} &= (34 \times N_{out,1month} + N_{out,1month}^{PKS\ 2247-131}) + \\ &\quad + (34 \times N_{out,7days} + N_{out,7days}^{PKS\ 2247-131}) \ = 1698893, \\ S_{out,T} &= (34 \times S_{out,1month} + S_{out,1month}^{PKS\ 2247-131}) + \\ &\quad + (34 \times S_{out,7days} + S_{out,7days}^{PKS\ 2247-131}) \ = 4833. \end{aligned} \tag{5.4.3}$$

5.5 Results

In this section we present the results for those light curves showing possible QPOs and we discuss in more details the five sources exhibiting the most significant features: 4C +01.02, PKS 0537-441, S5 1044+71, B2 1520+31 and PKS 2247-131. Furthermore, results consistent with previous QPO searches are also found in several sources, although at lower significance: PKS 0426-380, S5 0716+714, Mrk 421, PKS 1424-418, Mrk 501 and PKS 2155-304. These results are also commented briefly in this Section, although their CWT maps will be provided together with all the remaining sources in **??**. Table 5.2 lists the candidate QPOs found by CWT.

We identify a total of 36 QPO candidates in 24 out of the 35 selected sources. We consider candidates that have a post-trial significance larger than 3σ in at least one of the two binnings, and that show at least three complete cycles once fitted. Long term QPO candidates with periods longer than and

Source	Period(d) 30 d LC	Significance (σ)	Period(d) 7 d LC	Significance (σ)	Nr. fitted cycles
4C +01.02	268±55	> 5	268±54	> 5	4
	123±26	4.7	122±26	> 5	5
PKS 0537-441	285±67	> 5	286±73	> 5	4
S5 1044+71	1133±229	4.9	1127±226	4.6	3
	116±33	> 5	117±38	> 5	4
B2 1520+31	176±48	> 5	179±42	> 5	6
			71±15	> 5	14
			39±11	> 5	17
PKS 2247-131	217±38	> 5	214±43	> 5	6
			34±13	> 5	10
4C +28.07	230±90	> 5	244±88	> 5	3
NGC 1275	282±84	3.3	247±63	> 5	3
			92±33	> 5	4
PKS 0402-362	221±56	> 5	221±60	> 5	3
			122±42	> 5	5
PKS 0426-380			85±26	> 5	8
PKS 0447-439	120±37	> 5	111±42	> 5	7
PKS 0454-234			69±21	> 5	4
S5 0716+714	325±75	2.4	324±77	3.2	5
1H 1013+498	263±52	> 5	264±59	4.9	4
			100±25	> 5	4
			52±15	> 5	12
Mrk 421	300±64	> 5	300±65	> 5	3
4C +21.35			66±17	> 5	6
3C 273	177±36	> 5	177±38	> 5	4
	99±26	> 5	97±25	> 5	3
3C 279	102±26	> 5	101±27	> 5	6
			40±8	> 5	4
PKS 1424-418	94±25	> 5	90±22	> 5	5
PKS 1510-089	119±31	> 5	120±36	> 5	3
Mrk 501	315±98	2.9	326±76	> 5	7[a]
PKS 2155-304	334±107	2.2	341±106	3.5	4
CTA 102	370±85	> 5	366±81	> 5	3
	179±40	> 5	178±40	> 5	5
3C 454.3	117±23	> 5	120±27	> 5	4
PMN J2345-1555	197±50	> 5	191±44	> 5	4

Table 5.2: QPOs candidates identified by the CWT of the *Fermi*-LAT light curves in time bins of 30 days and 7 days.

[a] Number fitted cycles observed only in the weekly binned light curve.

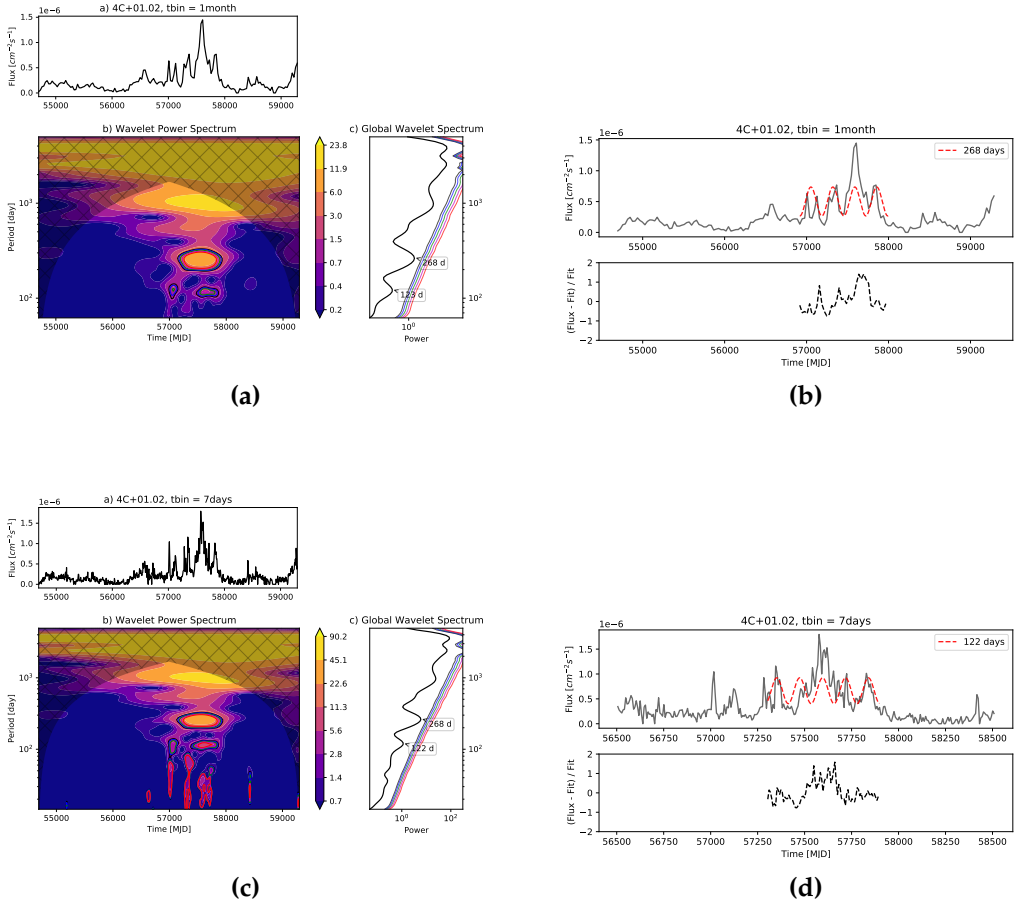

Figure 5.1: Left: CWT map for the monthly binned (upper) and the weekly binned light curve (bottom) for 4C +01.02. In each subplot, the panels represent a) Fermi/LAT light curve, b) wavelet power spectrum and c) global wavelet power spectrum. The solid coloured contours in b) and the dashed coloured lines in c) are the confidence levels (1 to 5 σ in black, blue, green, violet, and red). Right: monthly binned and weekly binned light curves with the fitted periodic signal in red dashed line in the upper panels and the relative error in the bottom panels.

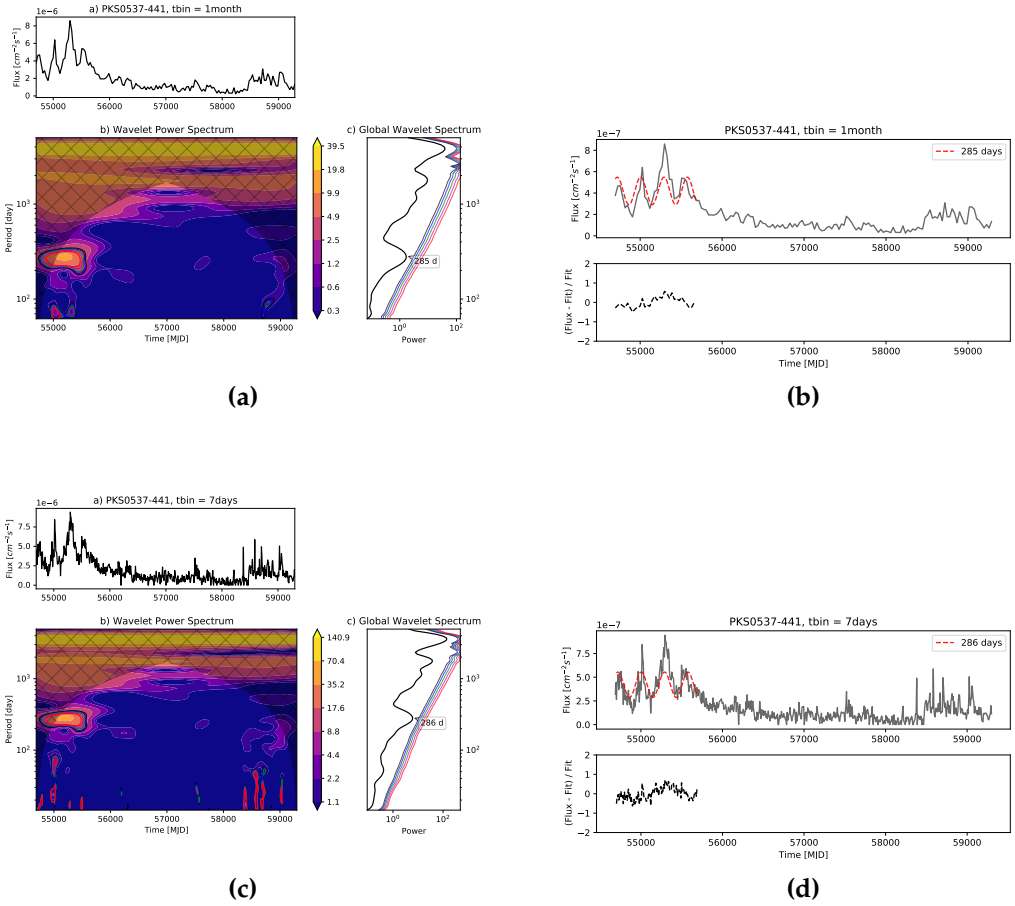

Figure 5.2: Same description as Fig. 5.1 for PKS 0537-441.

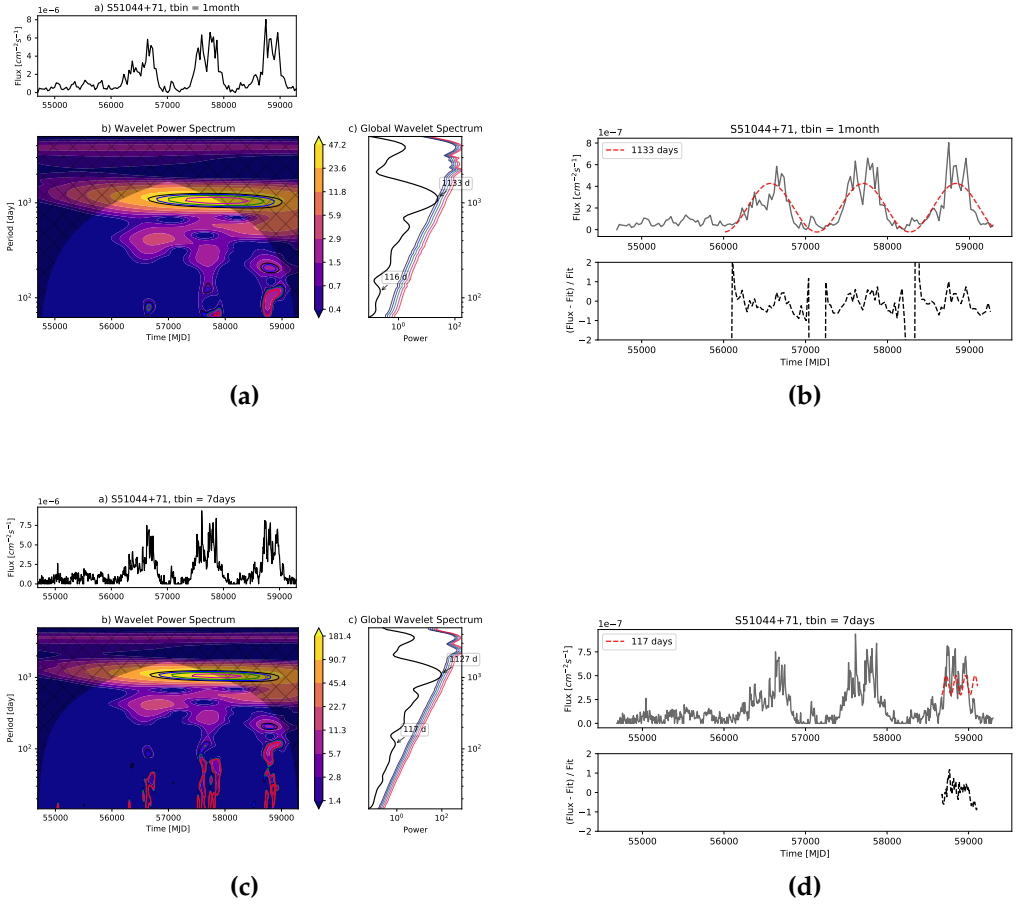

Figure 5.3: Same description as Fig. 5.1 for S5 1044+71.

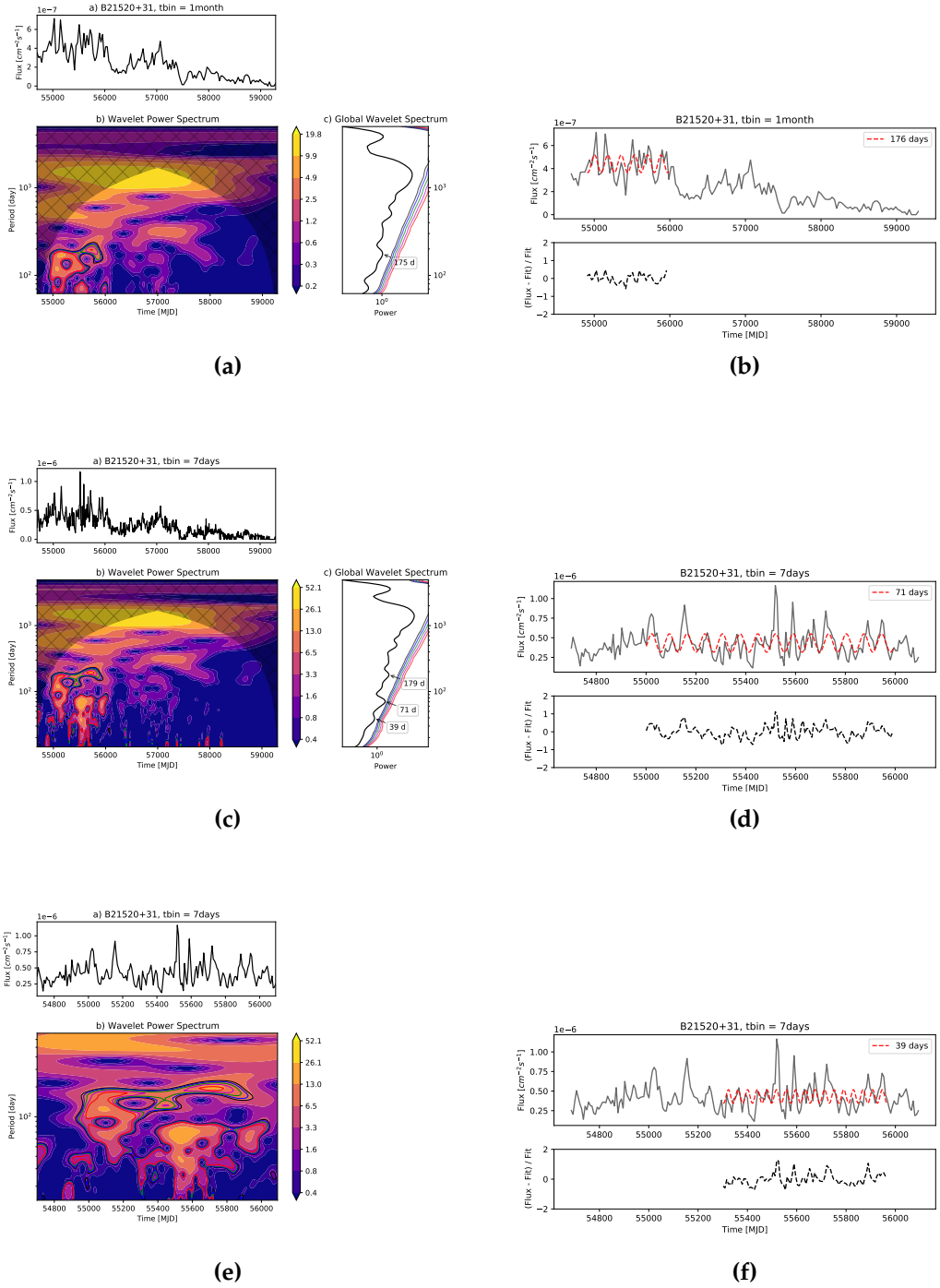

Figure 5.4: Same description as Fig. 5.1 for B2 1520+31 for the upper 4 figures. The third CWT is computed with the weekly binned light curve cut from MJD 54697 to MJD 56100. And on the right, the respective fitted light curve to show the ∼39 d period.

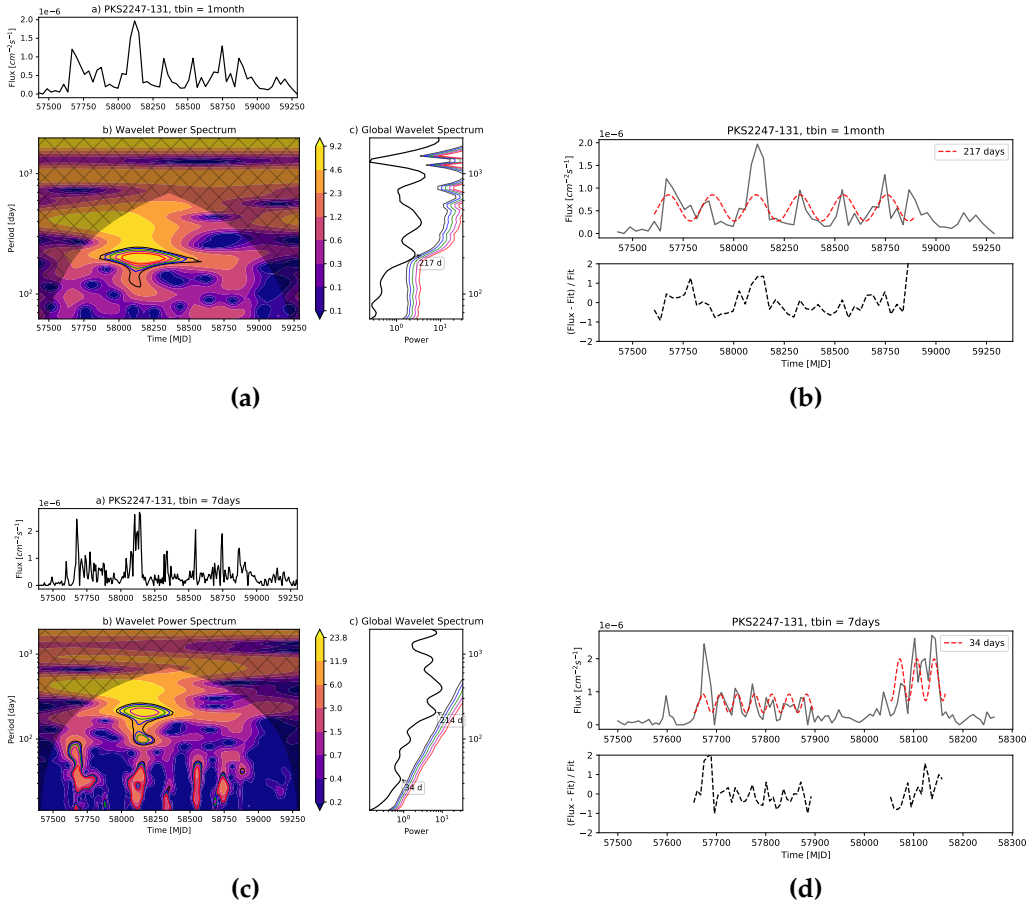

Figure 5.5: Same description as Fig. 5.1 for PKS 2247-131. In the bottom fitted light curve we show a possible reappearance of the candidate QPO with $\sim$34 d period at MJD 58050 adding 3 more cycles to the series.

around one year are observed at various significance levels in 5 sources: S5 0716+714, S5 1044+71, Mrk 421, Mrk 501, PKS 2155-304 and CTA 102. On the other hand, month-long QPO candidates with period less than $\sim$300 d can be identified in the following 20 sources: 4C +01.02, 4C +28.07, NGC 1275, PKS 0402-362, PKS 0426-380, PKS 0447-439, PKS 0454-234, PKS 0537-441, 1H 1013+498, S5 1044+71, 4C +21.35, 3C 273, 3C 279, PKS 1424-418, PKS 1510-089, B2 1520+31, CTA 102, PKS 2247-131, 3C 454.3 and PMN J2345-1555. We report no QPO detection in the γ-ray emission of sources 3C 66A, PKS 0235+164, 4C +55.17, B3 1343+451, PKS 1424+240, PKS 1502+106, PG 1553+113, 4C +38.41, 1ES 1959+650, BL Lac and PKS 2326-502.

The wavelet power spectra of the five more significant sources are shown in Figures 5.1, 5.2, 5.3, 5.4, and 5.5 . Additionally, to help visualizing the QPO candidates identified by the CWT, we fitted periodic functions with periods equal to the ones computed via the CWT, to the *Fermi*-LAT light curves. Here follows a detailed description of these results.

5.5.1 4C +01.02

The wavelet analysis shows two significant QPO candidates in the light curves of 4C +01.02, a distant FSRQ at z=2.099 (see Fig. 5.1(A) and (C)). No previous report of QPO analysis is found for this source in the literature. Both QPOs have month-long periods, with the longer one centered at 286 ± 55 d (268 ± 54 d), and the shorter one at 123 ± 26 d (122 ± 26 d), in the monthly (weekly) binned light curves. The significance of the longer QPO is over 5σ in both time binnings, whereas the shorter QPO has a significance $\sim 4.7\sigma$ for the monthly binned light curve, and larger than 5σ for the weekly binned light curve. The fitted light curves in Fig. 5.1(B) and (D) present four complete cycles for the first QPO, starting from around MJD 56900 to MJD 58000 (August 2014 to September 2017), and five complete cycles for the second QPO, between MJD 57300 and MJD 57900 approximately (October 205 and May 2017). Tinier structures also appear at lower periods, although with more vertical and ambiguous shapes, which are inevitably produced by small flares (see for example the signals found between MJD 57500 and MJD 58000 at periods ¡50 d). We did not include these among our results due to their shortness and unclear shape, but this is a very subjective criteria, and these features could

be investigated further with finer time bins.

5.5.2 PKS 0537-441

We identify a significant QPO candidate in this BL Lac object at z=0.892 (see Fig. 5.2(A) and (C)). The wavelet spectrum shows a clear horizontal feature centered at period 285 ± 67 d (286 ± 73 d) in the monthly (weekly) binned light curve, at a significance above 5σ in the CWT map of both time binnings. This result is consistent with [143], who claimed a candidate QPO at $\sim$280 d in the first few years of *Fermi*-LAT data, using the Lomb Scargle periodogram (LSP) technique. We can see four complete cycles of oscillation during a period of high γ-ray flux starting from the beginning of *Fermi*-LAT observations till around MJD 55700 (May 2011). The cycles are also shown in the fitted light curves in Fig. 5.2(B) and (D)).

5.5.3 S5 1044+71

We identify, for the first time, two highly significant QPO candidates in S5 1044+71, a moderately distant (z=1.15) FSRQ. The two CWTs are shown in Fig. 5.3(A) and (C). A very evident long term oscillation of period 1134 ± 226 d (1127 ± 224 d) at a conficence level $\sim 4.9\sigma$ ($\sim 4.6\sigma$) for the monthly (weekly) binned light curve appears in the wavelet map, emerging around MJD 56000 (March 2012). Secondly, a short month-long QPO emerged during the last flaring state of the source, between MJD 58650 and MJD 59000 (June 2019 and September 2020), with a period estimated to be 116 ± 33 d (117 ± 38 d) for the monthly (weekly) binned light curve at a significance more than 5σ. Three complete cycles of the year-long QPO can be observed also in the fitted light curve in Fig. 5.3(B), which corresponds to the large flaring states of the FSRQ. The last maximum occurred at around MJD 58800 (November 2019), so we expect the next maximum to occur at approximately MJD 59900 (November 2022). The absence of a clear fourth peak at around MJD 55500 might indicate additional modulation.[1] Regarding the short period QPO, four cycles are indicated in

[1] During the writing of this manuscript, an analysis of S5 1044+71 has been presented in a pre-print by [164], claiming a 3 years modulation ($\sim 3.06 \pm 0.43$ yr) at a significance level of $\sim 3.6\sigma$. This result is in total agreement with ours.

the fitted light curve in Fig.5.3(D), which are the three narrower flares in the last flaring state and a fourth more suppressed one after MJD 59000. This kind of structured flares are not unique in this last flaring state, but could also appear in the two previous maxima. These signals have however a more complex and vertical shapes, which causes ambiguity. If real, they could also suggest a trend towards longer periods. One can also notice in the weekly CWT maps hints (2σ at most) of several horizontal features at longer periods, which remain however consistent with noise once corrected for trials.

5.5.4 B2 1520+31

Three possible month-long QPOs are identified by the CWT of the light curves of this distant (z=1.489) FSRQ, as shown in Fig. 5.4(A), (C) and (E). The CWT maps of this source are a good example of the inherent difficulty of this analysis technique when dealing with blazar light curves: rapid flares result in vertical structures in the map that overlap with the horizontal bands we are interested into, and require visual inspection of all peaks that appear in the global wavelet spectrum. The first QPO candidate is found in both light curves at around 174 ± 48 d (179 ± 42 d) for the monthly (weekly) binned light curve with a significance above 5σ in both cases. This QPO candidate is of particular interest because its period seems to increase with time. The second and third candidate QPOs can be better identified in the CWT map of the weekly binned light curve, with periods of 71 ± 15 d and 39 ± 11 d, both exceeding 5σ significance. A zoomed-in CWT is shown in Fig. 5.4 (E), which allows us to visualize better the signal of the two very short period QPO candidates. The 71 ± 15 d period is compatible with the one reported by [77] with a period of $\sim$71 d, by analysing the first 4 years of *Fermi*-LAT data of B2 1520+31 using the LSP and weighted wavelet z-transform (WWZ) techniques. The source has also been studied by **(author?)** [153]: although some signal can be seen in their analysis at around $\sim$70 d, it remains below the 3σ interval they compute.

Fitted light curves are presented in the right hand side of Fig. 5.4. Fig. 5.4 (B) shows a periodic function of $\sim$176 d with six cycles between MJD 54900 and MJD 56000 (March 2009 and March 2012); in Fig. 5.4 (D) we can see 14 oscillations of $\sim$71 d spanning from MJD 55000 to MJD 56000 (June 2009 to

March 2012), and Fig. 5.4 (E) shows a fit with 17 cycles of period ∼39 d between MJD 55300 and 55970 (April 2010 and February 2012). A forth QPO could be also considered at a period halfway between ∼71 d and ∼176 d, which is visible in both the CWT map and the global wavelet spectrum of the weekly binned light curve. Furthermore, the ∼39 d period seems to also be present before the above mentioned time span, between around MJD 54800 and MJD 55000.

5.5.5 PKS 2247-131

The wavelet analysis of PKS 2247-131, a BL Lac object at z=0.22, shows two QPO candidates (see Fig. 5.5(A) and (C)). The first of the QPO candidates is found to be at around 217 ± 38 d (214 ± 43 d), at above 5σ confidence level in the CWT of monthly (weekly) binned light curves. This QPO candidate seems to span at least from MJD 57600 to MJD 58500 approximately (July 2016 to January 2019) in the CWT map. Just by looking at the light curve one can notice the tentative periodic oscillations of this source. And this can be confirmed by the fitted function shown in Fig. 5.5(B), presenting 6 peaks including the one at around MJD 58750.

More interestingly, we identify a QPO candidate in the time interval around MJD 57600 to MJD 57900 approximately (July 2016 to May 2017) with much shorter period. We can appreciate it in Fig. 5.5(C) which shows the QPO centered around 34 ± 14 d, with a significance larger than 5σ, and only noticeable in the full-range weekly binned light curve. Tentative oscillations can also be seen, with at least 7 full cycles, shown in Fig. 5.5(D) with the fitted periodic function. In addition, with a more detailed evaluation one can notice that the ∼34 d period reappears after MJD 58000 (September 2017). This is also shown in the fitted light curve in (D), with 3 more cycles spanning MJD 58050 to MJD 58170 approximately.

In November 2018, two years after the *Fermi*-LAT announcement of detection of this BL Lac type blazar, [176] presented the first claim of a month-scale QPO in the γ-emission of PKS 2247-131. They found a relatively short, month-scale oscillation at period 34.5 ± 1.5 d, which can be indicative of the presence of an SMBH binary in the center of this blazar. This discovery conducted us to explore the CWT of PKS 2247-131 more deeply. Small features

like this one also appear in several other sources which are included in **??**, but we do not systematically inspect all of them. The short QPO candidate in our analysis is compatible with the aforementioned one proposed by [176]. On the other hand, no previous claims for the longer QPO candidates at periods of around 220 d have been reported in the literature.

5.5.6 Other sources

In the remaining 27 sources showing QPO candidates, we found several candidates compatible with previously reported claims in the literature. The CWT maps and fitted light curves of these AGNs can be found in **??**.

- S5 0716+714: We found a QPO candidate in both the 1-month and 7-days binned light curves of this BL Lac object, centered at 325 ± 75 d (324 ± 77 d), at $\sim 2.4\sigma$ ($\sim 3.2\sigma$) in the wavelet spectrum of the monthly (weekly) binned light curve. This feature only appears in the time interval between MJD 56000 and MJD 57500 approximately (March 2012 to April 2016). Our result is compatible with the analyses by several authors: [124] reported a QPO evidence at $\sim$346 d, [93] detected a periodic feature at $\sim$344 d, [29] found a QPO candidate at around 340 d and [118] identified a period at $\sim$0.9 yr. However, [51] and [178] claim the absence of any periodic emission in this object. [29] and [118] also reported a possible QPO at longer period around 1000 d. In our CWT analysis, a high power spectrum feature does appear and it is centered at around 1000 d, spanning almost the full time series. However, this result is only significant before applying the trial correction, and is compatible with noise once the "look-elsewhere effect" is taken into account.

- Mrk 421: [29] reported an oscillating γ-ray emission at $\sim$280 d, compatible with our QPO candidate at 300 ± 64 d (300 ± 65 d) with significance exceeding 5σ in both time binnings. This QPO candidate is also not a persistent one, being seen between MJD 55800 and MJD 57000 approximately (August 2011 to December 2014). In our analysis, both maps show a complex structure, with a possible period change at the end.

- Mrk 501: [28] found a candidate QPO at period $\sim$230 d, compatible with the one we identify at 315 ± 98 d (326 ± 76 d) with a significance $\sim 2.9\sigma$ in the monthly binned light curve, but high significance above 5σ in the weekly binned one. This QPO candidate is also temporary, emerging from MJD 55800 to MJD 57000 approximately, and reappearing between $\sim$MJD 57800 to $\sim$MJD 58700.

We want to remark the following three sources which also present hints of QPOs compatible with some claims in the literature, although only significant before trial corrections.

- PKS 1424-418: [29] and [167] claimed a flux oscillation at period $\sim$353 d and $\sim$355 d respectively in the light curve of this FSRQ. The wavelet analysis, however, shows that this QPO candidate is compatible with noise, with a post-trial significance at $\sim 1\sigma$ for both monthly and weekly binned light curves. On the other hand, we detect a much shorter QPO candidate centered at $\sim 94 \pm 25$ d (90 ± 22 d) in the CWT of the monthly (weekly) binned light curve, at above 5σ significance. This month-long QPO candidate emerged from MJD 56100 to MJD 56500 approximately (June 2012 to August 2013), showing five complete oscillations in the fitted light curve.

- PG 1553+113: The first detection of a periodic behaviour in the γ-emission of this high-synchrotron-peak BL Lac object was claimed by [7], with a period of $\sim$798 d. Some more recent studies found a periodic feature at similar values: [144] reported two peaks at same frequency $\sim 780-810$ d, [52] detected a period of $\sim$790 d, [168] claimed a possible evidence at period $\sim$800 d, and [118] found high significance level at period $\sim$803 d. Our results show that this QPO candidate is significant in pre-trial significance (at a confidence level of $\sim 3\sigma$ ($\sim 2\sigma$) for the monthly (weekly) binned light curve), but becomes less than 1σ after trial correction [consistent with the results by 12].

- PKS 2155-304: We identify a low-significance QPO candidate for this BL Lac object centered at around 334 ± 107 d (341 ± 106 d), with a significance $\sim 2.2\sigma$ ($\sim 3.5\sigma$) in the monthly (weekly) binned light curve. The

QPO candidate clearly shows a time-dependent behaviour, with decreasing frequency in time. This source has been extensively studied in the past and several QPO claims have been made: [173] who detected a possible QPO at period $\sim$640 d, [29] who found two quasi-periodic features, one at 610$\pm$51 d and the other at $\sim$260 d, [52] who found a QPO at $\sim$610 d although not significant enough, [118] who claim a QPO at $\sim$1.7 yr, **(author?)** [153] who found a QPO at 610$\pm$42 d, and [178] who detected a QPO at $\sim$612 d. With respect to the results of our analysis, the QPO found by CWT technique is close to the short QPO candidate presented by [29], whereas the long-term feature at $\sim$600 d, also noticeable in the CWT maps, is not significant after the trial correction, likewise the long $\sim$1000 d QPO candidate in S5 0716+714.

5.6 Discussion

We identify a total of 36 QPO candidates in 24 sources, with the longest one found in the light curve of S5 1044+71 at $\sim$1130 d and the shortest in the light curve of PKS 2247-131 at $\sim$34 d. Many of the candidates have a period between one month and one year. This is a new result since not many month-year-long QPOs have been reported in the literature, and might be revealing that middle-term QPOs are actually frequent in nature. On the other hand, only four candidate QPOs with period of around one month are detected in our results. This can be explained by the fact that this kind of short periods, if not lasting continuously in time, would appear in the CWT map as small structures, being difficult to recognize, and to be disentangled from vertical structures produced by flares. A good example is PKS 2247-131, whose analysis was inspired by the work published by [176]. More example of short-leaving features with periods of the order of one month can be seen in the CWT maps of B2 1520+31, 1H 1013+498, and 3C 279 (see section 5.5.4 and **??**). We remind the reader that our threshold to select candidates is for them to have a post-trial significance $> 3\sigma$ in at least one of the time-bins, and showing more than three cycles. We cannot exclude then, that some of the candidates are spurious, and coming from the analysis itself.

Quasi-periodic modulations observed in the high-energy γ-ray fluxes of AGNs should be related to the relativistic jets launched by these objects or

to the process feeding the jet itself. Two main subgroups of QPOs were often discussed in the literature by considering the oscillation period: short intra-day and year-long QPOs. The former are though to be associated to pulsational accretion flow instabilities [80], despite that longer periods are observed in magneto-hydrodynamical simulations for slow-spinning SMBH [104]. The origin of long-period QPOs, on the other hand, could be related to jet precession, geometry and possibly to the presence of a binary SMBH system [see 7, and references therein]. In simple SMBH systems, jet precession, rotation and helical structure, in the presence of a sufficiently strong magnetic field, yield to observable periodicity from the change of the line of sight. Moreover, these variabilities could also appear in binary SMBH systems due to periodic perturbation of the secondary compact object to the accretion disk and jet. The orbital period of the binary systems is in the range of several years, being compatible with the year-long period QPOs. The most significant, multi-year, QPO candidate in our analysis, seen at more than 4σ in the blazar S5 1044+71, has a period of about 1100 d (3.5 y), and thus makes this γ-ray source a high-significance SMBH binary candidate in the Universe.

No QPOs at an intermediate time scale were reported until the publication of [176], who claimed the detection of $\sim$34.5 d QPO in the light curve of PKS 2247-131. This monthly modulation suggested a helical jet structure due to the short period. However, they also noted that the helical structure could be driven by the orbital period of a secondary SMBH. By considering the time compression due to the high Doppler factor of the emitting region, the observed period will be shortened with respect to the physical period in the host galaxy reference frame, and can still be of the order of orbital periods for close binary SMBHs. In our analysis of PKS 2247-131, an additional QPO ($\sim$200 d) seems to be existing in the form of large γ-ray flares during the last few years, and could be used to provide further constraints on the model.

We highlight here three important findings that emerged from our analysis that might be used as key observables to understand the origin of QPOs in blazar γ-ray light curves:

- We do not detect persistent QPOs, that last for the whole observing period. None of the global wavelet power spectra show significant features after trial correction. S5 1044+71 might be considered a persistent QPO candidate if we make the hypothesis that the first maximum is

suppressed due to additional modulation. Despite this potential exception, all other QPO candidates in our analysis are transient ones.

- We identify some cases where the QPO candidate shows period shifts. This can be seen in the CWT maps of B2 1520+31 and, at lower significance, of PKS 2155-304, where one of the QPO candidates is decreasing its frequency. Hunting for a possible explanation, we might consider changes in the inclination angle of jet precession. But the reasonable timescales involved should not produce a transition as fast as the observed one. A much easier possibility is that we are observing the helical geometry of a jet with an intrinsic opening angle, that naturally leads to a slowdown of the QPO.

- Lastly, we see several occurrences of multiple QPO candidates occurring simultaneously, and with harmonic periods. One of the examples is 4C+01.02, where two QPOs with different frequencies overlap in a specified time interval. The longer period is approximately two times the shorter one, suggesting the presence of resonances in the emission. Simultaneous QPO candidates at harmonic ratios (within errors) can be seen in PKS 0402-362, 1H 1013+498, B2 1520+31, and CTA 102. Harmonics are common in QPO analysis of X-ray binaries [83], so it is not surprising to see them also in AGNs. They indicate that the various QPOs share the same origin and are not due to independent physical processes, each one imprinting its particular QPO on the light curve. Theoretical models aimed at explaining QPOs in γ-ray light curves of blazars can thus be further constrained by studying harmonics, and harmonic ratios.

Furthermore, no QPO candidates are identified in the γ-ray emission of 3C 66A, PKS 0235+164, 4C +55.17, B3 1343+451, PKS 1424+240, PKS 1502+106, PG 1553+113, 4C +38.41, 1ES 1959+650, BL Lac and PKS 2326-502. Three of them, PG 1553+113, BL Lac and 3C 454.3, were previously reported showing periodic oscillation.

- PG 1553+113: We discussed in the previous section that the wavelet analysis do show a increase in power spectrum at a period similar to

the one reported by [7, 144, 52, 168, 118] ($\sim$800 d), but with a very low post-trial significance not reaching 1σ. In order to check the consistency of our result with the literature, we made a test with a reduced light-curve (removing the last cycle). The result shows that although the significance rises a bit, it still remains below 3σ post-trial. The major effect must come from the trial correction, which indeed, is not done when analyzing a single source. And furthermore, when increasing the duration of the light curve, the number of trials also increases. Before trial correction, we find a significance not much different compared to other works in the literature.

- BL Lac: [145, 144] identified a candidate QPO with period of $\sim$680 d in BL Lac's light curve. Nevertheless, our results show that this possible QPO is compatible with red noise, as was also found by **(author?)** [51, 118].

- 3C 454.3: [146] claimed a $> 4\sigma$ QPO at period $\sim$47 d analysing the 1-day binned light curve of 3C 454.3, lasting from MJD 56800 to MJD 57250. We can observe in our CWT maps of this source that there is a strong vertical signal before MJD 56000 and no further significant feature appears afterwards. Thus, our CWT maps of 3C 454.3 show no evidence of such a QPO even for the 7-days binned light curve.

Finally, some other γ-ray AGN have been claimed to show QPOs with periods of the order of years, but were not included in our sample only because they did not pass our original cut on brightness. For completeness, we mention here the cases of PKS 0301-243 [174], with a period of 2.1 ± 0.3 yr, PKS 0521-36 [172], with a period of about 1.1 yr, PKS 0601-70 [175], with a period of 1.22 ± 0.06 yr, and OJ 287 with a period of about 314 d [91].

We further remind the reader that our work is limited by two main choices: the target list, and the time binning. Extending the target list towards less bright objects is certainly possible, although with a major price: at some point the *Fermi*-LAT light curves of these fainter AGNs will start to show non-detections in individual bins, and the presence of these zeros is problematic for the CWT technique that is sensitive to discontinuities. A simple

solution will then be to also investigate longer time bins. Finer time bins could also be investigated for very bright γ-ray flares, giving access to QPO searches on time-scales of days. Both options have a price, that is an increase in the number of trials. As a final caveat, our results and in particular the determination of the significances depend on the Monte-Carlo simulations of artificial light curves. In our study we work under the assumption that the PSDs of the original light curves can be reconstructed by fitting them with a smoothly bended powerlaw function but this choice is far from unique. For a comprehensive study of Fermi-LAT PSD using different methods, see the recent work by **(author?)** [153].

5.7 Conclusions

The search for QPOs in the light curves of AGNs is a major research topic in astrophysics, providing us additional constraints on the physics of the SMBHs that power these sytems. Long-term QPOs, with periods of the order of months and beyond, are particularly difficult to identify due to the need of highly-sampled and unbiased light curves over long periods of time. The *Fermi*-LAT γ-ray telescope, thanks to its monitoring capabilities is an ideal instrument to perform such a study.

We analysed 13-years long (from August 2008 to April 2021) *Fermi*-LAT γ-ray light curve in two different time binnings (7 and 30 days) of 35 bright γ-ray AGNs. By using the CWT technique, we systematically searched for QPO candidates in this data set. In order to compute the confidence levels of the QPO candidates, 10000 simulated artificial light curves are generated for each light curve, and the histograms of global power spectrum at each period scale are fitted to a χ^2 function. We correct for the trial effect in our analysis by estimating the trial number due to the number of sources and the number of time-period bins (in the wavelet power spectrum) or the number of period bins (in the global wavelet spectrum), outside the COI, and following the parameterization given by [23].

In this way, 36 QPO candidates in 24 sources are identified (at various significance levels) with periods ranging from one month to several years. Our most significant, multi-year QPO candidate is in the blazar S5 1044+71, with

a period of about 1100 d.

We confirm some previously claimed γ-ray candidate QPOs in the sources PKS 0537-441, B2 1520+31, PKS 2247-131, S5 0716+714, Mrk 421, Mrk 501 and PKS 2155-304, while new possible QPO candidates are identified in 4C +01.02, 4C +28.07, NGC 1275, PKS 0402-362, PKS 0426-380, PKS 0447-439, PKS 0454-234, 1H 1013+498, S5 1044+71, 4C +21.35, 3C 273, 3C 279, PKS 1424-418, PKS 1510-089, B2 1520+31, CTA 102, PKS 2247-131, 3C 454.3 and PMN J2345-1555.

Possible physical origins of these quasi-periodical emissions are the precession of the AGN jet, its helical structure, and changes in the accretion flow. These scenarios can be due to the presence of a second SMBH in the system, opening up the window to study SMBH binaries. Since the orbital periods of the SMBH binaries are of the order of several years, sources showing long-term QPOs are naturally suspected as binary candidates. In particular, we put forward the blazar S5 1044+71 as the most promising SMBH candidate in our sample, due to its high significance QPO candidate with a period of about 1100 d. Shorter, month-long QPOs, could also be related to close SMBH binaries, once the period is corrected for the Doppler factor of the jet. In our analysis we identify a peculiar behaviour in some QPO candidates, that might hint towards a QPO origin related to the jet geometry, that is a varying (slowing-down) QPO frequency, seen in B2 1520+31. We also put forward the possibility that some simultaneous QPO candidates, such as the ones seen in 4C +01.02, are indeed harmonics, with a single physical mechanism at the origin of them.

With this, we can conclude that the CWT technique is a very powerful tool sensitive to any periodic oscillations in the light curves, considering an appropriate time binning. It has the major advantage over other statistical tools to be sensitive to transient QPO and period-shifting QPOs. However, it also reacts strongly to flares, resulting in vertical features in the map, and is influenced notably by border effects at large periods. This leads to the requirement of a visual inspection of all CWT maps to avoid misleading results. A major point to be highlighted is the trial-correction of significances. Due to the large number of scales probed, the number of sources, and the number of time binnings investigated, the number of trials is pretty large, and a careful correction has to be implemented to avoid false positives. While this correc-

tion is clearly mandatory for systematic studies as ours, it is necessary also for studies that analyze a single source without justifying how a particular target has been selected among the *Fermi*-LAT catalog.

A natural perspective for a future study would be a multi-wavelength analysis of quasi-periodic emissions from the selected interesting γ-ray sources. First, the identification of QPOs at multiple wave bands with the same periodicity will automatically boost the significance of the detection, or, if the QPO is only seen in γ-rays, help identify false positives. Second, and more importantly, multi-wavelength observations will constrain the theoretical models that aim to explain these QPOs. Long-term, unbiased, multi-wavelength monitoring campaigns over several years, as complex and expensive as they might seem, are thus the key to identify AGN QPOs and understand their origin.

6 Gradient boosting decision trees classification of blazars of uncertain type in the fourth Fermi-LAT catalog

6.1 Introduction

Fermi Gamma Ray Space Telescope (Fermi) launched in 2008 with improved sensitivity, wide field of view, large energy range, and an all-sky-survey operation mode, provided an unprecedented detailed view of the γ-ray sky. The primary instrument onboard the spacecraft, the Large Area Telescope (LAT), performs all sky survey every three hours in the energy range from $\sim$ 100 MeV to $>$ 300 GeV providing continuous and deepest view of the γ-ray sky. Further details on Fermi-LAT are given in **(author?)** [22].

The Fermi-LAT observations resulted in detection of many galactic and extragalactic γ-ray sources. For example, the most recent fourth Fermi-LAT catalog of γ-ray sources [4FGL Data Release 3 (DR 3) 6] based on the data accumulated between 2008-2020 (12 years) contains 6659 Galactic and extragalactic source of different classes. Pulsars are the largest class of Galactic γ-ray emitters - 292, and other Galactic γ-ray emitters are: globular clusters-25, Supernova remnants - 43 and Pulsar wind nebulae - 19. The extragalactic γ-ray sky is largely dominated by active galactic nuclei, in particular by blazars which also represent the largest fraction of the sources in 4FGL, 3743 out of 6659.

Blazars are a rare type of AGNs when one of the jets makes a small angle ($< 10^{\circ}$) to the line of sight of the observer [160]. The nonthermal emission from blazars is characterized by rapid flux variability across the entire accessible electromagnetic spectrum, the most extreme being at γ-rays. Blazars are sub-grouped in two large classes, Flat Spectrum Radio Quasars (FSRQs)

and BL Lacertae objects (BL Lacs), based on the properties observed in the optical spectrum, namely, in FSRQs strong and quasar-like emission lines are observed, whereas in BL Lacs the emission lines are weak or absent [160]. Blazars are further classified using the observed frequency of the synchrotron peak ($\nu_{s,p}$) as either low synchrotron peaked sources (LSPs or LBLs) when $\nu_{s,p} < 10^{14}$ Hz, intermediate synchrotron peaked sources (ISPs or IBLs) when 10^{14} Hz $< \nu_{s,p} < 10^{15}$ Hz and high synchrotron peaked sources (HSPs or HBLs) when $\nu_{s,p} > 10^{15}$ Hz. In this classification FSRQs have $\nu_{s,p}$ similar to those of LBLs. Among the blazars included in 4FGL, 1456 are BL Lacs, 794 are FSRQs and 1493 are blazar candidates of uncertain type (BCU). BCUs display properties similar to blazars (e.g., a flat radio spectrum and a typical two-humped blazar-like spectral energy distribution), but reliable optical association is lacking.

BCUs corresponds to the 39.9% of all blazars included in the 4FGL and their possible classification is very important for the scientific community, as it can be useful for blazar population studies (i.e., properties of different blazar sub-classes) or for planning observational campaigns on individual objects. Moreover, possible classification of BCUs is also important, considering the recent possible association of blazars and IceCube events that triggered interest on possible multi-messenger observations of blazars [e.g., 81, 82**?** , 138]. Although various optical monitorings aim to classify BCUs, they are time consuming and costly, given the large number of BCUs. However, in recent years there is a growing interest in applying machine learning techniques to different fields of science, including astronomy and astrophysics. Machine learning is a powerful tool in data science allowing machines to learn from data, detect patterns, self-improve and make classifications. The distinct spectral properties of BL Lacs and FSRQs in the γ-ray band can be used to train models which then can classify BCUs by comparing their properties with those of BL Lacs and FSRQs.

In fact, machine learning was already applied by **(author?)** [8, 46, 147, 142, 92, 89, 21, 90, 166, 58, 66, 47, 177, 60, 110, 27, 38, 27, 49] and other authors to study the multiwavelength properties of blazars, or classify unassociated γ-ray sources, or classify BL Lacs and FSRQs among BCUs. The methods used to identify or classify blazars include Artificial Neural Network (ANN) [e.g., 46, 142, 89, 90], multivariate classifiers - boosted decision trees and multilayer perceptron neural network [92], Bayesian Neural Networks [38], Random Forest [e.g., 147], CatBoost gradient boosting decision trees [49], and

others. All the applied models with different performances produce satisfactory results in classifying blazars based on different properties. It should be noted that machine learning techniques are also used to estimate different properties of blazars. For example, in **(author?)** [46] ANN was used to identify high synchrotron peaked blazars or **(author?)** [75] developed BlaST which uses machine learning methods to estimate the synchrotron peak directly from the blazar spectral energy distribution.

The goal of the current work is to perform a machine learning classification of BCUs by training the models on the most up-to-date γ-ray dataset which contains spectral and temporal properties of BL Lacs and FSRQs. Using the most complete γ-ray dataset based on 12 years of Fermi-LAT operation (4FGL) as well as state-of-the-art classification methods (eXtreme Gradient Boost [44] and *LightGBM* [85]) will better identify common patterns in γ-ray properties of BL Lacs and FSRQs and will allow statistically better association of BCUs.

The structure of the paper is as follows. In Section 6.2, the source sample and the properties of the used data are presented. The various algorithms used in the current paper are discussed in Section 6.3. In Section 6.4, we provide an overview of the obtained results and provide the conclusions in Section 6.5.

6.2 The source sample from 4FGL-DR3

The incremental version of the fourth Fermi-LAT catalog (4FGL Data Release 3 [DR3]) contains 6659 sources and for each individual source together with the coordinates, various spectral properties are provided, such as flux, detection significance, spectral parameters when fitting with different models, etc. For our study, from 4FGL DR3 we selected all sources with BLL, FSRQ and bll, fsrq designations where in capital letters are firm identifications whereas lower case letters indicate associations [see 6]. This amounted to 2250 sources (1456 BL Lacs and 794 FSRQs) to train our models. Then those models are applied to classify 1493 blazar candidates.

Among the features and measurements presented in 4FGL, we are interested in the energy spectra and fluxes measured in different periods; the first correspond to the sources' fluxes measured in different energy bands (*nuFnu_band* column) while the second one represent the sources' flux as a function of time (*Flux_History* column). These two measurements well char-

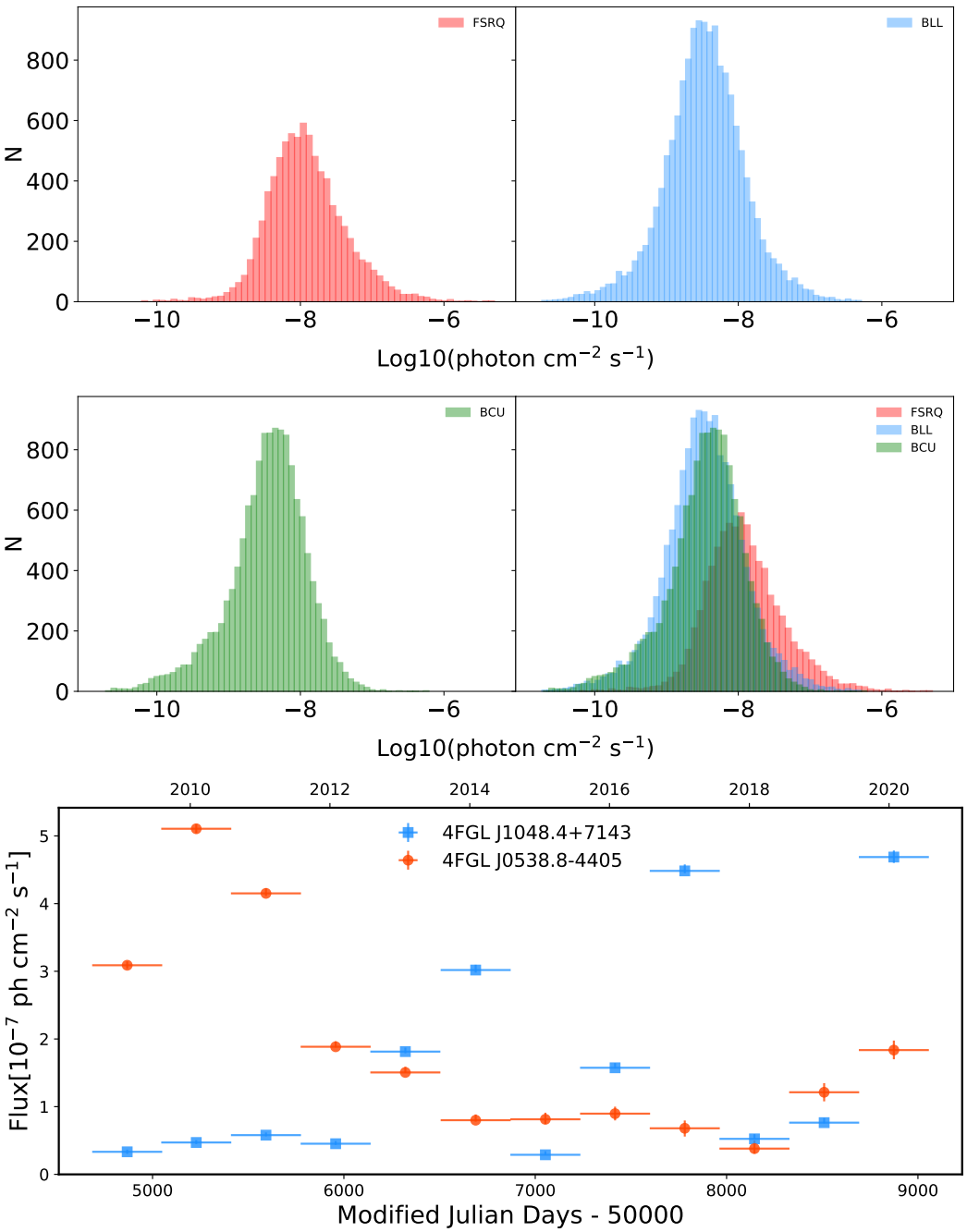

Figure 6.1: *Upper and middle panels:* The distribution of yearly fluxes of FSRQs, BL Lacs and BCUs included in the 4FGL catalog. *Lower panel:* The light curves of 4FGL J0538.8-4405 (BL Lac) and 4FGL J1048.4+7143 (FSRQ) measured during 12 years (2008-2020).

acterize different blazar sub-classes and are used as input parameters for our models.

6.2.1 γ-ray light curves

4FGL contains information on the γ-ray flux of the considered sources in different time bins (light curve) which is an essential information on the blazars emission features observed in the initial 12 years of Fermi-LAT operation. These light curves were computed by dividing the whole time period into twelve intervals (one year each) and the fluxes in each sub-interval were estimated by applying binned (up to 10 GeV) and unbinned (10-100 GeV) likelihood analysis. These fluxes were estimated by freezing the spectral parameters to those obtained in the fit over the full range and by adjusting the normalization. The photon fluxes estimated in the energy range 0.1-100 GeV in the units of $photon\, cm^{-2}\, s^{-1}$ are reported for each year.

For each selected source this creates twelve parameters that describe the γ-ray flux evolution in different periods. One may speculate that the short time flux variability will be smoothed out when measuring the flux in one-year intervals. However, the goal is to identify common patterns in the change of the γ-ray flux of blazars in different sub-classes rather than to compare the variability timescales. Moreover, by comparing the variability of blazars using 2-month and 1 year light curves, **(author?)** [5] showed that among 1173 sources identified as variable in 2-month intervals, 1057 show variability also in yearly binned intervals. Therefore, the one-year-binned light curves contain most of the variability information on the considered sources. Also, when the flux is measured in shorter periods, it might result in many upper limits which creates additional uncertainties for the models.

The distribution of the yearly measured fluxes of BL Lacs, FSRQs and BCUs is shown in Fig 6.1 (upper and middle panels), highlighting the difference in their γ-ray emission. For example, the mean of FSRQ γ-ray fluxes distribution is at $3.28 \times 10^{-8}\ photon\, cm^{-2}\, s^{-1}$ while that of BL Lacs is at $8.19 \times 10^{-9}\ photon\, cm^{-2}\, s^{-1}$. FSRQs are brighter with a highest yearly flux of $5.05 \times 10^{-6}\ photon\, cm^{-2}\, s^{-1}$ observed for 4FGL J2253.9+1609 (3C 454.3) as compared with the similar value of $5.2 \times 10^{-7}\ photon\, cm^{-2}\, s^{-1}$ observed for BL Lacs, 4FGL J2202.7+4216 (BL Lacertae). The BCU yearly fluxes distribution with a mean of $6.72 \times 10^{-9}\ photon\, cm^{-2}\, s^{-1}$ is broader, mimicking the properties of both FSRQs and BL Lacs. The distribution of yearly fluxes of FSRQs, BL Lacs

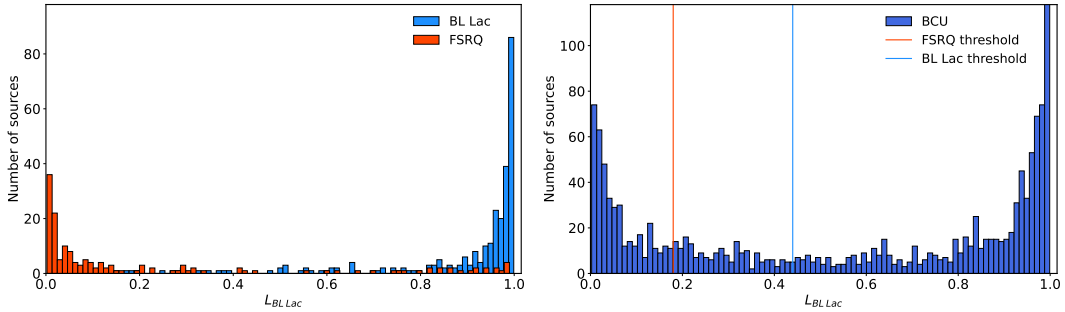

Figure 6.2: *Left panel:* Distribution of the likelihood to be BL Lac (blue) or FSRQ (orange) for the sources in the test sample. *Right panel:* Distribution of the likelihood of 1420 BCUs to be BL Lac or FSRQ candidates.

and BCUs are shown together in Fig. 6.1 middle panel right side.

The fluxes estimated in each interval represent an independent state of the sources and show their brightest and lowest emission states. The light curves of the sources (FSRQ and BL Lac) shown in Fig. 6.1 (lower panel) clearly demonstrate their different emission states. For example, BL Lac 4FGL J0538.8-4405 (orange circles in Fig. 6.1 lower panel) is initially in the high γ-ray emission state while it is in a relatively faint state in 2014, but then brightens again at the end of the considered period. Instead, the emission from FSRQ 4FGL J1048.4+7143 (blue squares in Fig. 6.1 lower panel) is initially in a relatively faint state but then it is in repeatedly flaring and quiescent states. Therefore, given that blazar emission is variable, a simple comparison of the fluxes of different sources estimated in the same year does not have any physical motivation. On the other hand, the change in the flux is linked with the source properties and it is meaningful to compare the fluxes when the sources are in the lowest, average or brightest emission states. Thus, we have sorted the early measured fluxes from the lowest to the highest and they are considered as twelve different input parameters. So, the network can compare and contrast the fluxes of sources whether they are in low or bright emission states. Some sources do not have the flux measured for all yearly bins, only the upper limits are given, so these data are missing. For the periods with no detection (upper limit) zero or NaN were set, depending on the method, meaning that there is no information.

6.2.2 γ-ray spectra

It is known that the γ-ray spectra of BL Lacs and FSRQs shown distinct differences. For example, **(author?)** [5] have shown that 93% of FSRQs have power-law photon indices > 2.2 while those of 81% of BL Lacs < 2.2. However, the photon index of BL Lacs varies also for LBLs, IBLs and HBLs; the γ-ray spectra of LBLs are softer than those of HBLs [see e.g., 14]. In principle, the difference between FSRQs and BL Lacs can be of a purely physical origin. In BL Lacs jets the electrons can be accelerated to higher energies, having a harder energy spectrum and hence producing photons with harder spectra. Instead, in FSRQs where the electrons effectively interact with different photon fields and efficiently cool down, the produced photons will appear with a soft γ-ray spectrum. Therefore, the spectral difference between FSRQs and BL Lacs can be used for BCU classification.

The 4FGL catalogue provides the sources fluxes (spectra) measured in eight energy bands: *1)* 50–100 MeV, *2)* 100–300 MeV, *3)* 300 MeV–1 GeV, *4)* 1–3 GeV, *5)* 3–10 GeV, *6)* 10–30 GeV, *7)* 30–100 GeV and *8)* 100 GeV–1 TeV. We excluded the first band, as at lower energies the fluxes could be affected by contamination of other sources. Visually inspecting plots of spectral fits of all sources, we decided to drop the last band as well because it is an upper limit for many sources, and work with the remaining 6 bands. The fluxes in each of these bands contain information of average spectra of the sources (e.g., spectral index, spectral curvature, spectral breaks, etc.) and can be used to distinguish between different types of blazars. The fluxes measured in each energy band were not sorted and provided as input according to the increase of the energy because they are defined by the photon index which is different for FSRQs and BL Lacs. There is already a physical interpretation for the fluxes in the same input parameter, so their compression is meaningful.

6.3 Model construction

The aim of this work is to examine the nature of BCUs in 4FGL based on their γ-ray properties. The spectral and temporal properties discussed in the previous section provide a framework for predicting the expected types of unclassified blazars. This is done by defining models that find correlations between measured γ-ray properties of BL Lacs and FSRQs and then compare them to the γ-ray properties of BCUs. Here, we have implemented two differ-

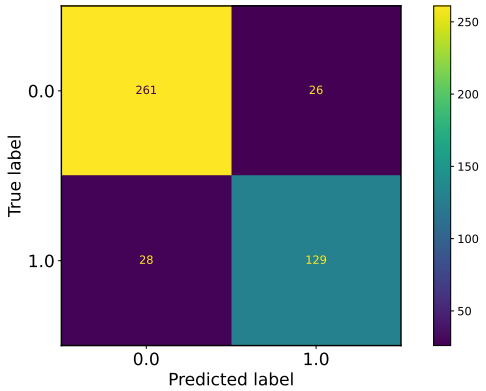

Figure 6.3: The confusion matrix of *LightGBM_opt* classifier on the test sample.

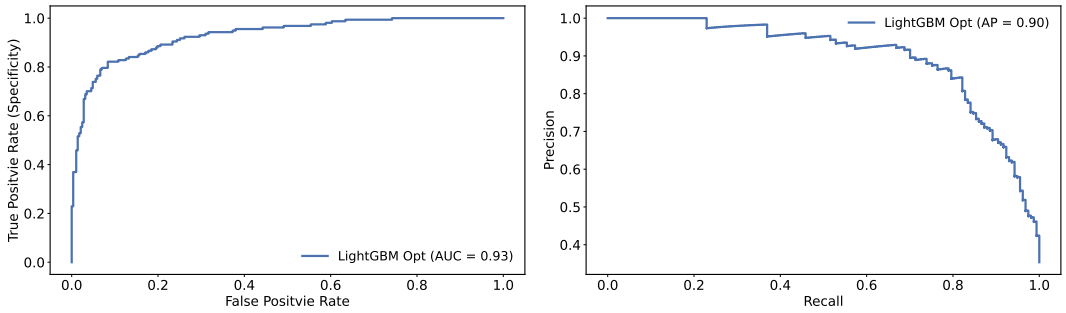

Figure 6.4: *Left panel:* ROC curve for *LightGBM_opt* classifier. *Right panel:* Precision Recall curve.

ent machine learning techniques to classify BCUs: Artificial Neural Network (ANN) and Gradient Boosted Decision Tree algorithm. Below we briefly introduce the general features of the used techniques.

- *Artificial Neural Network*

  Artificial Neural Networks (ANNs) [30] are among the most powerful tools in pattern-recognition problems. ANNs have been used successfully in various fields, including astrophysics and cosmology [e.g., 24, 55, 79, 142, 46, 89, 90].

  ANN consists of input, hidden, and output layers with connected neurons (nodes) representing a simplified model of the human brain functioning and the nervous system. A standard neural network contains

Table 6.1: The BCU classification performance of the models.

Model	Recall of Minority	Recall Weighted	Precision Weighted	ROC-AUC Mac
ANN	0.81	0.88	0.88	0.86
XGBoost_def	0.77	0.87	0.87	0.85
XGBoost_opt	0.80	0.87	0.87	0.86
LightGBM_def	0.81	0.87	0.87	0.86
LightGBM_opt	0.82	0.88	0.88	0.87

an input layer and an output layer but in most cases it can include any number of hidden layers with any number of hidden nodes in each layer. The input parameters, neurons in the input layer, are connected to one or more neurons in the hidden layer (intermediate layer) and propagate the data to the deeper layers and send the final output data to the last output layer (prediction). Each neuron in the first hidden layer is assigned weights associated to input parameters which indicates the importance of each neuron in the network. The goal of ANN training is to minimize the output error by finding the best set of weights for each connection. Initially, the weights are assigned randomly and are optimized during an ANN training. So, the ANN uses the input data to produce an output data which is compared with the real data to calculate the error (loss function). Then, ANN learns by adjusting its weights such that in the next iteration the net error produced by the ANN is generally smaller than that in the current iteration. So, it optimizes the weight values to get the best result from the network.

In our case, when the classification is the goal, the input parameters (fluxes in different years and fluxes in each energy bin) are values describing blazars while output layer is the number of classes (FSRQ or BL Lac). The network is trained (i.e., to find a function which best separates objects belonging to different classes) on already classified BL Lacs and FSRQs, tested on a selected sample of classified sources that was not used in the training, and then the resultant model can be used to classify BCUs.

- *Gradient Boosted Decision Tree*

Gradient Boosted Decision Tree (GBDT) is a machine learning algorithm used for both classification and regression problems. Boosting is one technique which aims to build a strong classifier from a number of weak classifiers, so it is forward-learning ensemble method that obtains results by gradually improving the estimations. Initially, a model (e.g., a tree) is fitted to the data, and then a second model is constructed by improving the cases where the accuracy of the first model was not good. Then, these processes of boosting are repeated many times to create a series of decision trees that produce an ensemble of weak prediction models; each successive model attempts to correct for the weakness of all the previous models and the combination of new models is better than the previous ones alone. In the gradient boosting method the loss function is minimized by adding trees in a gradient descent procedure. Namely, the very first model is trained on the dataset, whereas the second model is trained on the errors of the first model and added to the first model and so on. GBDT algorithms have wide applications and been used also in astronomy and astrophysics in a variety of problems [e.g., 49, 76, 84, 169].

Here we use *XGBoost* and *LightGBM* methods based on gradient boosting algorithm to classify BCUs. Extreme Gradient Boosting (XGBoost) [44] is a scalable machine learning algorithm for tree boosting where the best model is found by applying more accurate approximations. Unlike GBDT, in *XGBoost* model the objective function is optimized using Newton-Raphson method, i.e., second-order partial derivatives are used to gather more information about the direction of the gradient and the way to get to the minimum of the loss function. *LightGBM* is another implementation of GBDT [85]. *LightGBM* uses portion of the data with low memory cost applying two novel approaches for sampling: Gradient-based One-Side Sampling and Exclusive Feature Bundling. In contrast to *XGBoost* where the trees are growth level-wise (horizontal), in *LightGBM*, the decision trees are grown vertically, which can reduce more loss and provide a more accurate result. The goal of both algorithms, *XGBoost* and *LightGBM*, is the non-linear mapping from a set of input parameters to an outcome, namely, a prediction whose possible numerical values are spanned by the set of leaves. As an output, it provides a probability whether the source belongs to BL Lac or FSRQ sub-classes.

Both methods apply conceptually different approaches in transferring the input data into output models. The complex methods based on neural networks (like ANN) pose many challenges when applied to tabular data which contains sparsity (missing values, e.g., yearly fluxes in our case). The simple filling in of missing values with 0 or other constant might result in finding biased patterns in the data training or might significantly affect the obtained results. Instead, generally, the methods based on GBDT (like *XGBoost* and *LightGBM*) dominate when used on tabular data, showing superior performance. These algorithms can be trained on the data with missing values without doing imputation first and the tree branch directions for missing values are learned during training, each time deciding the best way to handle them. In addition, the algorithms based on decision trees are more applicable on the comparably small data sets (as in our case), as the complex methods based on neural networks tend to overfit the models. Thus, state-of-the-art algorithms, *XGBoost* and *LightGBM*, are more powerful and preferable tools for the classification of blazars. However, for a comparison we also performed classification using ANNs.

6.3.1 Training and testing

The data presented in previous section are used to train models and predict BCUs. Among the considered sources we dropped those which have three or more energy intervals with upper limits; in total 104 sources were dropped (73 BCUs and 31 FSRQs and BL Lacs). The entire dataset consists of 2219 rows from which 80% was selected as training set while 20% was the test set. We have used a 15-fold cross-validation procedure to evaluate the performance of the algorithms. In this procedure, the dataset is divided into 15 non-overlapping folds and the fitting is performed using 14 folds. Then, the model is validated using the remaining 15th fold. This procedure is repeated until every 15 folds serve as a validation and the average is taken as performance of the network. In this way, each of the 15 folds is given an opportunity to be used as a held-back validation set.

In our dataset each blazar (whether FSRQ or BL Lac) is characterized by 18 parameters: 12 yearly sorted γ-ray fluxes and 6 fluxes in each band. The BL Lacs and FSRQs with evident differences (see Section 6.2 and Fig. 6.1) occupy a different region in this parameter space and the goal is to quantify and determine the differences. In the ANN, the input neurons are 18, equal

to the number of the input parameters, and we used three hidden layers with 64, 128 and 64 neurons. To prevent overfitting, we added two dropout layers, between hidden layers, to randomly set units to 0 with a frequency of 0.4 and 0.5. The number of neurons in hidden layers was selected by reducing the number of neurons but keeping the performance accuracy. The *XGBoost* and *LightGBM* classifiers contain a set of important hyperparameters, among which the most important are the number of leaf nodes, the learning rate, and the number of iterations. Different values of these hyperparameters may increase the model performance, so their best values were found by hyperparameter tuning, i.e., the best version of the models are found by running many jobs that test a range of hyperparameters on the training and validation datasets. We used HyperOpt package [1] which uses a form of Bayesian optimization for parameter tuning. We found the following optimal parameters for *LightGBM* model: the number of leaf nodes-31, learning rate-0.3, and number of iterations - 400, etc. However, in order to compare the resultant models, initially the model fitting was performed with the default parameters (*XGBoost_def* and *LightGBM_def*) and then with the optimized parameters (*XGBoost_opt* and *LightGBM_opt*). In all the trained models, the output was set up to have two possibilities, i.e., it returns the likelihood of a source to belong to either FSRQs (L_{FSRQ}) or BL Lacs ($L_{BL\,Lac}$). The likelihood is assigned such that $L_{BL\,Lac} = 1 - L_{FSRQ}$; the larger $L_{BL\,Lac}$ (closer to 1) the higher the likelihood that the source is a BL Lac and vice-versa.

6.4 Results and Discussions

In this section, we discuss the results of classification of BCUs from 4FGL. Table 6.1 provides summary results of applied models, showing their performance. To fully evaluate the effectiveness of the models, we compare the precision and recall. The precision measures the model's accuracy in classifying a sample as positive, i.e., the ability not to misclassify a BL Lac (FSRQ) as a FSRQ (BL Lac). Meanwhile, recall measures the model's ability to detect positive samples, i.e., the ability to identify all BL Lac (FSRQ) samples. Considering our dataset is slightly imbalanced, i.e., there are a disproportionate ratio of BL Lac and FSRQ classes (65:35), minority class (FSRQs in our case) has the highest interest from a learning point of view, as it can be

[1] https://github.com/hyperopt/hyperopt

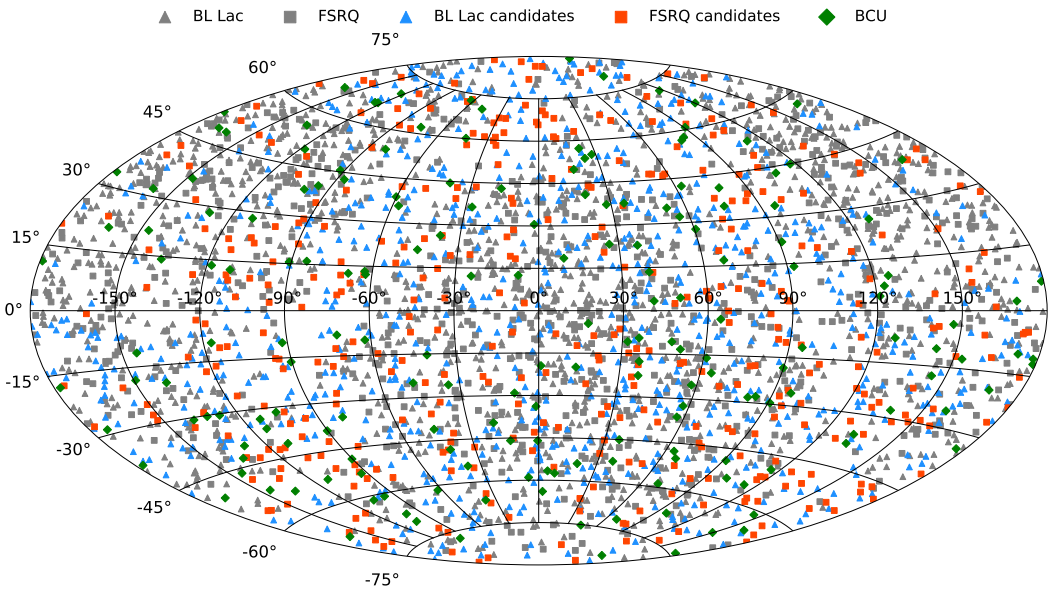

Figure 6.5: Hammer-Aitoff projection of FSRQs, BL Lacs and BCUs. The location of BL Lacs and FSRQs from 4FGL is shown with gray color while the new BL Lac and FSRQ candidates are in blue and orange, respectively.

under-classified. Therefore, we compare the models performance considering the recall of minority class (first column in Table 6.1) which shows that the *LightGBM_opt* model has the highest value for minority recall, 0.82, and a satisfactory precision, 0.88. Therefore, it provides the best BCU classification performance, so we report only the results obtained by this model.

In order to demonstrate the ability of *LightGBM_opt* to distinguish BL Lacs and FSRQs, the likelihood distribution of test sample is shown in Fig. 6.2, left panel. The test sample contains 287 BL Lacs and 157 FSRQs, the ratio of which 287/157$\simeq$1.83 is the same as in the total sample (1436/783$\simeq$1.83). In the distribution, there are two evident and opposite peaks, BL Lacs (blue) centralized towards $L_{BL\,Lac} = 1$ while opposite for FSRQs $L_{BL\,Lac} = 0$, which clearly shows the ability of our model to separate BL Lacs and FSRQs from the test sample (not used during the training).

The performance of our applied model can be further examined from the confusion matrix shown in Fig. 6.3 which summarizes the number of true and predicted classes. The comparison of the number of correct (129-FSRQs and 261-BL Lacs) and incorrect (28-FSRQs and 26-BL Lacs) predictions shows that the model classifies BL Lacs and FSRQs perfectly. Other ways to analyze the effectiveness of the model are Receiver Operating Characteristic (ROC) and Precision-Recall curves shown in Fig. 6.4. The ROC curve (left panel in Fig. 6.4) represents the graph of the true positive rate versus the false positive ones and shows the performance of the model at all classification thresholds. The Area under the ROC Curve (AUC) is a measure of the model usefulness-the higher the AUC the better the model can distinguish between BL Lacs and FSRQs; in this case AUC=0.93. The Precision-Recall curve in Fig. 6.4 (right panel), the plot of the precision against the recall at a variety of thresholds, shows the trendoff between the precision and recall.

The accuracy of the network defined as positive association rate, i.e., how many BL Lacs (FSRQs) are correctly identified out of all BCUs, was optimized by selecting different classification thresholds for BL Lacs and FSRQs. The accuracy reaches 0.9 (90 %) when the classification threshold of $L_{BL\,Lac} > 0.44$ identifies BL Lac candidates, while threshold $L_{FSRQs} > 0.82$ identifies FSRQ candidates.

We applied the best model to the entire 1420 BCU sample in 4FGL. It is found that 825 objects (58.1%) have likelihood above the threshold of $L_{BL\,Lac} = 0.44$ and are classified as BL Lacs, 405 (28.5%) are FSRQs having likelihood above $L_{FSRQ} = 0.82$, and 190 (13.3%) remain unclassified. The sky distribution of blazars locations in Galactic coordinates and Hammer–Aitoff projec-

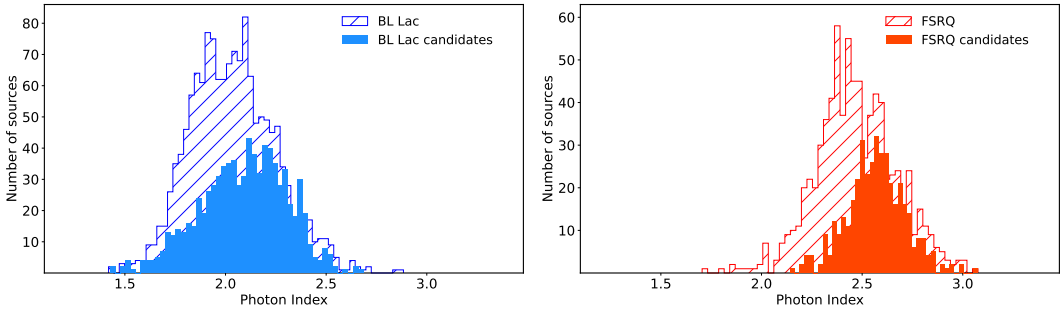

Figure 6.6: The power-law photon index distribution of BL Lacs (left) and FSRQs (right) in 4FGL. The distributions are compared with newly classified BL Lac and FSRQ candidates (filled histograms).

tion is shown in Fig. 6.5. The location of BL Lacs and FSRQs from 4FGL are shown with gray triangles and squares, respectively, most likely BL Lacs and FSRQs from BCUs are in blue triangles and orange squares, respectively, and the remaining unclassified BCUs are in green diamonds.

The likelihood distribution of the model applied to BCU sample is shown on the right panel of Fig. 6.2. As expected, it mimics the same trend as seen for BL Lacs and FSRQs in test sample (left panel of Fig. 6.2). The ratio of BL Lacs to FSRQs identified from BCUs is 2.03, similar to the result obtained in **(author?)** [90] which classified BCUs in Fermi-LAT 8-year source catalogue using ANNs. Table 6.2 shows the portion of the sources having higher probability of being BL Lacs and FSRQs; for each source the name in the catalogue, RA and Dec, detection significance (σ), energy flux and its uncertainty, and the probabilities to be BL Lac or FSRQ are reported. As it can be seen from the table, the used algorithm can classify BCUs as BL Lacs or FSRQs with a high probability. However, there are also sources with intermediate likelihoods falling in the region where the two sub-classes overlap, so they cannot be classified by the model. The full BCUs classification table that includes also the sources which have lower association likelihood is available in the online supplementary material and at the following github repository `https://github.com/mherkhachatryan/BCU-Classification.git`.

The comparison of BL Lac and FSRQ candidate list presented here with the previous studies is not straightforward and rather difficult as the number of blazars and their classifications are changing in different versions of the catalogues. However, to show the accuracy of our method, we present a general

Table 6.2: List of BCUs from 4FGL with the most significant association.

Source Name	RA	Dec	Significance	Energy Flux	$L_{BL\,Lac}$	L_{FSRQ}
4FGL J1925.0+2815	291.2683	28.2643	17.84	$(6.8 \pm 0.61) \times 10^{-12}$	0.9989	0.0011
4FGL J1958.1+2438	299.5284	24.6417	11.24	$(6.6 \pm 0.94) \times 10^{-12}$	0.9986	0.0014
4FGL J0121.7+5153	20.4389	51.8947	5.90	$(1.5 \pm 0.37) \times 10^{-12}$	0.9983	0.0017
4FGL J0538.6+0443	84.6630	4.7262	4.51	$(1.6 \pm 0.45) \times 10^{-12}$	0.9982	0.0018
4FGL J1401.1-3717	210.2971	-37.2975	10.62	$(3.1 \pm 0.47) \times 10^{-12}$	0.9980	0.0020
4FGL J1846.7+7238	281.6849	72.6371	8.04	$(1.4 \pm 0.25) \times 10^{-12}$	0.9978	0.0022
4FGL J2142.1+4501	325.5291	45.0182	6.10	$(1.8 \pm 0.39) \times 10^{-12}$	0.9976	0.0024
4FGL J0215.3+7555	33.8285	75.9190	7.26	$(1.5 \pm 0.34) \times 10^{-12}$	0.9975	0.0025
4FGL J1535.3-3135	233.8391	-31.5907	6.59	$(1.7 \pm 0.39) \times 10^{-12}$	0.9973	0.0027
4FGL J0606.5-4730	91.6416	-47.5038	13.57	$(3.3 \pm 0.38) \times 10^{-12}$	0.9972	0.0028
4FGL J0507.4-3346	76.8591	-33.7813	13.88	$(3.0 \pm 0.38) \times 10^{-12}$	0.9971	0.0029
4FGL J0954.2-2520	148.5681	-25.3384	8.47	$(2.1 \pm 0.36) \times 10^{-12}$	0.9971	0.0029
4FGL J1943.6-0533	295.9249	-5.5665	4.86	$(2.2 \pm 0.53) \times 10^{-12}$	0.9971	0.0029
4FGL J1234.0-5735	188.5194	-57.5961	29.72	$(13.5 \pm 0.99) \times 10^{-12}$	0.9970	0.0030
4FGL J0213.8-6949	33.4704	-69.8311	8.96	$(1.4 \pm 0.27) \times 10^{-12}$	0.9970	0.0030
4FGL J1412.0+3836	213.0130	38.6102	8.30	$(1.4 \pm 0.27) \times 10^{-12}$	0.9970	0.0030
4FGL J0830.1-0946	127.5427	-9.7728	7.53	$(1.8 \pm 0.36) \times 10^{-12}$	0.9970	0.0030
4FGL J1537.9-1344	234.4867	-13.7335	5.76	$(1.6 \pm 0.40) \times 10^{-12}$	0.9969	0.0031
4FGL J2142.4+3659	325.6020	36.9856	9.83	$(2.8 \pm 0.43) \times 10^{-12}$	0.9969	0.0031
4FGL J1240.4-7148	190.1160	-71.8156	21.15	$(7.7 \pm 0.61) \times 10^{-12}$	0.9969	0.0031
4FGL J0620.5-2512	95.1445	-25.2129	17.24	$(7.8 \pm 0.70) \times 10^{-12}$	0.0023	0.9977
4FGL J0900.6-7408	135.1721	-74.1440	8.25	$(3.6 \pm 0.54) \times 10^{-12}$	0.0028	0.9972
4FGL J2057.4-0723	314.3535	-7.3901	8.64	$(3.9 \pm 0.53) \times 10^{-12}$	0.0033	0.9967
4FGL J1830.2-4443	277.5504	-44.7200	23.11	$(10.0 \pm 0.72) \times 10^{-12}$	0.0034	0.9966
4FGL J0138.6+2923	24.6637	29.3855	7.20	$(2.5 \pm 0.46) \times 10^{-12}$	0.0036	0.9964
4FGL J0616.7-1049	94.1761	-10.8230	6.02	$(5.1 \pm 1.11) \times 10^{-12}$	0.0037	0.9963
4FGL J0732.7-4638	113.1774	-46.6488	11.17	$(4.9 \pm 0.97) \times 10^{-12}$	0.0037	0.9963
4FGL J0953.1-3005	148.2779	-30.0979	10.08	$(3.5 \pm 0.51) \times 10^{-12}$	0.0041	0.9959
4FGL J0841.0-2744	130.2630	-27.7468	6.09	$(2.6 \pm 0.54) \times 10^{-12}$	0.0043	0.9957
4FGL J0348.8+4610	57.2185	46.1695	6.51	$(3.6 \pm 0.94) \times 10^{-12}$	0.0046	0.9954
4FGL J2139.9+3910	324.9929	39.1711	3.72	$(2.6 \pm 0.67) \times 10^{-12}$	0.0050	0.9950
4FGL J0008.0-3937	2.0048	-39.6320	5.44	$(2.1 \pm 0.41) \times 10^{-12}$	0.0052	0.9948
4FGL J1437.3-3239	219.3259	-32.6569	5.17	$(1.7 \pm 0.53) \times 10^{-12}$	0.0053	0.9947
4FGL J0118.7-0848	19.6884	-8.8080	7.56	$(2.7 \pm 0.43) \times 10^{-12}$	0.0053	0.9947
4FGL J2141.7-6410	325.4305	-64.1792	65.83	$(25.0 \pm 0.78) \times 10^{-12}$	0.0054	0.9946
4FGL J1821.6+6819	275.4034	68.3242	34.47	$(12.1 \pm 0.86) \times 10^{-12}$	0.0055	0.9945
4FGL J0429.0-0006	67.2549	-0.1006	3.39	$(2.3 \pm 0.63) \times 10^{-12}$	0.0055	0.9945
4FGL J0501.0-2423	75.2732	-24.3935	5.11	$(3.5 \pm 0.72) \times 10^{-12}$	0.0059	0.9941
4FGL J2318.2+1915	349.5568	19.2560	13.17	$(6.2 \pm 0.56) \times 10^{-12}$	0.0059	0.9941
4FGL J1421.6-4819	215.4125	-48.3317	6.61	$(3.8 \pm 0.85) \times 10^{-12}$	0.0059	0.9941

comparison of our results with those presented in **(author?)** [38] where the BCUs from 4FGL DR2 (a catalogue version preceding 4FGL DR3) are classified using Bayesian neural networks. Applying tight selection criteria, their list contains 429 BL Lacs and 178 FSRQs. Among their BL Lac candidates 355 (82.7%) objects are in agreement with our prediction and we found a difference in 74. Among those 74, in 4FGL DR3 53 objects have already been classified as BL Lacs, 2 as FSRQs and 1 as normal galaxy; 13 objects were dropped by us because of insufficient spectral data (see Section 6.3). So disagreement is found only with 5 objects: all remained unclassified. Similarly, out of 178 FSRQs in their list, 148 (83.1%) match with our results; from the remaining 31 sources in 4FGL DR3 4 have already been classified as FSRQs and 2 are missing, we excluded 6 objects, 13 objects remained unclassified with a probability between $L_{BL\,Lac} = 0.18 - 0.44$ and we found disagreement for 5 objects. Similar picture can be drawn when comparing with the BL Lac and FSRQ list by applying loose selection criteria. Thus, our results are in a good agreement with those presented in **(author?)** [38] and obtained by a different method.

6.4.1 BL Lac and FSRQ candidates versus BL Lacs and FSRQs

The idea of the classification presented in the previous subsection is to identify new BL Lac and FSRQ candidates among the unclassified blazars. In this subsection, we compare and contrast the properties of newly identified and known sources.

The spectral difference between BL Lacs and FSRQs in 0.1-300 GeV band is well known. The distribution of power-law photon indexes of BL Lacs and FSRQs from 4FGL are shown in Fig. 6.6 left and right panels, respectively (blue and orange shaded areas). The mean and standard deviation of these distributions is 2.03 ± 0.21 for BL Lacs and 2.47 ± 0.20 for FSRQs; on the average, BL Lacs spectra are harder than those of FSRQs. The distribution of newly classified BL Lac and FSRQ candidates is shown by filled blue and orange areas in the left and right panels of Fig. 6.6, respectively. The distribution of likely BL Lacs and FSRQs is centered on 2.09 ± 0.21 and 2.57 ± 0.14, respectively, in an excellent agreement with the distributions of known BL Lacs and FSRQs. Thus, BL Lacs and FSRQs classified from BCUs have similar spectral characteristics as compared with those derived for known sources.

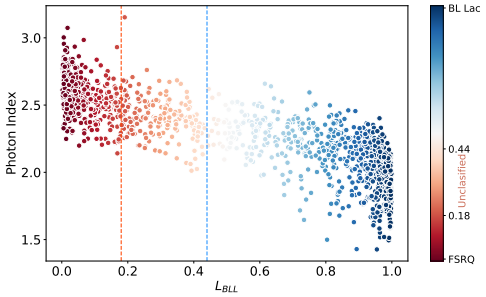

Figure 6.7: Photon index versus the probability. The color bar shows the probabilities of source associations: FSRQs are in dark red and BL Lacs in dark blue.

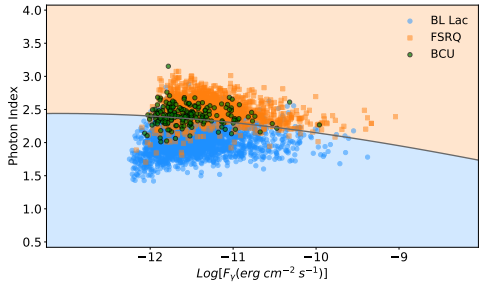

Figure 6.8: Photon index versus energy flux above 100 MeV. The curve represents the approximate boundary of two sub-classes separation.

As the power-law index was not considered in the model training, this comparison is an effective way to illustrate the power of our method.

Another way to visualize the power-law photon index difference between BL Lacs and FSRQs is to plot the photon index versus $L_{BL\,Lac}$ (Fig. 6.7). There is a clear correlation between the photon index and probability; higher $L_{BL\,Lac}$ corresponds to lower index and vice-versa. This very well follows the spectral trend observed for BL Lacs and FSRQs, namely higher $L_{BL\,Lac}$ (more likely BL Lacs) corresponds to harder spectra while FSRQs (lower $L_{BL\,Lac}$) appear with softer spectra.

Vertical blue and orange dashed lines show the classification threshold defined for BL Lacs and FSRQs. 57.2 % of total BCUs are classified as BL Lacs (right region from the blue dashed line in Fig. 6.7) and 28.9 % are FSRQs (left region from the orange dashed line in Fig. 6.7). The sources falling between the orange and blue dashed lines (13.9 %) remain unclassified, their

power-law index is in the range defined for BL Lacs and FSRQs.

The increased number of BL Lacs and FSRQs (2261 and 1188, respectively) allows to compare their properties with improved statistics. A convenient way to compare the properties of different blazar classes is through plotting the power-law photon index versus the flux (Fig. 6.8). Since the spectra of some sources deviate from the simple power-law model, we computed the energy flux between 100 MeV and 100 GeV using the power-law model parameters given in 4FGL, namely, reported flux density, pivot energy and power-law photon index. The BL Lacs and FSRQs both from 4FGL and classified from BCUs are shown in blue and orange, respectively and the remaining unclassified BCUs are in green. The reported energy fluxes vary from $5.62 \times 10^{-13}\, erg\, cm^{-2}\, s^{-1}$ to $9.06 \times 10^{-10}\, erg\, cm^{-2}\, s^{-1}$ while the photon index is in the range from 1.42 to 3.08. A Kolmogorov–Smirnov test gives a probability of 0.31 that FSRQs and FSRQ candidates come from the same parent population and the probability is 0.15 for the BL Lacs and BL Lac candidates. From the distribution it is possible to quantify the space occupied by BL Lacs and FSRQs in the photon index versus energy flux plane. The boundary between these two classes (decision boundary) was found by using Gaussian naive Bayes classification. The black line in Fig. 6.8 is the decision boundary, which corresponds to the curve that optimally separates the two classes. In other words, by computing the probabilities the algorithm optimally divides the plane in a such way as to have the highest number of BL Lacs and FSRQs below and above the line, respectively. The boundary line defines $\simeq$ 2.41, 2.31 and 2.15 indices at $10^{-12}\, erg\, cm^{-2}\, s^{-1}$, $10^{-11}\, erg\, cm^{-2}\, s^{-1}$ and $10^{-10}\, erg\, cm^{-2}\, s^{-1}$ fluxes, respectively, well separating the two-classes: 91.2 % of BL Lacs occupy the region below the line while 86.1 % of FSRQs are above. The remaining BCUs (green circles in Fig. 6.8) are distributed above and below the limit; 65.1% of BCUs occupy the space more characteristic for FSRQs, while 34.9 % show properties more similar to BL Lacs. The limit presented in Fig. 6.8, which is a physical distinction between the two classes of blazars, BL Lacs and FSRQs, based on photon index and flux, was obtained using a large number of BL Lacs and FSRQs, 3449 in total. The accuracy of Gaussian naive Bayes classification is 90% implying the line satisfactorily well separates the two classes of blazars. Even if this is not a strict limit, it still can be used as a reference limit for BL Lac and FSRQ division.

It is also interesting to compare the photon index with the frequency of the synchrotron peak ($\nu_{s,p}$). In the previous studies, a strong anticorrelation between these two parameters was already reported [e.g., 9, 14]. Now, with up-

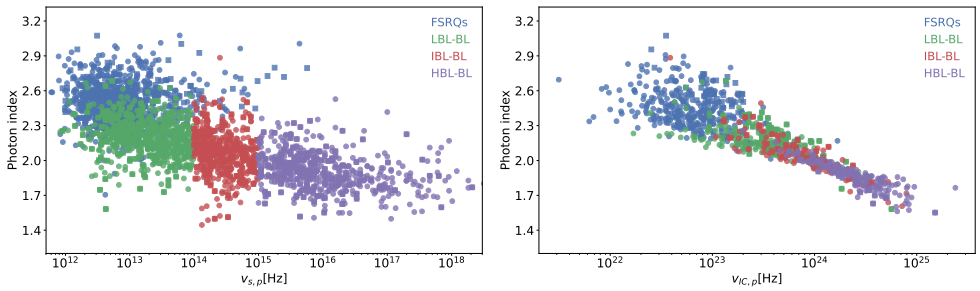

Figure 6.9: Left panel: γ-ray photon index versus the synchrotron peak frequency. Right panel: γ-ray photon index versus the inverse Compton peak frequency. The FSRQs, LBLs, IBLs and HBLs are in blue, green, red and purple, respectively. BL Lacs and FSRQs from 4FGL are shown with circles, while BL Lac and FSRQ candidates are with squares.

dated number of BL Lacs and FSRQs tighter constraints on the photon index distribution on different blazar types can be obtained [2]. Fig. 6.9 (left panel) shows the photon index versus $\nu_{s,p}$ where BL Lacs are separated into LBL, IBL and HBL classes. We note that also FSRQs are mostly LBLs, but we show and discuss their properties by separating them from BL Lacs that are classified as LBLs, IBLs and HBLs. For the FSRQs (blue), LBLs (green), IBLs (red) and HBLs (purple) the mean and rms of the photon index are 2.49 ± 0.18, 2.20 ± 0.16, 2.06 ± 0.18 and 1.90 ± 0.16, respectively. As expected, the distributions of FSRQs and LBLs are similar but LBLs have a slightly harder γ-ray photon index, but, clearly, as compared with them IBLs and HBLs occupy a different region in the γ-ray photon index $\nu_{s,p}$ plane; the γ-ray photon index becomes smaller (harder) from FSRQs to HBLs, $\Gamma_{\gamma,FSRQs} > \Gamma_{\gamma,LBLs} > \Gamma_{\gamma,IBLs} > \Gamma_{\gamma,HBLs}$.

The distribution of the high energy peak frequency (referred as inverse-Compton peak $\nu_{IC,p}$) for the considered sources is shown in Fig. 6.9 (right panel). This is a new parameter available in the fourth catalog of AGNs detected by Fermi LAT - Data Release 3 [15] which has been estimated by fitting the significantly curved spectrum with a log-parabolic model. For the current study, we excluded all the sources for which the uncertainty on the high energy peak estimation is large (requiring the value to be larger than $1.5\times$ error) which resulted in 893 blazars with measured $\nu_{IC,p}$, among which 369

[2] We note that for a more meaningful comparison, $\nu_{s,p}$ should be corrected by a factor of $1+z$ but this will reduce the source sample size, as z is not measured for many sources.

are FSRQs, 217 are LBLs, 143 are IBLs and 164 are HBLs. The distributions of LBLs, IBLs and HBLs overlap and are slightly separated from FSRQs toward higher frequencies. The fit of the linear function $\Gamma_\gamma = \Gamma_0 + \alpha \times \nu_{IC,p}$ yields $\alpha = -0.21 \pm 0.02$ and $\alpha = -0.31 \pm 0.01$ for FSRQs and BL Lacs (considering all LBLs, IBLs and HBLs), respectively. This shows that Γ_γ of BL Lacs becomes steeper with increasing $\nu_{IC,p}$.

The comparison of synchrotron ($\nu_{s,p}$) and high energy ($\nu_{IC,p}$) peak frequencies estimated for different blazar sub-classes is shown in Fig. 6.10. In general, the $\nu_{IC,p}$ of FSRQs is at lower frequencies than those of BL Lacs which in their turn show different tendencies for LBLs, IBLs and HBLs. $\nu_{IC,p}$ increases along with the increase of $\nu_{s,p}$; the linear fit ($\nu_{IC,p} = \nu_0 + \kappa \times \nu_{s,p}$) for BL Lacs shows a slope of $\kappa = 0.33 \pm 0.01$. Only 10.1% of LBLs have $\nu_{IC,p}$ above 10^{24} Hz, while the percentage is 41.2% for IBLs and 89.0% for HBLs. The difference between the FSRQs and BL Lacs as well as between LBLs, IBLs and HBLs is expected from simple theoretical considerations. Within a simple one-zone synchrotron/synchrotron-self Compton (SSC) model, which is successfully applied to model the SEDs of BL Lacs [e.g., see 69], assuming Thomson regime for the inverse Compton scattering, $\nu_{s,p}$ and $\nu_{IC,p}$ are linked by $\nu_{IC,p}/\nu_{s,p} = 4/3(\gamma_p^{SSC})^2$. So, it is natural that for the sources with higher synchrotron peak (HBLs) also $\nu_{IC,p}$ is at higher frequencies. However, the $\nu_{s,p}$ and $\nu_{IC,p}$ relation is not valid for the FSRQs, where the high energy emission is most likely due to inverse Compton scattering of external photons (UV and IR external radiation fields which usually dominate over the jet synchrotron emission), so the $\nu_{IC,p}$ scales with the average energy of up-scattered photons and bulk Lorentz factor of the emitting region.

6.5 Conclusions

In this paper, we performed machine learning classification of blazar candidates of uncertain type. By training and constructing predictive models which forecast the likelihood of a source to belong to a particular class of blazars, the classification of BCUs based on their direct observable spectral and temporal properties in the γ-ray band is conducted.

The models were trained on the set of γ-ray parameters (spectra and light curves) of BL Lacs and FSRQs from the latest and most detailed γ-ray catalog (4FGL DR3) which is based on accumulation of data in twelve years (2008-2022). Different machine learning algorithms were applied to classify

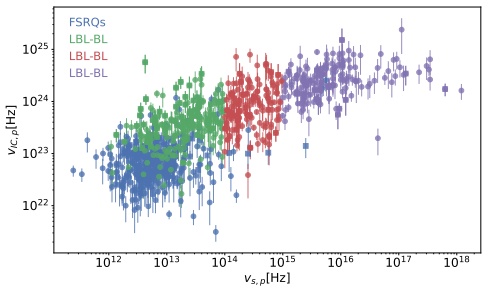

Figure 6.10: The synchrotron peak frequency ($\nu_{s,p}$) as a function of the high energy peak frequency ($\nu_{IC,p}$). The same color code and plot markers as in Fig. 6.9.

blazars by dividing the entire data set into 80% and 20% train and test subsets and performing 15 fold cross validation. The algorithms based on gradient-boosted decision trees are preferred and outperform the other models because the available data set is comparatively small and contains missing data points. As a result, *LightGBM*- a state-of-the-art classification model based on gradient boosted trees shows the highest performance with a weighted recall of 0.88 and precision of 0.88.

The best model was applied to 1420 BCUs included in 4FGL to obtain the probability of their association to one of the blazar sub-classes and address the question of their nature. As a result, among the BCUs 825 (58.1%) are BL Lac candidates, 405 (28.5%) are FSRQ candidates and only 190 (13.3%) cannot be classified by our model. The γ-ray spectral properties (e.g., power-law photon index) of already classified and BL Lac and FSRQ candidates are in an excellent agreement, showing the validity of our model.

The results of BCU classification reported here although cannot conclusively give the type of a BCU but they can be useful for statistical population studies or for planing optical monitoring of blazars. For example, the distributions of BL Lacs and FSRQs from a more complete list show clustering in the photon index and energy flux plane, clearly separating those two sub-classes. According to this criteria, the majority of BCUs (65.1%) that remained unclassified in our model show properties more similar to FSRQs. For a larger blazar sample, the distribution of the synchrotron peak frequency ($\nu_{s,p}$) versus the γ-ray photon index confirms the strong difference between FSRQs and BL Lacs as well as between LBLs, IBLs and HBLs. In the distribution of the high energy peak frequency versus the γ-ray photon index most

of the FSRQs occupy the region of $\Gamma_\gamma > 2.3$ and $\nu_{IC,p} < 10^{23}$ Hz whereas $\nu_{IC,p}$ of BL Lacs can reach higher frequencies with harder γ-ray photon index, however no distinction between LBLs, IBLs and HBLs sublasses is possible. Instead, the comparison of $\nu_{s,p}$ and $\nu_{IC,p}$ shows a remarkable difference between FSRQs and BL Lacs as well as between LBLs, IBLs and HBLs. The BL Lacs have much larger $\nu_{IC,p}$ with a mean of 1.6×10^{24} Hz as compared with that of FSRQS with 1.1×10^{23}; 43.3% of BL Lacs have a peak above 10^{24} Hz. Among BL Lacs, HBLs have higher $\nu_{IC,p}$ (for 89.0% of HBLs $\nu_{IC,p} \geq 10^{24}$ Hz) whereas it is lower for LBLs; the linear fit shows a slope of 0.33 ± 0.01, so $\nu_{IC,p}$ increases with $\nu_{s,p}$. Such a correlation is in agreement with expectations from one-zone synchrotron-self-Compton scenarios.

Bibliography

[1] A. A. Abdo, M. Ackermann, I. Agudo, M. Ajello, A. Allafort, H. D. Aller, M. F. Aller, E. Antolini, A. A. Arkharov, M. Axelsson, U. Bach, L. Baldini, J. Ballet, G. Barbiellini, D. Bastieri, K. Bechtol, R. Bellazzini, A. Berdyugin, B. Berenji, R. D. Blandford, D. A. Blinov, E. D. Bloom, M. Boettcher, E. Bonamente, A. W. Borgland, A. Bouvier, J. Bregeon, A. Brez, M. Brigida, P. Bruel, R. Buehler, C. S. Buemi, T. H. Burnett, S. Buson, G. A. Caliandro, R. A. Cameron, P. A. Caraveo, D. Carosati, S. Carrigan, J. M. Casandjian, E. Cavazzuti, C. Cecchi, Ö. Çelik, A. Chekhtman, W. P. Chen, C. C. Cheung, J. Chiang, S. Ciprini, R. Claus, J. Cohen-Tanugi, J. Conrad, S. Corbel, L. Costamante, C. D. Dermer, A. de Angelis, F. de Palma, D. Donato, E. do Couto e. Silva, P. S. Drell, R. Dubois, D. Dumora, C. Farnier, C. Favuzzi, S. J. Fegan, E. C. Ferrara, W. B. Focke, E. Forné, P. Fortin, Y. Fukazawa, S. Funk, P. Fusco, F. Gargano, D. Gasparrini, N. Gehrels, S. Germani, B. Giebels, N. Giglietto, F. Giordano, M. Giroletti, T. Glanzman, G. Godfrey, I. A. Grenier, J. E. Grove, S. Guiriec, M. A. Gurwell, C. Gusbar, J. L. Gómez, D. Hadasch, V. A. Hagen-Thorn, M. Hayashida, E. Hays, D. Horan, R. E. Hughes, G. Jóhannesson, A. S. Johnson, W. N. Johnson, T. Kamae, H. Katagiri, J. Kataoka, N. Kawai, G. Kimeridze, J. Knödlseder, T. S. Konstantinova, E. N. Kopatskaya, E. Koptelova, Y. Y. Kovalev, O. M. Kurtanidze, M. Kuss, A. Lahteenmaki, J. Lande, V. M. Larionov, E. G. Larionova, L. V. Larionova, S. Larsson, L. Latronico, S. H. Lee, P. Leto, M. L. Lister, F. Longo, F. Loparco, B. Lott, M. N. Lovellette, P. Lubrano, G. M. Madejski, A. Makeev, E. Massaro, M. N. Mazziotta, W. McConville, J. E. McEnery, I. M. McHardy, P. F. Michelson, W. Mitthumsiri, T. Mizuno, A. A. Moiseev, C. Monte, M. E. Monzani, D. A. Morozova, A. Morselli, I. V. Moskalenko, S. Murgia, M. Naumann-Godo, M. G. Nikolashvili, P. L. Nolan, J. P. Norris, E. Nuss, M. Ohno, T. Ohsugi, A. Okumura, N. Omodei, E. Orlando, J. F. Ormes, M. Ozaki, D. Paneque, J. H. Panetta, D. Par-

ent, M. Pasanen, V. Pelassa, M. Pepe, M. Pesce-Rollins, F. Piron, T. A. Porter, A. B. Pushkarev, S. Rainò, C. M. Raiteri, R. Rando, M. Razzano, A. Reimer, O. Reimer, R. Reinthal, J. Ripken, S. Ritz, M. Roca-Sogorb, A. Y. Rodriguez, M. Roth, P. Roustazadeh, F. Ryde, H. F. W. Sadrozinski, A. Sander, J. D. Scargle, C. Sgrò, L. A. Sigua, P. D. Smith, K. Sokolovsky, G. Spandre, P. Spinelli, J. L. Starck, M. S. Strickman, D. J. Suson, H. Takahashi, T. Takahashi, L. O. Takalo, T. Tanaka, B. Taylor, J. B. Thayer, J. G. Thayer, D. J. Thompson, L. Tibaldo, M. Tornikoski, D. F. Torres, G. Tosti, A. Tramacere, C. Trigilio, I. S. Troitsky, G. Umana, T. L. Usher, J. Vandenbroucke, V. Vasileiou, N. Vilchez, M. Villata, V. Vitale, A. P. Waite, P. Wang, B. L. Winer, K. S. Wood, Z. Yang, T. Ylinen, and M. Ziegler.

Fermi Large Area Telescope and Multi-wavelength Observations of the Flaring Activity of PKS 1510-089 between 2008 September and 2009 June.

ApJ, 721(2):1425–1447, October 2010.

[2] A. A. Abdo, M. Ackermann, I. Agudo, M. Ajello, H. D. Aller, M. F. Aller, E. Angelakis, A. A. Arkharov, M. Axelsson, U. Bach, L. Baldini, J. Ballet, G. Barbiellini, D. Bastieri, B. M. Baughman, K. Bechtol, R. Bellazzini, E. Benitez, A. Berdyugin, B. Berenji, R. D. Bland ford, E. D. Bloom, M. Boettcher, E. Bonamente, A. W. Borgland, J. Bregeon, A. Brez, M. Brigida, P. Bruel, T. H. Burnett, D. Burrows, S. Buson, G. A. Caliandro, L. Calzoletti, R. A. Cameron, M. Capalbi, P. A. Caraveo, D. Carosati, J. M. Casand jian, E. Cavazzuti, C. Cecchi, Ö. Çelik, E. Charles, S. Chaty, A. Chekhtman, W. P. Chen, J. Chiang, G. Chincarini, S. Ciprini, R. Claus, J. Cohen-Tanugi, S. Colafrancesco, L. R. Cominsky, J. Conrad, L. Costamante, S. Cutini, F. D'ammando, R. Deitrick, V. D'Elia, C. D. Dermer, A. de Angelis, F. de Palma, S. W. Digel, I. Donnarumma, E. do Couto e. Silva, P. S. Drell, R. Dubois, D. Dultzin, D. Dumora, A. Falcone, C. Farnier, C. Favuzzi, S. J. Fegan, W. B. Focke, E. Forné, P. Fortin, M. Frailis, L. Fuhrmann, Y. Fukazawa, S. Funk, P. Fusco, J. L. Gómez, F. Gargano, D. Gasparrini, N. Gehrels, S. Germani, B. Giebels, N. Giglietto, P. Giommi, F. Giordano, A. Giuliani, T. Glanzman, G. Godfrey, I. A. Grenier, C. Gronwall, J. E. Grove, L. Guillemot, S. Guiriec, M. A. Gurwell, D. Hadasch, Y. Hanabata, A. K. Harding, M. Hayashida, E. Hays, S. E. Healey, J. Heidt,

D. Hiriart, D. Horan, E. A. Hoversten, R. E. Hughes, R. Itoh, M. S. Jackson, G. Jóhannesson, A. S. Johnson, W. N. Johnson, S. G. Jorstad, M. Kadler, T. Kamae, H. Katagiri, J. Kataoka, N. Kawai, J. Kennea, M. Kerr, G. Kimeridze, J. Knödlseder, M. L. Kocian, E. N. Kopatskaya, E. Koptelova, T. S. Konstantinova, Y. Y. Kovalev, Yu. A. Kovalev, O. M. Kurtanidze, M. Kuss, J. Lande, V. M. Larionov, L. Latronico, P. Leto, E. Lindfors, F. Longo, F. Loparco, B. Lott, M. N. Lovellette, P. Lubrano, G. M. Madejski, A. Makeev, P. Marchegiani, A. P. Marscher, F. Marshall, W. Max-Moerbeck, M. N. Mazziotta, W. McConville, J. E. McEnery, C. Meurer, P. F. Michelson, W. Mitthumsiri, T. Mizuno, A. A. Moiseev, C. Monte, M. E. Monzani, A. Morselli, I. V. Moskalenko, S. Murgia, I. Nestoras, K. Nilsson, N. A. Nizhelsky, P. L. Nolan, J. P. Norris, E. Nuss, T. Ohsugi, R. Ojha, N. Omodei, E. Orlando, J. F. Ormes, J. Osborne, M. Ozaki, L. Pacciani, P. Padovani, C. Pagani, K. Page, D. Paneque, J. H. Panetta, D. Parent, M. Pasanen, V. Pavlidou, V. Pelassa, M. Pepe, M. Perri, M. Pesce-Rollins, S. Piranomonte, F. Piron, C. Pittori, T. A. Porter, S. Puccetti, F. Rahoui, S. Rainò, C. Raiteri, R. Rando, M. Razzano, A. Reimer, O. Reimer, T. Reposeur, J. L. Richards, S. Ritz, L. S. Rochester, A. Y. Rodriguez, R. W. Romani, J. A. Ros, M. Roth, P. Roustazadeh, F. Ryde, H. F. W. Sadrozinski, A. Sadun, D. Sanchez, A. Sander, P. M. Saz Parkinson, J. D. Scargle, A. Sellerholm, C. Sgrò, M. S. Shaw, L. A. Sigua, E. J. Siskind, D. A. Smith, P. D. Smith, G. Spandre, P. Spinelli, J. L. Starck, M. Stevenson, G. Stratta, M. S. Strickman, D. J. Suson, H. Tajima, H. Takahashi, T. Takahashi, L. O. Takalo, T. Tanaka, J. B. Thayer, J. G. Thayer, D. J. Thompson, L. Tibaldo, D. F. Torres, G. Tosti, A. Tramacere, Y. Uchiyama, T. L. Usher, V. Vasileiou, F. Verrecchia, N. Vilchez, M. Villata, V. Vitale, A. P. Waite, P. Wang, B. L. Winer, K. S. Wood, T. Ylinen, J. A. Zensus, G. V. Zhekanis, and M. Ziegler.
The Spectral Energy Distribution of Fermi Bright Blazars.
ApJ, 716(1):30–70, June 2010.

[3] A. A. Abdo, M. Ackermann, M. Ajello, W. B. Atwood, M. Axelsson, L. Baldini, J. Ballet, G. Barbiellini, D. Bastieri, B. M. Baughman, K. Bechtol, R. Bellazzini, B. Berenji, E. D. Bloom, G. Bogaert, E. Bonamente, A. W. Borgland, J. Bregeon, A. Brez, M. Brigida, P. Bruel, T. H. Burnett, G. A. Caliandro, R. A. Cameron, P. A. Caraveo, J. M.

Casandjian, E. Cavazzuti, C. Cecchi, Ö. Çelik, A. Chekhtman, C. C. Cheung, J. Chiang, S. Ciprini, R. Claus, J. Cohen-Tanugi, J. Conrad, S. Cutini, C. D. Dermer, A. de Angelis, F. de Palma, S. W. Digel, E. do Couto e. Silva, P. S. Drell, R. Dubois, D. Dumora, C. Farnier, C. Favuzzi, S. J. Fegan, E. C. Ferrara, W. B. Focke, M. Frailis, L. Fuhrmann, Y. Fukazawa, S. Funk, P. Fusco, F. Gargano, D. Gasparrini, N. Gehrels, S. Germani, B. Giebels, N. Giglietto, F. Giordano, M. Giroletti, T. Glanzman, G. Godfrey, I. A. Grenier, M. H. Grondin, J. E. Grove, L. Guillemot, S. Guiriec, Y. Hanabata, A. K. Harding, M. Hayashida, E. Hays, R. E. Hughes, G. Jóhannesson, A. S. Johnson, R. P. Johnson, W. N. Johnson, M. Kadler, T. Kamae, H. Katagiri, J. Kataoka, M. Kerr, J. Knödlseder, M. L. Kocian, F. Kuehn, M. Kuss, J. Lande, L. Latronico, M. Lemoine-Goumard, F. Longo, F. Loparco, B. Lott, M. N. Lovellette, P. Lubrano, G. M. Madejski, A. Makeev, M. Marelli, E. Massaro, W. Max-Moerbeck, M. N. Mazziotta, W. McConville, J. E. McEnery, C. Meurer, P. F. Michelson, W. Mitthumsiri, T. Mizuno, A. A. Moiseev, C. Monte, M. E. Monzani, A. Morselli, I. V. Moskalenko, S. Murgia, P. L. Nolan, J. P. Norris, E. Nuss, T. Ohsugi, N. Omodei, E. Orlando, J. F. Ormes, M. Ozaki, D. Paneque, J. H. Panetta, D. Parent, V. Pavlidou, T. J. Pearson, V. Pelassa, M. Pepe, M. Pesce-Rollins, F. Piron, T. A. Porter, S. Rainò, R. Rando, M. Razzano, S. Razzaque, A. Readhead, A. Reimer, O. Reimer, T. Reposeur, J. L. Richards, S. Ritz, L. S. Rochester, A. Y. Rodriguez, R. W. Romani, M. Roth, F. Ryde, H. F. W. Sadrozinski, D. Sanchez, A. Sander, P. M. Saz Parkinson, J. D. Scargle, C. Sgrò, M. S. Shaw, E. J. Siskind, D. A. Smith, P. D. Smith, G. Spandre, P. Spinelli, M. Stevenson, M. S. Strickman, D. J. Suson, H. Tajima, H. Takahashi, T. Tanaka, J. B. Thayer, J. G. Thayer, D. J. Thompson, L. Tibaldo, O. Tibolla, D. F. Torres, G. Tosti, A. Tramacere, P. Ubertini, Y. Uchiyama, T. L. Usher, V. Vasileiou, N. Vilchez, V. Vitale, A. P. Waite, P. Wang, B. L. Winer, K. S. Wood, H. Yasuda, T. Ylinen, J. A. Zensus, M. Ziegler, Fermi LAT Collaboration, E. Angelakis, T. Hovatta, E. Hoversten, Y. Ikejiri, K. S. Kawabata, Y. Y. Kovalev, Yu. A. Kovalev, T. P. Krichbaum, M. L. Lister, A. Lähteenmäki, N. Marchili, P. Ogle, C. Pagani, A. B. Pushkarev, K. Sakimoto, M. Sasada, M. Tornikoski, M. Uemura, M. Yamanaka, T. Yamashita, Fermi LAT Collaboration, and Multifrequency Campaign Collaboration.

PKS 1502+106: A New and Distant Gamma-ray Blazar in Outburst Discovered by the Fermi Large Area Telescope.
ApJ, 710(1):810–827, February 2010.

[4] A. A. Abdo, M. Ackermann, M. Ajello, W. B. Atwood, L. Baldini, J. Ballet, G. Barbiellini, D. Bastieri, B. M. Baughman, K. Bechtol, R. Bellazzini, B. Berenji, R. D. Blandford, E. D. Bloom, E. Bonamente, A. W. Borgland, J. Bregeon, A. Brez, M. Brigida, P. Bruel, T. H. Burnett, S. Buson, G. A. Caliandro, R. A. Cameron, P. A. Caraveo, J. M. Casandjian, E. Cavazzuti, C. Cecchi, Ö. Çelik, E. Charles, A. Chekhtman, C. C. Cheung, J. Chiang, S. Ciprini, R. Claus, J. Cohen-Tanugi, L. R. Cominsky, J. Conrad, S. Cutini, C. D. Dermer, A. de Angelis, F. de Palma, S. W. Digel, G. di Bernardo, E. do Couto e Silva, P. S. Drell, A. Drlica-Wagner, R. Dubois, D. Dumora, C. Farnier, C. Favuzzi, S. J. Fegan, W. B. Focke, P. Fortin, M. Frailis, Y. Fukazawa, S. Funk, P. Fusco, D. Gaggero, F. Gargano, D. Gasparrini, N. Gehrels, S. Germani, B. Giebels, N. Giglietto, P. Giommi, F. Giordano, T. Glanzman, G. Godfrey, I. A. Grenier, M. H. Grondin, J. E. Grove, L. Guillemot, S. Guiriec, M. Gustafsson, Y. Hanabata, A. K. Harding, M. Hayashida, R. E. Hughes, R. Itoh, M. S. Jackson, G. Jóhannesson, A. S. Johnson, R. P. Johnson, T. J. Johnson, W. N. Johnson, T. Kamae, H. Katagiri, J. Kataoka, N. Kawai, M. Kerr, J. Knödlseder, M. L. Kocian, F. Kuehn, M. Kuss, J. Lande, L. Latronico, M. Lemoine-Goumard, F. Longo, F. Loparco, B. Lott, M. N. Lovellette, P. Lubrano, G. M. Madejski, A. Makeev, M. N. Mazziotta, W. McConville, J. E. McEnery, C. Meurer, P. F. Michelson, W. Mitthumsiri, T. Mizuno, A. A. Moiseev, C. Monte, M. E. Monzani, A. Morselli, I. V. Moskalenko, S. Murgia, P. L. Nolan, J. P. Norris, E. Nuss, T. Ohsugi, N. Omodei, E. Orlando, J. F. Ormes, D. Paneque, J. H. Panetta, D. Parent, V. Pelassa, M. Pepe, M. Pesce-Rollins, F. Piron, T. A. Porter, S. Rainò, R. Rando, M. Razzano, A. Reimer, O. Reimer, T. Reposeur, S. Ritz, L. S. Rochester, A. Y. Rodriguez, M. Roth, F. Ryde, H. F. W. Sadrozinski, D. Sanchez, A. Sander, P. M. Saz Parkinson, J. D. Scargle, A. Sellerholm, C. Sgrò, M. S. Shaw, E. J. Siskind, D. A. Smith, P. D. Smith, G. Spandre, P. Spinelli, J. L. Starck, M. S. Strickman, A. W. Strong, D. J. Suson, H. Tajima, H. Takahashi, T. Takahashi, T. Tanaka, J. B. Thayer, J. G. Thayer, D. J. Thompson, L. Tibaldo, D. F. Torres, G. Tosti, A. Tra-

macere, Y. Uchiyama, T. L. Usher, V. Vasileiou, N. Vilchez, V. Vitale, A. P. Waite, P. Wang, B. L. Winer, K. S. Wood, T. Ylinen, M. Ziegler, and Fermi LAT Collaboration.
Spectrum of the Isotropic Diffuse Gamma-Ray Emission Derived from First-Year Fermi Large Area Telescope Data.
Phys. Rev. Lett., 104(10):101101, March 2010.

[5] S. Abdollahi, F. Acero, M. Ackermann, M. Ajello, W. B. Atwood, M. Axelsson, L. Baldini, J. Ballet, G. Barbiellini, D. Bastieri, J. Becerra Gonzalez, R. Bellazzini, A. Berretta, E. Bissaldi, R. D. Blandford, E. D. Bloom, R. Bonino, E. Bottacini, T. J. Brandt, J. Bregeon, P. Bruel, R. Buehler, T. H. Burnett, S. Buson, R. A. Cameron, R. Caputo, P. A. Caraveo, J. M. Casandjian, D. Castro, E. Cavazzuti, E. Charles, S. Chaty, S. Chen, C. C. Cheung, G. Chiaro, S. Ciprini, J. Cohen-Tanugi, L. R. Cominsky, J. Coronado-Blázquez, D. Costantin, A. Cuoco, S. Cutini, F. D'Ammando, M. DeKlotz, P. de la Torre Luque, F. de Palma, A. Desai, S. W. Digel, N. Di Lalla, M. Di Mauro, L. Di Venere, A. Domínguez, D. Dumora, F. Fana Dirirsa, S. J. Fegan, E. C. Ferrara, A. Franckowiak, Y. Fukazawa, S. Funk, P. Fusco, F. Gargano, D. Gasparrini, N. Giglietto, P. Giommi, F. Giordano, M. Giroletti, T. Glanzman, D. Green, I. A. Grenier, S. Griffin, M. H. Grondin, J. E. Grove, S. Guiriec, A. K. Harding, K. Hayashi, E. Hays, J. W. Hewitt, D. Horan, G. Jóhannesson, T. J. Johnson, T. Kamae, M. Kerr, D. Kocevski, M. Kovac'evic', M. Kuss, D. Landriu, S. Larsson, L. Latronico, M. Lemoine-Goumard, J. Li, I. Liodakis, F. Longo, F. Loparco, B. Lott, M. N. Lovellette, P. Lubrano, G. M. Madejski, S. Maldera, D. Malyshev, A. Manfreda, E. J. Marchesini, L. Marcotulli, G. Martí-Devesa, P. Martin, F. Massaro, M. N. Mazziotta, J. E. McEnery, I. Mereu, M. Meyer, P. F. Michelson, N. Mirabal, T. Mizuno, M. E. Monzani, A. Morselli, I. V. Moskalenko, M. Negro, E. Nuss, R. Ojha, N. Omodei, M. Orienti, E. Orlando, J. F. Ormes, M. Palatiello, V. S. Paliya, D. Paneque, Z. Pei, H. Peña-Herazo, J. S. Perkins, M. Persic, M. Pesce-Rollins, V. Petrosian, L. Petrov, F. Piron, H. Poon, T. A. Porter, G. Principe, S. Rainò, R. Rando, M. Razzano, S. Razzaque, A. Reimer, O. Reimer, Q. Remy, T. Reposeur, R. W. Romani, P. M. Saz Parkinson, F. K. Schinzel, D. Serini, C. Sgrò, E. J. Siskind, D. A. Smith, G. Spandre, P. Spinelli, A. W. Strong, D. J. Suson, H. Tajima, M. N. Takahashi, D. Tak, J. B. Thayer, D. J. Thomp-

son, L. Tibaldo, D. F. Torres, E. Torresi, J. Valverde, B. Van Klaveren, P. van Zyl, K. Wood, M. Yassine, and G. Zaharijas.
Fermi Large Area Telescope Fourth Source Catalog.
ApJSS, 247(1):33, March 2020.

[6] S. Abdollahi, F. Acero, L. Baldini, J. Ballet, D. Bastieri, R. Bellazzini, B. Berenji, A. Berretta, E. Bissaldi, R. D. Blandford, E. Bloom, R. Bonino, A. Brill, R. J. Britto, P. Bruel, T. H. Burnett, S. Buson, R. A. Cameron, R. Caputo, P. A. Caraveo, D. Castro, S. Chaty, C. C. Cheung, G. Chiaro, N. Cibrario, S. Ciprini, J. Coronado-Blázquez, M. Crnogorcevic, S. Cutini, F. D'Ammando, S. De Gaetano, S. W. Digel, N. Di Lalla, F. Dirirsa, L. Di Venere, A. Domínguez, V. Fallah Ramazani, S. J. Fegan, E. C. Ferrara, A. Fiori, H. Fleischhack, A. Franckowiak, Y. Fukazawa, S. Funk, P. Fusco, G. Galanti, V. Gammaldi, F. Gargano, S. Garrappa, D. Gasparrini, F. Giacchino, N. Giglietto, F. Giordano, M. Giroletti, T. Glanzman, D. Green, I. A. Grenier, M. H. Grondin, L. Guillemot, S. Guiriec, M. Gustafsson, A. K. Harding, E. Hays, J. W. Hewitt, D. Horan, X. Hou, G. Jóhannesson, C. Karwin, T. Kayanoki, M. Kerr, M. Kuss, D. Landriu, S. Larsson, L. Latronico, M. Lemoine-Goumard, J. Li, I. Liodakis, F. Longo, F. Loparco, B. Lott, P. Lubrano, S. Maldera, D. Malyshev, A. Manfreda, G. Martí-Devesa, M. N. Mazziotta, I. Mereu, M. Meyer, P. F. Michelson, N. Mirabal, W. Mitthumsiri, T. Mizuno, A. A. Moiseev, M. E. Monzani, A. Morselli, I. V. Moskalenko, M. Negro, E. Nuss, N. Omodei, M. Orienti, E. Orlando, D. Paneque, Z. Pei, J. S. Perkins, M. Persic, M. Pesce-Rollins, V. Petrosian, R. Pillera, H. Poon, T. A. Porter, G. Principe, S. Rainò, R. Rando, B. Rani, M. Razzano, S. Razzaque, A. Reimer, O. Reimer, T. Reposeur, M. Sánchez-Conde, P. M. Saz Parkinson, L. Scotton, D. Serini, C. Sgrò, E. J. Siskind, D. A. Smith, G. Spandre, P. Spinelli, K. Sueoka, D. J. Suson, H. Tajima, D. Tak, J. B. Thayer, D. J. Thompson, D. F. Torres, E. Troja, J. Valverde, K. Wood, and G. Zaharijas.
Incremental Fermi Large Area Telescope Fourth Source Catalog.
ApJSS, 260(2):53, June 2022.

[7] M. Ackermann, M. Ajello, A. Albert, W. B. Atwood, L. Baldini, J. Ballet, G. Barbiellini, D. Bastieri, J. Becerra Gonzalez, R. Bellazzini, E. Bissaldi, R. D. Blandford, E. D. Bloom, R. Bonino, E. Bottacini,

J. Bregeon, P. Bruel, R. Buehler, S. Buson, G. A. Caliandro, R. A. Cameron, R. Caputo, M. Caragiulo, P. A. Caraveo, E. Cavazzuti, C. Cecchi, A. Chekhtman, J. Chiang, G. Chiaro, S. Ciprini, J. Cohen-Tanugi, J. Conrad, S. Cutini, F. D'Ammando, A. de Angelis, F. de Palma, R. Desiante, L. Di Venere, A. Domínguez, P. S. Drell, C. Favuzzi, S. J. Fegan, E. C. Ferrara, W. B. Focke, L. Fuhrmann, Y. Fukazawa, P. Fusco, F. Gargano, D. Gasparrini, N. Giglietto, P. Giommi, F. Giordano, M. Giroletti, G. Godfrey, D. Green, I. A. Grenier, J. E. Grove, S. Guiriec, A. K. Harding, E. Hays, J. W. Hewitt, A. B. Hill, D. Horan, T. Jogler, G. Jóhannesson, A. S. Johnson, T. Kamae, M. Kuss, S. Larsson, L. Latronico, J. Li, L. Li, F. Longo, F. Loparco, B. Lott, M. N. Lovellette, P. Lubrano, J. Magill, S. Maldera, A. Manfreda, W. Max-Moerbeck, M. Mayer, M. N. Mazziotta, J. E. McEnery, P. F. Michelson, T. Mizuno, M. E. Monzani, A. Morselli, I. V. Moskalenko, S. Murgia, E. Nuss, M. Ohno, T. Ohsugi, R. Ojha, N. Omodei, E. Orlando, J. F. Ormes, D. Paneque, T. J. Pearson, J. S. Perkins, M. Perri, M. Pesce-Rollins, V. Petrosian, F. Piron, G. Pivato, T. A. Porter, S. Rainò, R. Rando, M. Razzano, A. Readhead, A. Reimer, O. Reimer, A. Schulz, C. Sgrò, E. J. Siskind, F. Spada, G. Spandre, P. Spinelli, D. J. Suson, H. Takahashi, J. B. Thayer, D. J. Thompson, L. Tibaldo, D. F. Torres, G. Tosti, E. Troja, Y. Uchiyama, G. Vianello, K. S. Wood, M. Wood, S. Zimmer, A. Berdyugin, R. H. D. Corbet, T. Hovatta, E. Lindfors, K. Nilsson, R. Reinthal, A. Sillanpää, A. Stamerra, L. O. Takalo, and M. J. Valtonen.

Multiwavelength Evidence for Quasi-periodic Modulation in the Gamma-Ray Blazar PG 1553+113.

ApJL, 813(2):L41, November 2015.

[8] M. Ackermann, M. Ajello, A. Allafort, E. Antolini, L. Baldini, J. Ballet, G. Barbiellini, D. Bastieri, R. Bellazzini, B. Berenji, R. D. Blandford, E. D. Bloom, E. Bonamente, A. W. Borgland, A. Bouvier, T. J. Brandt, J. Bregeon, M. Brigida, P. Bruel, R. Buehler, T. H. Burnett, S. Buson, G. A. Caliandro, R. A. Cameron, P. A. Caraveo, J. M. Casandjian, E. Cavazzuti, C. Cecchi, Ö. Çelik, E. Charles, A. Chekhtman, A. W. Chen, C. C. Cheung, J. Chiang, S. Ciprini, R. Claus, J. Cohen-Tanugi, J. Conrad, S. Cutini, A. de Angelis, M. E. DeCesar, A. De Luca, F. de Palma, C. D. Dermer, E. do Couto e. Silva, P. S. Drell, A. Drlica-

Wagner, R. Dubois, T. Enoto, C. Favuzzi, S. J. Fegan, E. C. Ferrara, W. B. Focke, P. Fortin, Y. Fukazawa, S. Funk, P. Fusco, F. Gargano, D. Gasparrini, N. Gehrels, S. Germani, N. Giglietto, F. Giordano, M. Giroletti, T. Glanzman, G. Godfrey, I. A. Grenier, M. H. Grondin, J. E. Grove, L. Guillemot, S. Guiriec, M. Gustafsson, D. Hadasch, Y. Hanabata, A. K. Harding, M. Hayashida, E. Hays, S. E. Healey, A. B. Hill, D. Horan, X. Hou, G. Jóhannesson, A. S. Johnson, T. J. Johnson, T. Kamae, H. Katagiri, J. Kataoka, M. Kerr, J. Knödlseder, M. Kuss, J. Lande, L. Latronico, S. H. Lee, M. Lemoine-Goumard, F. Longo, F. Loparco, B. Lott, M. N. Lovellette, P. Lubrano, G. M. Madejski, M. N. Mazziotta, J. E. McEnery, J. Mehault, P. F. Michelson, R. P. Mignani, W. Mitthumsiri, T. Mizuno, C. Monte, M. E. Monzani, A. Morselli, I. V. Moskalenko, S. Murgia, T. Nakamori, M. Naumann-Godo, P. L. Nolan, J. P. Norris, E. Nuss, T. Ohsugi, A. Okumura, N. Omodei, E. Orlando, J. F. Ormes, M. Ozaki, D. Paneque, J. H. Panetta, D. Parent, V. Pelassa, M. Pesce-Rollins, M. Pierbattista, F. Piron, G. Pivato, T. A. Porter, S. Rainò, R. Rando, P. S. Ray, M. Razzano, A. Reimer, O. Reimer, T. Reposeur, R. W. Romani, H. F. W. Sadrozinski, D. Salvetti, P. M. Saz Parkinson, T. L. Schalk, C. Sgrò, M. S. Shaw, E. J. Siskind, P. D. Smith, G. Spandre, P. Spinelli, D. J. Suson, H. Takahashi, T. Tanaka, J. G. Thayer, J. B. Thayer, D. J. Thompson, L. Tibaldo, O. Tibolla, D. F. Torres, G. Tosti, A. Tramacere, E. Troja, T. L. Usher, J. Vandenbroucke, V. Vasileiou, G. Vianello, N. Vilchez, V. Vitale, A. P. Waite, E. Wallace, P. Wang, B. L. Winer, M. T. Wolff, D. L. Wood, K. S. Wood, Z. Yang, and S. Zimmer.

A Statistical Approach to Recognizing Source Classes for Unassociated Sources in the First Fermi-LAT Catalog.

ApJ, 753(1):83, July 2012.

[9] M. Ackermann, M. Ajello, W. B. Atwood, L. Baldini, J. Ballet, G. Barbiellini, D. Bastieri, J. Becerra Gonzalez, R. Bellazzini, E. Bissaldi, R. D. Blandford, E. D. Bloom, R. Bonino, E. Bottacini, T. J. Brandt, J. Bregeon, R. J. Britto, P. Bruel, R. Buehler, S. Buson, G. A. Caliandro, R. A. Cameron, M. Caragiulo, P. A. Caraveo, B. Carpenter, J. M. Casandjian, E. Cavazzuti, C. Cecchi, E. Charles, A. Chekhtman, C. C. Cheung, J. Chiang, G. Chiaro, S. Ciprini, R. Claus, J. Cohen-Tanugi, L. R. Cominsky, J. Conrad, S. Cutini, R. D'Abrusco,

F. D'Ammando, A. de Angelis, R. Desiante, S. W. Digel, L. Di Venere, P. S. Drell, C. Favuzzi, S. J. Fegan, E. C. Ferrara, J. Finke, W. B. Focke, A. Franckowiak, L. Fuhrmann, Y. Fukazawa, A. K. Furniss, P. Fusco, F. Gargano, D. Gasparrini, N. Giglietto, P. Giommi, F. Giordano, M. Giroletti, T. Glanzman, G. Godfrey, I. A. Grenier, J. E. Grove, S. Guiriec, J. W. Hewitt, A. B. Hill, D. Horan, R. Itoh, G. Jóhannesson, A. S. Johnson, W. N. Johnson, J. Kataoka, T. Kawano, F. Krauss, M. Kuss, G. La Mura, S. Larsson, L. Latronico, C. Leto, J. Li, L. Li, F. Longo, F. Loparco, B. Lott, M. N. Lovellette, P. Lubrano, G. M. Madejski, M. Mayer, M. N. Mazziotta, J. E. McEnery, P. F. Michelson, T. Mizuno, A. A. Moiseev, M. E. Monzani, A. Morselli, I. V. Moskalenko, S. Murgia, E. Nuss, M. Ohno, T. Ohsugi, R. Ojha, N. Omodei, M. Orienti, E. Orlando, A. Paggi, D. Paneque, J. S. Perkins, M. Pesce-Rollins, F. Piron, G. Pivato, T. A. Porter, S. Rainò, R. Rando, M. Razzano, S. Razzaque, A. Reimer, O. Reimer, R. W. Romani, D. Salvetti, M. Schaal, F. K. Schinzel, A. Schulz, C. Sgrò, E. J. Siskind, K. V. Sokolovsky, F. Spada, G. Spandre, P. Spinelli, L. Stawarz, D. J. Suson, H. Takahashi, T. Takahashi, Y. Tanaka, J. G. Thayer, J. B. Thayer, L. Tibaldo, D. F. Torres, E. Torresi, G. Tosti, E. Troja, Y. Uchiyama, G. Vianello, B. L. Winer, K. S. Wood, and S. Zimmer.

The Third Catalog of Active Galactic Nuclei Detected by the Fermi Large Area Telescope.

ApJ, 810(1):14, September 2015.

[10] M. Ackermann, M. Ajello, L. Baldini, J. Ballet, G. Barbiellini, D. Bastieri, J. Becerra Gonzalez, R. Bellazzini, E. Bissaldi, R. D. Blandford, E. D. Bloom, R. Bonino, E. Bottacini, J. Bregeon, P. Bruel, R. Buehler, S. Buson, R. A. Cameron, M. Caragiulo, P. A. Caraveo, E. Cavazzuti, C. Cecchi, C. C. Cheung, J. Chiang, G. Chiaro, S. Ciprini, J. Conrad, D. Costantin, F. Costanza, S. Cutini, F. D'Ammando, F. de Palma, R. Desiante, S. W. Digel, N. Di Lalla, M. Di Mauro, L. Di Venere, A. Domínguez, P. S. Drell, C. Favuzzi, S. J. Fegan, E. C. Ferrara, J. Finke, W. B. Focke, Y. Fukazawa, S. Funk, P. Fusco, F. Gargano, D. Gasparrini, N. Giglietto, F. Giordano, M. Giroletti, D. Green, I. A. Grenier, L. Guillemot, S. Guiriec, D. H. Hartmann, E. Hays, D. Horan, T. Jogler, G. Jóhannesson, A. S. Johnson, M. Kuss, G. La Mura, S. Larsson, L. Latronico, J. Li, F. Longo, F. Loparco, M. N. Lovel-

lette, P. Lubrano, J. D. Magill, S. Maldera, A. Manfreda, L. Marcotulli, M. N. Mazziotta, P. F. Michelson, N. Mirabal, W. Mitthumsiri, T. Mizuno, M. E. Monzani, A. Morselli, I. V. Moskalenko, M. Negro, E. Nuss, T. Ohsugi, R. Ojha, N. Omodei, M. Orienti, E. Orlando, J. F. Ormes, V. S. Paliya, D. Paneque, J. S. Perkins, M. Persic, M. Pesce-Rollins, F. Piron, T. A. Porter, G. Principe, S. Rainò, R. Rando, B. Rani, M. Razzano, S. Razzaque, A. Reimer, O. Reimer, R. W. Romani, C. Sgrò, D. Simone, E. J. Siskind, F. Spada, G. Spandre, P. Spinelli, C. S. Stalin, L. Stawarz, D. J. Suson, M. Takahashi, K. Tanaka, J. B. Thayer, D. J. Thompson, D. F. Torres, E. Torresi, G. Tosti, E. Troja, G. Vianello, and K. S. Wood.
Gamma-Ray Blazars within the First 2 Billion Years.
ApJL, 837(1):L5, March 2017.

[11] M. Ackermann, R. Anantua, K. Asano, L. Baldini, G. Barbiellini, D. Bastieri, J. Becerra Gonzalez, R. Bellazzini, E. Bissaldi, R. D. Blandford, E. D. Bloom, R. Bonino, E. Bottacini, P. Bruel, R. Buehler, G. A. Caliandro, R. A. Cameron, M. Caragiulo, P. A. Caraveo, E. Cavazzuti, C. Cecchi, C. C. Cheung, J. Chiang, G. Chiaro, S. Ciprini, J. Cohen-Tanugi, F. Costanza, S. Cutini, F. D'Ammando, F. de Palma, R. Desiante, S. W. Digel, N. Di Lalla, M. Di Mauro, L. Di Venere, P. S. Drell, C. Favuzzi, S. J. Fegan, E. C. Ferrara, Y. Fukazawa, S. Funk, P. Fusco, F. Gargano, D. Gasparrini, N. Giglietto, F. Giordano, M. Giroletti, I. A. Grenier, L. Guillemot, S. Guiriec, M. Hayashida, E. Hays, D. Horan, G. Jóhannesson, S. Kensei, D. Kocevski, M. Kuss, G. La Mura, S. Larsson, L. Latronico, J. Li, F. Longo, F. Loparco, B. Lott, M. N. Lovellette, P. Lubrano, G. M. Madejski, J. D. Magill, S. Maldera, A. Manfreda, M. Mayer, M. N. Mazziotta, P. F. Michelson, N. Mirabal, T. Mizuno, M. E. Monzani, A. Morselli, I. V. Moskalenko, K. Nalewajko, M. Negro, E. Nuss, T. Ohsugi, E. Orlando, D. Paneque, J. S. Perkins, M. Pesce-Rollins, F. Piron, G. Pivato, T. A. Porter, G. Principe, R. Rando, M. Razzano, S. Razzaque, A. Reimer, J. D. Scargle, C. Sgrò, M. Sikora, D. Simone, E. J. Siskind, F. Spada, P. Spinelli, L. Stawarz, J. B. Thayer, D. J. Thompson, D. F. Torres, E. Troja, Y. Uchiyama, Y. Yuan, and S. Zimmer.
Minute-timescale ¿100 MeV γ-Ray Variability during the Giant Outburst of Quasar 3C 279 Observed by Fermi-LAT in 2015 June.
ApJL, 824(2):L20, June 2016.

[12] F. Ait Benkhali, W. Hofmann, F. M. Rieger, and N. Chakraborty.
Evaluating quasi-periodic variations in the γ-ray light curves of Fermi-LAT blazars.
A&A, 634:A120, February 2020.

[13] M. Ajello, R. Angioni, M. Axelsson, J. Ballet, G. Barbiellini, D. Bastieri, J. Becerra Gonzalez, R. Bellazzini, E. Bissaldi, E. D. Bloom, R. Bonino, E. Bottacini, P. Bruel, S. Buson, F. Cafardo, R. A. Cameron, E. Cavazzuti, S. Chen, C. C. Cheung, S. Ciprini, D. Costantin, S. Cutini, F. D'Ammando, P. de la Torre Luque, R. de Menezes, F. de Palma, A. Desai, N. Di Lalla, L. Di Venere, A. Domínguez, F. Fana Dirirsa, E. C. Ferrara, J. Finke, A. Franckowiak, Y. Fukazawa, S. Funk, P. Fusco, F. Gargano, S. Garrappa, D. Gasparrini, N. Giglietto, F. Giordano, M. Giroletti, D. Green, I. A. Grenier, S. Guiriec, S. Harita, E. Hays, D. Horan, R. Itoh, G. Jóhannesson, M. Kovac'evic', F. Krauss, M. Kreter, M. Kuss, S. Larsson, C. Leto, J. Li, I. Liodakis, F. Longo, F. Loparco, B. Lott, M. N. Lovellette, P. Lubrano, G. M. Madejski, S. Maldera, A. Manfreda, G. Martí-Devesa, F. Massaro, M. N. Mazziotta, I. Mereu, M. Meyer, G. Migliori, N. Mirabal, T. Mizuno, M. E. Monzani, A. Morselli, I. V. Moskalenko, M. Negro, R. Nemmen, E. Nuss, L. S. Ojha, R. Ojha, N. Omodei, M. Orienti, E. Orlando, J. F. Ormes, V. S. Paliya, Z. Pei, H. Peña-Herazo, M. Persic, M. Pesce-Rollins, L. Petrov, F. Piron, H. Poon, G. Principe, S. Rainò, R. Rando, B. Rani, M. Razzano, S. Razzaque, A. Reimer, O. Reimer, F. K. Schinzel, D. Serini, C. Sgrò, E. J. Siskind, G. Spandre, P. Spinelli, D. J. Suson, Y. Tachibana, D. J. Thompson, D. F. Torres, E. Torresi, E. Troja, J. Valverde, P. van Zyl, and M. Yassine.
The Fourth Catalog of Active Galactic Nuclei Detected by the Fermi Large Area Telescope.
ApJ, 892(2):105, April 2020.

[14] M. Ajello, R. Angioni, M. Axelsson, J. Ballet, G. Barbiellini, D. Bastieri, J. Becerra Gonzalez, R. Bellazzini, E. Bissaldi, E. D. Bloom, R. Bonino, E. Bottacini, P. Bruel, S. Buson, F. Cafardo, R. A. Cameron, E. Cavazzuti, S. Chen, C. C. Cheung, S. Ciprini, D. Costantin, S. Cutini, F. D'Ammando, P. de la Torre Luque, R. de Menezes, F. de Palma, A. Desai, N. Di Lalla, L. Di Venere, A. Domínguez,

F. Fana Dirirsa, E. C. Ferrara, J. Finke, A. Franckowiak, Y. Fukazawa, S. Funk, P. Fusco, F. Gargano, S. Garrappa, D. Gasparrini, N. Giglietto, F. Giordano, M. Giroletti, D. Green, I. A. Grenier, S. Guiriec, S. Harita, E. Hays, D. Horan, R. Itoh, G. Jóhannesson, M. Kovac'evic', F. Krauss, M. Kreter, M. Kuss, S. Larsson, C. Leto, J. Li, I. Liodakis, F. Longo, F. Loparco, B. Lott, M. N. Lovellette, P. Lubrano, G. M. Madejski, S. Maldera, A. Manfreda, G. Martí-Devesa, F. Massaro, M. N. Mazziotta, I. Mereu, M. Meyer, G. Migliori, N. Mirabal, T. Mizuno, M. E. Monzani, A. Morselli, I. V. Moskalenko, M. Negro, R. Nemmen, E. Nuss, L. S. Ojha, R. Ojha, N. Omodei, M. Orienti, E. Orlando, J. F. Ormes, V. S. Paliya, Z. Pei, H. Peña-Herazo, M. Persic, M. Pesce-Rollins, L. Petrov, F. Piron, H. Poon, G. Principe, S. Rainò, R. Rando, B. Rani, M. Razzano, S. Razzaque, A. Reimer, O. Reimer, F. K. Schinzel, D. Serini, C. Sgrò, E. J. Siskind, G. Spandre, P. Spinelli, D. J. Suson, Y. Tachibana, D. J. Thompson, D. F. Torres, E. Torresi, E. Troja, J. Valverde, P. van Zyl, and M. Yassine.
The Fourth Catalog of Active Galactic Nuclei Detected by the Fermi Large Area Telescope.
ApJ, 892(2):105, April 2020.

[15] M. Ajello, L. Baldini, J. Ballet, D. Bastieri, J. Becerra Gonzalez, R. Bellazzini, A. Berretta, E. Bissaldi, R. Bonino, A. Brill, P. Bruel, S. Buson, R. Caputo, P. A. Caraveo, C. C. Cheung, G. Chiaro, N. Cibrario, S. Ciprini, M. Crnogorcevic, S. Cutini, F. D'Ammando, S. De Gaetano, N. Di Lalla, L. Di Venere, A. Domínguez, V. Fallah Ramazani, E. C. Ferrara, A. Fiori, Y. Fukazawa, S. Funk, P. Fusco, V. Gammaldi, F. Gargano, S. Garrappa, D. Gasparrini, N. Giglietto, F. Giordano, M. Giroletti, D. Green, I. A. Grenier, S. Guiriec, D. Horan, X. Hou, T. Kayanoki, M. Kuss, S. Larsson, L. Latronico, T. Lewis, J. Li, I. Liodakis, F. Longo, F. Loparco, B. Lott, M. N. Lovellette, P. Lubrano, G. M. Madejski, S. Maldera, A. Manfreda, G. Martí-Devesa, M. N. Mazziotta, I. Mereu, P. F. Michelson, N. Mirabal, W. Mitthumsiri, T. Mizuno, M. E. Monzani, A. Morselli, I. V. Moskalenko, M. Negro, R. Ojha, M. Orienti, E. Orlando, J. F. Ormes, Z. Pei, H. Peña-Herazo, M. Persic, M. Pesce-Rollins, V. Petrosian, R. Pillera, H. Poon, T. A. Porter, G. Principe, S. Rainò, R. Rando, B. Rani, M. Razzano, S. Razzaque, A. Reimer, O. Reimer, L. Scotton, D. Serini, C. Sgrò, E. J.

Siskind, G. Spandre, P. Spinelli, D. J. Suson, H. Tajima, D. F. Torres, J. Valverde, H. Yassin, and G. Zaharijas.
The Fourth Catalog of Active Galactic Nuclei Detected by the Fermi Large Area Telescope: Data Release 3.
ApJSS, 263(2):24, December 2022.

[16] J. Aleksić, S. Ansoldi, L. A. Antonelli, P. Antoranz, A. Babic, P. Bangale, J. A. Barrio, J. Becerra González, W. Bednarek, E. Bernardini, B. Biasuzzi, A. Biland, O. Blanch, S. Bonnefoy, G. Bonnoli, F. Borracci, T. Bretz, E. Carmona, A. Carosi, P. Colin, E. Colombo, J. L. Contreras, J. Cortina, S. Covino, P. Da Vela, F. Dazzi, A. De Angelis, G. De Caneva, B. De Lotto, E. de Oña Wilhelmi, C. Delgado Mendez, D. Dominis Prester, D. Dorner, M. Doro, S. Einecke, D. Eisenacher, D. Elsaesser, M. V. Fonseca, L. Font, K. Frantzen, C. Fruck, D. Galindo, R. J. García López, M. Garczarczyk, D. Garrido Terrats, M. Gaug, N. Godinović, A. González Muñoz, S. R. Gozzini, D. Hadasch, Y. Hanabata, M. Hayashida, J. Herrera, D. Hildebrand, J. Hose, D. Hrupec, W. Idec, V. Kadenius, H. Kellermann, K. Kodani, Y. Konno, J. Krause, H. Kubo, J. Kushida, A. La Barbera, D. Lelas, N. Lewandowska, E. Lindfors, S. Lombardi, F. Longo, M. López, R. López-Coto, A. López-Oramas, E. Lorenz, I. Lozano, M. Makariev, K. Mallot, G. Maneva, N. Mankuzhiyil, K. Mannheim, L. Maraschi, B. Marcote, M. Mariotti, M. Martínez, D. Mazin, U. Menzel, J. M. Miranda, R. Mirzoyan, A. Moralejo, P. Munar-Adrover, D. Nakajima, A. Niedzwiecki, K. Nilsson, K. Nishijima, K. Noda, R. Orito, A. Overkemping, S. Paiano, M. Palatiello, D. Paneque, R. Paoletti, J. M. Paredes, X. Paredes-Fortuny, M. Persic, J. Poutanen, P. G. Prada Moroni, E. Prandini, I. Puljak, R. Reinthal, W. Rhode, M. Ribó, J. Rico, J. Rodriguez Garcia, S. Rügamer, T. Saito, K. Saito, K. Satalecka, V. Scalzotto, V. Scapin, C. Schultz, T. Schweizer, S. N. Shore, A. Sillanpää, J. Sitarek, I. Snidaric, D. Sobczynska, F. Spanier, V. Stamatescu, A. Stamerra, T. Steinbring, J. Storz, M. Strzys, L. Takalo, H. Takami, F. Tavecchio, P. Temnikov, T. Terzić, D. Tescaro, M. Teshima, J. Thaele, O. Tibolla, D. F. Torres, T. Toyama, A. Treves, M. Uellenbeck, P. Vogler, R. Zanin, M. Kadler, R. Schulz, E. Ros, U. Bach, F. Krauß, and J. Wilms.
Black hole lightning due to particle acceleration at subhorizon scales.

Science, 346(6213):1080–1084, November 2014.

[17] W. N. Alston, M. L. Parker, J. Markevičiūtė, A. C. Fabian, M. Middleton, A. Lohfink, E. Kara, and C. Pinto.
Discovery of an ∼2-h high-frequency X-ray QPO and iron Kα reverberation in the active galaxy MS 2254.9-3712.
MNRAS, 449(1):467–476, May 2015.

[18] R. Angioni.
Fermi-LAT detection of renewed gamma-ray activity from the high-redshift FSRQ PKS 0537-286.
The Astronomer's Telegram, 14285:1, December 2020.

[19] T. Arlen, T. Aune, M. Beilicke, W. Benbow, A. Bouvier, J. H. Buckley, V. Bugaev, A. Cesarini, L. Ciupik, M. P. Connolly, W. Cui, R. Dickherber, J. Dumm, M. Errando, A. Falcone, S. Federici, Q. Feng, J. P. Finley, G. Finnegan, L. Fortson, A. Furniss, N. Galante, D. Gall, S. Griffin, J. Grube, G. Gyuk, D. Hanna, J. Holder, T. B. Humensky, P. Kaaret, N. Karlsson, M. Kertzman, Y. Khassen, D. Kieda, H. Krawczynski, F. Krennrich, G. Maier, P. Moriarty, R. Mukherjee, T. Nelson, A. O'Faoláin de Bhróithe, R. A. Ong, M. Orr, N. Park, J. S. Perkins, A. Pichel, M. Pohl, H. Prokoph, J. Quinn, K. Ragan, L. C. Reyes, P. T. Reynolds, E. Roache, D. B. Saxon, M. Schroedter, G. H. Sembroski, D. Staszak, I. Telezhinsky, G. Tešić, M. Theiling, K. Tsurusaki, A. Varlotta, S. Vincent, S. P. Wakely, T. C. Weekes, A. Weinstein, R. Welsing, D. A. Williams, B. Zitzer, VERITAS Collaboration, S. G. Jorstad, N. R. MacDonald, A. P. Marscher, P. S. Smith, R. C. Walker, T. Hovatta, J. Richards, W. Max-Moerbeck, A. Readhead, M. L. Lister, Y. Y. Kovalev, A. B. Pushkarev, M. A. Gurwell, A. Lähteenmäki, E. Nieppola, M. Tornikoski, and E. Järvelä.
Rapid TeV Gamma-Ray Flaring of BL Lacertae.
ApJ, 762(2):92, January 2013.

[20] K. A. Arnaud.
XSPEC: The First Ten Years.
In George H. Jacoby and Jeannette Barnes, editors, *Astronomical Data Analysis Software and Systems V*, volume 101 of *Astronomical Society of the Pacific Conference Series*, page 17, January 1996.

[21] B. Arsioli and P. Dedin.
Machine learning applied to multifrequency data in astrophysics: blazar classification.
MNRAS, 498(2):1750–1764, October 2020.

[22] W. B. Atwood, A. A. Abdo, M. Ackermann, W. Althouse, B. Anderson, M. Axelsson, L. Baldini, J. Ballet, D. L. Band, G. Barbiellini, J. Bartelt, D. Bastieri, B. M. Baughman, K. Bechtol, D. Bédérède, F. Bellardi, R. Bellazzini, B. Berenji, G. F. Bignami, D. Bisello, E. Bissaldi, R. D. Blandford, E. D. Bloom, J. R. Bogart, E. Bonamente, J. Bonnell, A. W. Borgland, A. Bouvier, J. Bregeon, A. Brez, M. Brigida, P. Bruel, T. H. Burnett, G. Busetto, G. A. Caliandro, R. A. Cameron, P. A. Caraveo, S. Carius, P. Carlson, J. M. Casandjian, E. Cavazzuti, M. Ceccanti, C. Cecchi, E. Charles, A. Chekhtman, C. C. Cheung, J. Chiang, R. Chipaux, A. N. Cillis, S. Ciprini, R. Claus, J. Cohen-Tanugi, S. Condamoor, J. Conrad, R. Corbet, L. Corucci, L. Costamante, S. Cutini, D. S. Davis, D. Decotigny, M. DeKlotz, C. D. Dermer, A. de Angelis, S. W. Digel, E. do Couto e Silva, P. S. Drell, R. Dubois, D. Dumora, Y. Edmonds, D. Fabiani, C. Farnier, C. Favuzzi, D. L. Flath, P. Fleury, W. B. Focke, S. Funk, P. Fusco, F. Gargano, D. Gasparrini, N. Gehrels, F. X. Gentit, S. Germani, B. Giebels, N. Giglietto, P. Giommi, F. Giordano, T. Glanzman, G. Godfrey, I. A. Grenier, M. H. Grondin, J. E. Grove, L. Guillemot, S. Guiriec, G. Haller, A. K. Harding, P. A. Hart, E. Hays, S. E. Healey, M. Hirayama, L. Hjalmarsdotter, R. Horn, R. E. Hughes, G. Jóhannesson, G. Johansson, A. S. Johnson, R. P. Johnson, T. J. Johnson, W. N. Johnson, T. Kamae, H. Katagiri, J. Kataoka, A. Kavelaars, N. Kawai, H. Kelly, M. Kerr, W. Klamra, J. Knödlseder, M. L. Kocian, N. Komin, F. Kuehn, M. Kuss, D. Landriu, L. Latronico, B. Lee, S. H. Lee, M. Lemoine-Goumard, A. M. Lionetto, F. Longo, F. Loparco, B. Lott, M. N. Lovellette, P. Lubrano, G. M. Madejski, A. Makeev, B. Marangelli, M. M. Massai, M. N. Mazziotta, J. E. McEnery, N. Menon, C. Meurer, P. F. Michelson, M. Minuti, N. Mirizzi, W. Mitthumsiri, T. Mizuno, A. A. Moiseev, C. Monte, M. E. Monzani, E. Moretti, A. Morselli, I. V. Moskalenko, S. Murgia, T. Nakamori, S. Nishino, P. L. Nolan, J. P. Norris, E. Nuss, M. Ohno, T. Ohsugi, N. Omodei, E. Orlando, J. F. Ormes, A. Paccagnella, D. Paneque, J. H. Panetta, D. Parent, M. Pearce, M. Pepe, A. Perazzo, M. Pesce-Rollins, P. Picozza,

L. Pieri, M. Pinchera, F. Piron, T. A. Porter, L. Poupard, S. Rainò, R. Rando, E. Rapposelli, M. Razzano, A. Reimer, O. Reimer, T. Reposeur, L. C. Reyes, S. Ritz, L. S. Rochester, A. Y. Rodriguez, R. W. Romani, M. Roth, J. J. Russell, F. Ryde, S. Sabatini, H. F. W. Sadrozinski, D. Sanchez, A. Sander, L. Sapozhnikov, P. M. Saz Parkinson, J. D. Scargle, T. L. Schalk, G. Scolieri, C. Sgrò, G. H. Share, M. Shaw, T. Shimokawabe, C. Shrader, A. Sierpowska-Bartosik, E. J. Siskind, D. A. Smith, P. D. Smith, G. Spandre, P. Spinelli, J. L. Starck, T. E. Stephens, M. S. Strickman, A. W. Strong, D. J. Suson, H. Tajima, H. Takahashi, T. Takahashi, T. Tanaka, A. Tenze, S. Tether, J. B. Thayer, J. G. Thayer, D. J. Thompson, L. Tibaldo, O. Tibolla, D. F. Torres, G. Tosti, A. Tramacere, M. Turri, T. L. Usher, N. Vilchez, V. Vitale, P. Wang, K. Watters, B. L. Winer, K. S. Wood, T. Ylinen, and M. Ziegler.
The Large Area Telescope on the Fermi Gamma-Ray Space Telescope Mission.
ApJ, 697(2):1071–1102, June 2009.

[23] F. Auchère, C. Froment, K. Bocchialini, E. Buchlin, and J. Solomon.
On the Fourier and Wavelet Analysis of Coronal Time Series.
ApJ, 825(2):110, July 2016.

[24] T. Auld, M. Bridges, M. P. Hobson, and S. F. Gull.
Fast cosmological parameter estimation using neural networks.
Monthly Notices of the Royal Astronomical Society: Letters, 376(1):L11–L15, 03 2007.

[25] V. Baghmanyan, S. Gasparyan, and N. Sahakyan.
Rapid Gamma-Ray Variability of NGC 1275.
ApJ, 848(2):111, October 2017.

[26] M. C. Begelman, R. D. Blandford, and M. J. Rees.
Massive black hole binaries in active galactic nuclei.
Nature, 287(5780):307–309, September 1980.

[27] A. Bhat and D. Malyshev.
Machine learning methods for constructing probabilistic Fermi-LAT catalogs.
A&A, 660:A87, April 2022.

[28] Gopal Bhatta.
Blazar Mrk 501 shows rhythmic oscillations in its γ-ray emission.
MNRAS, 487(3):3990–3997, August 2019.

[29] Gopal Bhatta and Niraj Dhital.
The Nature of γ-Ray Variability in Blazars.
ApJ, 891(2):120, March 2020.

[30] C.M. Bishop.
Neural networks for pattern recognition.
Oxford University Press, USA, 1995.

[31] J. Biteau, E. Prandini, L. Costamante, M. Lemoine, P. Padovani, E. Pueschel, E. Resconi, F. Tavecchio, A. Taylor, and A. Zech.
Progress in unveiling extreme particle acceleration in persistent astrophysical jets.
Nature Astronomy, 4:124–131, February 2020.

[32] Roger Blandford, David Meier, and Anthony Readhead.
Relativistic Jets from Active Galactic Nuclei.
Annual Review of Astronomy and Astrophysics, 57:467–509, August 2019.

[33] M. Błażejowski, M. Sikora, R. Moderski, and G. M. Madejski.
Comptonization of Infrared Radiation from Hot Dust by Relativistic Jets in Quasars.
ApJ, 545(1):107–116, December 2000.

[34] Steven D. Bloom and Alan P. Marscher.
An Analysis of the Synchrotron Self-Compton Model for the Multi–Wave Band Spectra of Blazars.
ApJ, 461:657, April 1996.

[35] E. Bottacini, M. Ajello, J. Greiner, E. Pian, A. Rau, E. Palazzi, S. Covino, G. Ghisellini, T. Krühler, A. Küpcü Yoldaş, N. Cappelluti, and P. Afonso.
PKS 0537-286, carrying the information of the environment of SMBHs in the early Universe.
A&A, 509:A69, January 2010.

[36] M. Böttcher, A. Reimer, K. Sweeney, and A. Prakash.

Leptonic and Hadronic Modeling of Fermi-detected Blazars.
ApJ, 768:54, May 2013.

[37] Richard J. Britto, Eugenio Bottacini, Benoît Lott, Soebur Razzaque, and Sara Buson.
Fermi-LAT Observations of the 2014 May-July Outburst from 3C 454.3.
ApJ, 830(2):162, October 2016.

[38] Anja Butter, Thorben Finke, Felicitas Keil, Michael Krämer, and Silvia Manconi.
Classification of Fermi-LAT blazars with Bayesian neural networks.
JCAP, 2022(4):023, April 2022.

[39] M. Cappi, M. Matsuoka, A. Comastri, W. Brinkmann, M. Elvis, G. G. C. Palumbo, and C. Vignali.
ASCA and ROSAT X-Ray Spectra of High-Redshift Radio-loud Quasars.
ApJ, 478(2):492–510, March 1997.

[40] W. Cash.
Parameter estimation in astronomy through application of the likelihood ratio.
ApJ, 228:939–947, March 1979.

[41] M. Cerruti, A. Zech, C. Boisson, G. Emery, S. Inoue, and J.-P. Lenain.
Leptohadronic single-zone models for the electromagnetic and neutrino emission of TXS 0506+056.
MNRAS, 483:L12–L16, February 2019.

[42] Matteo Cerruti.
Leptonic and Hadronic Radiative Processes in Supermassive-Black-Hole Jets.
Galaxies, 8(4):72, October 2020.

[43] Y. L. Chang, C. H. Brandt, and P. Giommi.
The Open Universe VOU-Blazars tool.
Astronomy and Computing, 30:100350, January 2020.

[44] Tianqi Chen and Carlos Guestrin.
XGBoost: A Scalable Tree Boosting System.
arXiv e-prints, page arXiv:1603.02754, March 2016.

[45] C. C. Cheung.
Fermi LAT detection of a GeV flare from High-redshift Blazar PKS 0537-286.
The Astronomer's Telegram, 10356:1, May 2017.

[46] G. Chiaro, D. Salvetti, G. La Mura, M. Giroletti, D. J. Thompson, and D. Bastieri.
Blazar flaring patterns (B-FlaP) classifying blazar candidate of uncertain type in the third Fermi-LAT catalogue by artificial neural networks.
MNRAS, 462(3):3180–3195, November 2016.

[47] Graziano Chiaro, Milos Kovacevic, and Giovanni La Mura.
4FGLzoo. Classifying Fermi-LAT uncertain gamma-ray sources by machine learning analysis.
Journal of High Energy Astrophysics, 29:40–42, March 2021.

[48] S D Connolly.
A Python Code for the Emmanoulopoulos et al. [arXiv:1305.0304] Light Curve Simulation Algorithm.
arXiv e-prints, page arXiv:1503.06676, March 2015.

[49] Javier Coronado-Blázquez.
Classification of Fermi-LAT unidentified gamma-ray sources using CATBOOST gradient boosting decision trees.
MNRAS, 515(2):1807–1814, September 2022.

[50] L. Costamante, G. Ghisellini, P. Giommi, G. Tagliaferri, A. Celotti, M. Chiaberge, G. Fossati, L. Maraschi, F. Tavecchio, A. Treves, and A. Wolter.
Extreme synchrotron BL Lac objects. Stretching the blazar sequence.
A&A, 371:512–526, May 2001.

[51] S. Covino, A. Sandrinelli, and A. Treves.
Gamma-ray quasi-periodicities of blazars. A cautious approach.
MNRAS, 482(1):1270–1274, January 2019.

[52] Stefano Covino, Marco Landoni, Angela Sandrinelli, and Aldo Treves.
Looking at Blazar Light-curve Periodicities with Gaussian Processes.
ApJ, 895(2):122, June 2020.

[53] C. D. Dermer, R. Schlickeiser, and A. Mastichiadis.
High-energy gamma radiation from extragalactic radio sources.
A&A, 256:L27–L30, March 1992.

[54] Charles D. Dermer and Reinhard Schlickeiser.
On the Location of the Acceleration and Emission Sites in Gamma-Ray Blazars.
ApJSS, 90:945, February 1994.

[55] Sander Dieleman, Kyle W. Willett, and Joni Dambre.
Rotation-invariant convolutional neural networks for galaxy morphology prediction.
Monthly Notices of the Royal Astronomical Society, 450(2):1441–1459, 04 2015.

[56] Alina-C. Donea and R. J. Protheroe.
Radiation fields of disk, BLR and torus in quasars and blazars: implications for /γ-ray absorption.
Astroparticle Physics, 18(4):377–393, January 2003.

[57] D. Emmanoulopoulos, I. M. McHardy, and I. E. Papadakis.
Generating artificial light curves: revisited and updated.
MNRAS, 433(2):907–927, August 2013.

[58] Thorben Finke, Michael Krämer, and Silvia Manconi.
Classification of Fermi-LAT sources with deep learning using energy and time spectra.
MNRAS, 507(3):4061–4073, November 2021.

[59] Fabrizio Fiore, Martin Elvis, Paolo Giommi, and Paolo Padovani.
X-Ray Spectral Survey of WGACAT Quasars. I. Spectral Evolution and Low-Energy Cutoffs.
ApJ, 492(1):79–90, January 1998.

[60] Bernardo M. O. Fraga, Ulisses Barres de Almeida, Clécio R. Bom, Carlos H. Brandt, Paolo Giommi, Patrick Schubert, and Márcio P. de Albuquerque.
Deep learning Blazar classification based on multifrequency spectral energy distribution data.
MNRAS, 505(1):1268–1279, July 2021.

[61] A. Franceschini, G. Rodighiero, and M. Vaccari.
Extragalactic optical-infrared background radiation, its time evolution and the cosmic photon-photon opacity.
A&A, 487(3):837–852, September 2008.

[62] S. Gao, A. Fedynitch, W. Winter, and M. Pohl.
Modelling the coincident observation of a high-energy neutrino and a bright blazar flare.
Nature Astronomy, 3:88–92, January 2019.

[63] S. Gasparyan, D. Bégué, and N. Sahakyan.
Time-dependent lepto-hadronic modelling of the emission from blazar jets with SOPRANO: the case of TXS 0506 + 056, 3HSP J095507.9 + 355101, and 3C 279.
MNRAS, 509(2):2102–2121, January 2022.

[64] S. Gasparyan, N. Sahakyan, V. Baghmanyan, and D. Zargaryan.
On the Multiwavelength Emission from CTA 102.
ApJ, 863(2):114, August 2018.

[65] N. Gehrels, G. Chincarini, P. Giommi, K. O. Mason, J. A. Nousek, A. A. Wells, N. E. White, S. D. Barthelmy, D. N. Burrows, L. R. Cominsky, K. C. Hurley, F. E. Marshall, P. Mészáros, P. W. A. Roming, L. Angelini, L. M. Barbier, T. Belloni, S. Campana, P. A. Caraveo, M. M. Chester, O. Citterio, T. L. Cline, M. S. Cropper, J. R. Cummings, A. J. Dean, E. D. Feigelson, E. E. Fenimore, D. A. Frail, A. S. Fruchter, G. P. Garmire, K. Gendreau, G. Ghisellini, J. Greiner, J. E. Hill, S. D. Hunsberger, H. A. Krimm, S. R. Kulkarni, P. Kumar, F. Lebrun, N. M. Lloyd-Ronning, C. B. Markwardt, B. J. Mattson, R. F. Mushotzky, J. P. Norris, J. Osborne, B. Paczynski, D. M. Palmer, H. S. Park, A. M. Parsons, J. Paul, M. J. Rees, C. S. Reynolds, J. E. Rhoads, T. P. Sasseen, B. E. Schaefer, A. T. Short, A. P. Smale, I. A. Smith, L. Stella, G. Tagliaferri, T. Takahashi, M. Tashiro, L. K. Townsley, J. Tueller, M. J. L. Turner, M. Vietri, W. Voges, M. J. Ward, R. Willingale, F. M. Zerbi, and W. W. Zhang.
The Swift Gamma-Ray Burst Mission.
ApJ, 611(2):1005–1020, August 2004.

[66] S. Germani, G. Tosti, P. Lubrano, S. Cutini, I. Mereu, and A. Berretta.

Artificial Neural Network classification of 4FGL sources.
MNRAS, 505(4):5853–5861, August 2021.

[67] G. Ghisellini, R. Della Ceca, M. Volonteri, G. Ghirlanda, F. Tavecchio, L. Foschini, G. Tagliaferri, F. Haardt, G. Pareschi, and J. Grindlay.
Chasing the heaviest black holes of jetted active galactic nuclei.
MNRAS, 405(1):387–400, June 2010.

[68] G. Ghisellini, L. Foschini, M. Volonteri, G. Ghirlanda, F. Haardt, D. Burlon, and F. Tavecchio.
The blazar S5 0014+813: a real or apparent monster?
MNRAS, 399(1):L24–L28, October 2009.

[69] G. Ghisellini, L. Maraschi, and A. Treves.
Inhomogeneous synchrotron-self-compton models and the problem of relativistic beaming of BL Lac objects.
A&A, 146:204–212, May 1985.

[70] G. Ghisellini, G. Tagliaferri, L. Foschini, G. Ghirlanda, F. Tavecchio, R. Della Ceca, F. Haardt, M. Volonteri, and N. Gehrels.
High-redshift Fermi blazars.
MNRAS, 411(2):901–914, February 2011.

[71] G. Ghisellini and F. Tavecchio.
Fermi/LAT broad emission line blazars.
MNRAS, 448(2):1060–1077, April 2015.

[72] Marek Gierliński, Matthew Middleton, Martin Ward, and Chris Done.
A periodicity of ~1hour in X-ray emission from the active galaxy RE J1034+396.
Nature, 455(7211):369–371, September 2008.

[73] P Giommi, M T Menna, and P Padovani.
The Sedentary Multi-Frequency Survey . I . arXiv : astro-ph / 9907014v1 1 Jul 1999.
MNRAS, 310:465–475, 1999.

[74] Paolo Giommi, M. Perri, M. Capalbi, V. D'Elia, U. Barres de Almeida, C. H. Brandt, A. M. T. Pollock, F. Arneodo, A. Di Giovanni, Y. L.

Chang, O. Civitarese, M. De Angelis, C. Leto, F. Verrecchia, N. Ricard, S. Di Pippo, R. Middei, A. V. Penacchioni, R. Ruffini, N. Sahakyan, D. Israyelyan, and S. Turriziani.
X-ray spectra, light curves and SEDs of blazars frequently observed by Swift.
MNRAS, 507(4):5690–5702, November 2021.

[75] Theo Glauch, Tobias Kerscher, and Paolo Giommi.
BlaST – A Machine-Learning Estimator for the Synchrotron Peak of Blazars.
arXiv e-prints, page arXiv:2207.03813, July 2022.

[76] Anneya Golob, Marcin Sawicki, Andy D. Goulding, and Jean Coupon.
Classifying stars, galaxies, and AGNs in CLAUDS + HSC-SSP using gradient boosted decision trees.
MNRAS, 503(3):4136–4146, May 2021.

[77] Alok C. Gupta, Ashutosh Tripathi, Paul J. Wiita, Pankaj Kushwaha, Zhongli Zhang, and Cosimo Bambi.
Detection of a quasi-periodic oscillation in γ-ray light curve of the high-redshift blazar B2 1520+31.
MNRAS, 484(4):5785–5790, April 2019.

[78] Fiona A. Harrison, William W. Craig, Finn E. Christensen, Charles J. Hailey, William W. Zhang, Steven E. Boggs, Daniel Stern, W. Rick Cook, Karl Forster, Paolo Giommi, Brian W. Grefenstette, Yunjin Kim, Takao Kitaguchi, Jason E. Koglin, Kristin K. Madsen, Peter H. Mao, Hiromasa Miyasaka, Kaya Mori, Matteo Perri, Michael J. Pivovaroff, Simonetta Puccetti, Vikram R. Rana, Niels J. Westergaard, Jason Willis, Andreas Zoglauer, Hongjun An, Matteo Bachetti, Nicolas M. Barrière, Eric C. Bellm, Varun Bhalerao, Nicolai F. Brejnholt, Felix Fuerst, Carl C. Liebe, Craig B. Markwardt, Melania Nynka, Julia K. Vogel, Dominic J. Walton, Daniel R. Wik, David M. Alexander, Lynn R. Cominsky, Ann E. Hornschemeier, Allan Hornstrup, Victoria M. Kaspi, Greg M. Madejski, Giorgio Matt, Silvano Molendi, David M. Smith, John A. Tomsick, Marco Ajello, David R. Ballantyne, Mislav Baloković, Didier Barret, Franz E. Bauer, Roger D. Blandford, W. Niel Brandt, Laura W. Brenneman, James Chiang, Deepto Chakrabarty, Jerome Chenevez, Andrea Comastri, Francois

Dufour, Martin Elvis, Andrew C. Fabian, Duncan Farrah, Chris L. Fryer, Eric V. Gotthelf, Jonathan E. Grindlay, David J. Helfand, Roman Krivonos, David L. Meier, Jon M. Miller, Lorenzo Natalucci, Patrick Ogle, Eran O. Ofek, Andrew Ptak, Stephen P. Reynolds, Jane R. Rigby, Gianpiero Tagliaferri, Stephen E. Thorsett, Ezequiel Treister, and C. Megan Urry.
The Nuclear Spectroscopic Telescope Array (NuSTAR) High-energy X-Ray Mission.
ApJ, 770(2):103, June 2013.

[79] Siyu He, Yin Li, Yu Feng, Shirley Ho, Siamak Ravanbakhsh, Wei Chen, and Barnabás Póczos.
Learning to predict the cosmological structure formation.
Proceedings of the National Academy of Sciences, 116(28):13825–13832, 2019.

[80] Fumio Honma, Ryoji Matsumoto, and Shoji Kato.
Pulsational Instability of Relativistic Accretion Disks and Its Connection to the Periodic X-Ray Time Variabilily of NGC 6814.
PASJ, 44:529–535, October 1992.

[81] IceCube Collaboration, M. G. Aartsen, M. Ackermann, J. Adams, J. A. Aguilar, M. Ahlers, M. Ahrens, I. Al Samarai, D. Altmann, K. Andeen, T. Anderson, I. Ansseau, G. Anton, C. Argüelles, J. Auffenberg, S. Axani, H. Bagherpour, X. Bai, J. P. Barron, S. W. Barwick, V. Baum, R. Bay, J. J. Beatty, J. Becker Tjus, K. H. Becker, S. Ben-Zvi, D. Berley, E. Bernardini, D. Z. Besson, G. Binder, D. Bindig, E. Blaufuss, S. Blot, C. Bohm, M. Börner, F. Bos, S. Böser, O. Botner, E. Bourbeau, J. Bourbeau, F. Bradascio, J. Braun, M. Brenzke, H. P. Bretz, S. Bron, J. Brostean-Kaiser, A. Burgman, R. S. Busse, T. Carver, E. Cheung, D. Chirkin, A. Christov, K. Clark, L. Classen, S. Coenders, G. H. Collin, J. M. Conrad, P. Coppin, P. Correa, D. F. Cowen, R. Cross, P. Dave, M. Day, J. P. A. M. de André, C. De Clercq, J. J. DeLaunay, H. Dembinski, S. De Ridder, P. Desiati, K. D. de Vries, G. de Wasseige, M. de With, T. DeYoung, J. C. Díaz-Vélez, V. di Lorenzo, H. Dujmovic, J. P. Dumm, M. Dunkman, E. Dvorak, B. Eberhardt, T. Ehrhardt, B. Eichmann, P. Eller, P. A. Evenson, S. Fahey, A. R. Fazely, J. Felde, K. Filimonov, C. Finley, S. Flis, A. Franckowiak, E. Friedman, A. Fritz, T. K. Gaisser, J. Gallagher,

L. Gerhardt, K. Ghorbani, T. Glauch, T. Glüsenkamp, A. Goldschmidt, J. G. Gonzalez, D. Grant, Z. Griffith, C. Haack, A. Hallgren, F. Halzen, K. Hanson, D. Hebecker, D. Heereman, K. Helbing, R. Hellauer, S. Hickford, J. Hignight, G. C. Hill, K. D. Hoffman, R. Hoffmann, T. Hoinka, B. Hokanson-Fasig, K. Hoshina, F. Huang, M. Huber, K. Hultqvist, M. Hünnefeld, R. Hussain, S. In, N. Iovine, A. Ishihara, E. Jacobi, G. S. Japaridze, M. Jeong, K. Jero, B. J. P. Jones, P. Kalaczynski, W. Kang, A. Kappes, D. Kappesser, T. Karg, A. Karle, U. Katz, M. Kauer, A. Keivani, J. L. Kelley, A. Kheirandish, J. Kim, M. Kim, T. Kintscher, J. Kiryluk, T. Kittler, S. R. Klein, R. Koirala, H. Kolanoski, L. Köpke, C. Kopper, S. Kopper, J. P. Koschinsky, D. J. Koskinen, M. Kowalski, K. Krings, M. Kroll, G. Krückl, S. Kunwar, N. Kurahashi, T. Kuwabara, A. Kyriacou, M. Labare, J. L. Lanfranchi, M. J. Larson, F. Lauber, K. Leonard, M. Lesiak-Bzdak, M. Leuermann, Q. R. Liu, C. J. Lozano Mariscal, L. Lu, J. Lünemann, W. Luszczak, J. Madsen, G. Maggi, K. B. M. Mahn, S. Mancina, R. Maruyama, K. Mase, R. Maunu, K. Meagher, M. Medici, M. Meier, T. Menne, G. Merino, T. Meures, S. Miarecki, J. Micallef, G. Momenté, T. Montaruli, R. W. Moore, R. Morse, M. Moulai, R. Nahnhauer, P. Nakarmi, U. Naumann, G. Neer, H. Niederhausen, S. C. Nowicki, D. R. Nygren, A. Obertacke Pollmann, A. Olivas, A. O'Murchadha, E. O'Sullivan, T. Palczewski, H. Pandya, D. V. Pankova, P. Peiffer, J. A. Pepper, C. Pérez de los Heros, D. Pieloth, E. Pinat, M. Plum, P. B. Price, G. T. Przybylski, C. Raab, L. Rädel, M. Rameez, L. Rauch, K. Rawlins, I. C. Rea, R. Reimann, B. Relethford, M. Relich, E. Resconi, W. Rhode, M. Richman, S. Robertson, M. Rongen, C. Rott, T. Ruhe, D. Ryckbosch, D. Rysewyk, I. Safa, T. Sälzer, S. E. Sanchez Herrera, A. Sandrock, J. Sandroos, M. Santander, S. Sarkar, S. Sarkar, K. Satalecka, P. Schlunder, T. Schmidt, A. Schneider, S. Schoenen, S. Schöneberg, L. Schumacher, S. Sclafani, D. Seckel, S. Seunarine, J. Soedingrekso, D. Soldin, M. Song, G. M. Spiczak, C. Spiering, J. Stachurska, M. Stamatikos, T. Stanev, A. Stasik, R. Stein, J. Stettner, A. Steuer, T. Stezelberger, R. G. Stokstad, A. Stößl, N. L. Strotjohann, T. Stuttard, G. W. Sullivan, M. Sutherland, I. Taboada, J. Tatar, F. Tenholt, S. Ter-Antonyan, A. Terliuk, S. Tilav, P. A. Toale, M. N. Tobin, C. Toennis, S. Toscano, D. Tosi, M. Tselengidou, C. F. Tung, A. Turcati, C. F. Turley, B. Ty, E. Unger, M. Usner, J. Vandenbroucke, W. Van Driess-

che, D. van Eijk, N. van Eijndhoven, S. Vanheule, J. van Santen, E. Vogel, M. Vraeghe, C. Walck, A. Wallace, M. Wallraff, F. D. Wandler, N. Wandkowsky, A. Waza, C. Weaver, M. J. Weiss, C. Wendt, J. Werthebach, S. Westerhoff, B. J. Whelan, N. Whitehorn, K. Wiebe, C. H. Wiebusch, L. Wille, D. R. Williams, L. Wills, M. Wolf, J. Wood, T. R. Wood, K. Woschnagg, D. L. Xu, X. W. Xu, Y. Xu, J. P. Yanez, G. Yodh, S. Yoshida, T. Yuan, Fermi-LAT Collaboration, S. Abdollahi, M. Ajello, R. Angioni, L. Baldini, J. Ballet, G. Barbiellini, D. Bastieri, K. Bechtol, R. Bellazzini, B. Berenji, E. Bissaldi, R. D. Blandford, R. Bonino, E. Bottacini, J. Bregeon, P. Bruel, R. Buehler, T. H. Burnett, E. Burns, S. Buson, R. A. Cameron, R. Caputo, P. A. Caraveo, E. Cavazzuti, E. Charles, S. Chen, C. C. Cheung, J. Chiang, G. Chiaro, S. Ciprini, J. Cohen-Tanugi, J. Conrad, D. Costantin, S. Cutini, F. D'Ammando, F. de Palma, S. W. Digel, N. Di Lalla, M. Di Mauro, L. Di Venere, A. Domínguez, C. Favuzzi, A. Franckowiak, Y. Fukazawa, S. Funk, P. Fusco, F. Gargano, D. Gasparrini, N. Giglietto, M. Giomi, P. Giommi, F. Giordano, M. Giroletti, T. Glanzman, D. Green, I. A. Grenier, M. H. Grondin, S. Guiriec, A. K. Harding, M. Hayashida, E. Hays, J. W. Hewitt, D. Horan, G. Jóhannesson, M. Kadler, S. Kensei, D. Kocevski, F. Krauss, M. Kreter, M. Kuss, G. La Mura, S. Larsson, L. Latronico, M. Lemoine-Goumard, J. Li, F. Longo, F. Loparco, M. N. Lovellette, P. Lubrano, J. D. Magill, S. Maldera, D. Malyshev, A. Manfreda, M. N. Mazziotta, J. E. McEnery, M. Meyer, P. F. Michelson, T. Mizuno, M. E. Monzani, A. Morselli, I. V. Moskalenko, M. Negro, E. Nuss, R. Ojha, N. Omodei, M. Orienti, E. Orlando, M. Palatiello, V. S. Paliya, J. S. Perkins, M. Persic, M. Pesce-Rollins, F. Piron, T. A. Porter, G. Principe, S. Rainò, R. Rando, B. Rani, M. Razzano, S. Razzaque, A. Reimer, O. Reimer, N. Renault-Tinacci, S. Ritz, L. S. Rochester, P. M. Saz Parkinson, C. Sgrò, E. J. Siskind, G. Spandre, P. Spinelli, D. J. Suson, H. Tajima, M. Takahashi, Y. Tanaka, J. B. Thayer, D. J. Thompson, L. Tibaldo, D. F. Torres, E. Torresi, G. Tosti, E. Troja, J. Valverde, G. Vianello, M. Vogel, K. Wood, M. Wood, G. Zaharijas, MAGIC Collaboration, M. L. Ahnen, S. Ansoldi, L. A. Antonelli, C. Arcaro, D. Baack, A. Babić, B. Banerjee, P. Bangale, U. Barres de Almeida, J. A. Barrio, J. Becerra González, W. Bednarek, E. Bernardini, A. Berti, W. Bhattacharyya, A. Biland, O. Blanch, G. Bonnoli, A. Carosi, R. Carosi, G. Ceribella, A. Chat-

terjee, S. M. Colak, P. Colin, E. Colombo, J. L. Contreras, J. Cortina, S. Covino, P. Cumani, P. Da Vela, F. Dazzi, A. De Angelis, B. De Lotto, M. Delfino, J. Delgado, F. Di Pierro, A. Domínguez, D. Dominis Prester, D. Dorner, M. Doro, S. Einecke, D. Elsaesser, V. Fallah Ramazani, A. Fernández-Barral, D. Fidalgo, L. Foffano, K. Pfrang, M. V. Fonseca, L. Font, A. Franceschini, C. Fruck, D. Galindo, S. Gallozzi, R. J. García López, M. Garczarczyk, M. Gaug, P. Giammaria, N. Godinović, D. Gora, D. Guberman, D. Hadasch, A. Hahn, T. Hassan, M. Hayashida, J. Herrera, J. Hose, D. Hrupec, S. Inoue, K. Ishio, Y. Konno, H. Kubo, J. Kushida, D. Lelas, E. Lindfors, S. Lombardi, F. Longo, M. López, C. Maggio, P. Majumdar, M. Makariev, G. Maneva, M. Manganaro, K. Mannheim, L. Maraschi, M. Mariotti, M. Martínez, S. Masuda, D. Mazin, M. Minev, J. M. M, R. Mirzoyan, A. Moralejo, V. Moreno, E. Moretti, T. Nagayoshi, V. Neustroev, A. Niedzwiecki, M. Nievas Rosillo, C. Nigro, K. Nilsson, D. Ninci, K. Nishijima, K. Noda, L. Nogués, S. Paiano, J. Palacio, D. Paneque, R. Paoletti, J. M. Paredes, G. Pedaletti, M. Peresano, M. Persic, P. G. Prada Moroni, E. Prandini, I. Puljak, J. Rodriguez Garcia, I. Reichardt, W. Rhode, M. Ribó, J. Rico, C. Righi, A. Rugliancich, T. Saito, K. Satalecka, T. Schweizer, J. Sitarek, I. Šnidaric ´, D. Sobczynska, A. Stamerra, M. Strzys, T. Surić, M. Takahashi, F. Tavecchio, P. Temnikov, T. Terzić, M. Teshima, N. Torres-Albà, A. Treves, S. Tsujimoto, G. Vanzo, M. Vazquez Acosta, I. Vovk, J. E. Ward, M. Will, S, D. Zaric ´, AGILE Team, F. Lucarelli, M. Tavani, G. Piano, I. Donnarumma, C. Pittori, F. Verrecchia, G. Barbiellini, A. Bulgarelli, P. Caraveo, P. W. Cattaneo, S. Colafrancesco, E. Costa, G. Di Cocco, A. Ferrari, F. Gianotti, A. Giuliani, P. Lipari, S. Mereghetti, A. Morselli, L. Pacciani, F. Paoletti, N. Parmiggiani, A. Pellizzoni, P. Picozza, M. Pilia, A. Rappoldi, A. Trois, S. Vercellone, V. Vittorini, ASAS-SN Team, K. Z. Stanek, A. Franckowiak, C. S. Kochanek, J. F. Beacom, T. A. Thompson, T. W. S. Holoien, S. Dong, J. L. Prieto, B. J. Shappee, S. Holmbo, HAWC Collaboration, A. U. Abeysekara, A. Albert, R. Alfaro, C. Alvarez, R. Arceo, J. C. Arteaga-Velázquez, D. Avila Rojas, H. A. Ayala Solares, A. Becerril, E. Belmont-Moreno, A. Bernal, K. S. Caballero-Mora, T. Capistrán, A. Carramiñana, S. Casanova, M. Castillo, U. Cotti, J. Cotzomi, S. Coutiño de León, C. De León, E. De la Fuente, R. Diaz Hernandez, S. Dichiara, B. L. Dingus, M. A. DuVernois, J. C.

Díaz-Vélez, R. W. Ellsworth, K. Engel, D. W. Fiorino, H. Fleischhack, N. Fraija, J. A. García-González, F. Garfias, A. González Muñoz, M. M. González, J. A. Goodman, Z. Hampel-Arias, J. P. Harding, S. Hernandez, B. Hona, F. Hueyotl-Zahuantitla, C. M. Hui, P. Hüntemeyer, A. Iriarte, A. Jardin-Blicq, V. Joshi, S. Kaufmann, G. J. Kunde, A. Lara, R. J. Lauer, W. H. Lee, D. Lennarz, H. León Vargas, J. T. Linnemann, A. L. Longinotti, G. Luis-Raya, R. Luna-García, K. Malone, S. S. Marinelli, O. Martinez, I. Martinez-Castellanos, J. Martínez-Castro, H. Martínez-Huerta, J. A. Matthews, P. Miranda-Romagnoli, E. Moreno, M. Mostafá, A. Nayerhoda, L. Nellen, M. Newbold, M. U. Nisa, R. Noriega-Papaqui, R. Pelayo, J. Pretz, E. G. Pérez-Pérez, Z. Ren, C. D. Rho, C. Rivière, D. Rosa-González, M. Rosenberg, E. Ruiz-Velasco, E. Ruiz-Velasco, F. Salesa Greus, A. Sandoval, M. Schneider, H. Schoorlemmer, G. Sinnis, A. J. Smith, R. W. Springer, P. Surajbali, O. Tibolla, K. Tollefson, I. Torres, L. Villaseñor, T. Weisgarber, F. Werner, T. Yapici, Y. Gaurang, A. Zepeda, H. Zhou, J. D. Álvarez, H. E. S. S. Collaboration, H. Abdalla, E. O. Angüner, C. Armand, M. Backes, Y. Becherini, D. Berge, M. Böttcher, C. Boisson, J. Bolmont, S. Bonnefoy, P. Bordas, F. Brun, M. Büchele, T. Bulik, S. Caroff, A. Carosi, S. Casanova, M. Cerruti, N. Chakraborty, S. Chandra, A. Chen, S. Colafrancesco, I. D. Davids, C. Deil, J. Devin, A. Djannati-Ataï, K. Egberts, G. Emery, S. Eschbach, A. Fiasson, G. Fontaine, S. Funk, M. Füßling, Y. A. Gallant, F. Gaté, G. Giavitto, D. Glawion, J. F. Glicenstein, D. Gottschall, M. H. Grondin, M. Haupt, G. Henri, J. A. Hinton, C. Hoischen, T. L. Holch, D. Huber, M. Jamrozy, D. Jankowsky, F. Jankowsky, L. Jouvin, I. Jung-Richardt, D. Kerszberg, B. Khélifi, J. King, S. Klepser, W. Kluz ´niak, Nu. Komin, M. Kraus, J. Lefaucheur, A. Lemière, M. Lemoine-Goumard, J. P. Lenain, E. Leser, T. Lohse, R. López-Coto, M. Lorentz, I. Lypova, V. Marandon, G. Guillem Martí-Devesa, G. Maurin, A. M. W. Mitchell, R. Moderski, M. Mohamed, L. Mohrmann, E. Moulin, T. Murach, M. de Naurois, F. Niederwanger, J. Niemiec, L. Oakes, P. O'Brien, S. Ohm, M. Ostrowski, I. Oya, M. Panter, R. D. Parsons, C. Perennes, Q. Piel, S. Pita, V. Poireau, A. Priyana Noel, H. Prokoph, G. Pühlhofer, A. Quirrenbach, S. Raab, R. Rauth, M. Renaud, F. Rieger, L. Rinchiuso, C. Romoli, G. Rowell, B. Rudak, D. A. Sasaki, M. Sanchez, R. Schlickeiser, F. Schüssler, A. Schulz, U. Schwanke, M. Seglar-Arroyo, N. Shafi,

R. Simoni, H. Sol, C. Stegmann, C. Steppa, T. Tavernier, A. M. Taylor, D. Tiziani, C. Trichard, M. Tsirou, C. van Eldik, C. van Rensburg, B. van Soelen, J. Veh, P. Vincent, F. Voisin, S. J. Wagner, R. M. Wagner, A. Wierzcholska, R. Zanin, A. A. Zdziarski, A. Zech, A. Ziegler, J. Zorn, N. Żywucka, INTEGRAL Team, V. Savchenko, C. Ferrigno, A. Bazzano, R. Diehl, E. Kuulkers, P. Laurent, S. Mereghetti, L. Natalucci, F. Panessa, J. Rodi, P. Ubertini, Kiso Kanata, Subaru Observing Teams, T. Morokuma, K. Ohta, Y. T. Tanaka, H. Mori, M. Yamanaka, K. S. Kawabata, Y. Utsumi, T. Nakaoka, M. Kawabata, H. Nagashima, M. Yoshida, Y. Matsuoka, R. Itoh, Kapteyn Team, W. Keel, Liverpool Telescope Team, C. Copperwheat, I. Steele, Swift/NuSTAR Team, S. B. Cenko, D. F. Cowen, J. J. DeLaunay, P. A. Evans, D. B. Fox, A. Keivani, J. A. Kennea, F. E. Marshall, J. P. Osborne, M. Santander, A. Tohuvavohu, C. F. Turley, VERITAS Collaboration, A. U. Abeysekara, A. Archer, W. Benbow, R. Bird, A. Brill, R. Brose, M. Buchovecky, J. H. Buckley, V. Bugaev, J. L. Christiansen, M. P. Connolly, W. Cui, M. K. Daniel, M. Errando, A. Falcone, Q. Feng, J. P. Finley, L. Fortson, A. Furniss, O. Gueta, M. Hütten, O. Hervet, G. Hughes, T. B. Humensky, C. A. Johnson, P. Kaaret, P. Kar, N. Kelley-Hoskins, M. Kertzman, D. Kieda, M. Krause, F. Krennrich, S. Kumar, M. J. Lang, T. T. Y. Lin, G. Maier, S. McArthur, P. Moriarty, R. Mukherjee, D. Nieto, S. O'Brien, R. A. Ong, A. N. Otte, N. Park, A. Petrashyk, M. Pohl, A. Popkow, S. E. Pueschel, J. Quinn, K. Ragan, P. T. Reynolds, G. T. Richards, E. Roache, C. Rulten, I. Sadeh, M. Santander, S. S. Scott, G. H. Sembroski, K. Shahinyan, I. Sushch, S. Trépanier, J. Tyler, V. V. Vassiliev, S. P. Wakely, A. Weinstein, R. M. Wells, P. Wilcox, A. Wilhelm, D. A. Williams, B. Zitzer, VLA/B Team, A. J. Tetarenko, A. E. Kimball, J. C. A. Miller-Jones, and G. R. Sivakoff.

Multimessenger observations of a flaring blazar coincident with high-energy neutrino IceCube-170922A.

Science, 361(6398):eaat1378, July 2018.

[82] IceCube Collaboration, M. G. Aartsen, M. Ackermann, J. Adams, J. A. Aguilar, M. Ahlers, M. Ahrens, I. Al Samarai, D. Altmann, K. Andeen, T. Anderson, I. Ansseau, G. Anton, C. Argüelles, B. Arsioli, J. Auffenberg, S. Axani, H. Bagherpour, X. Bai, J. P. Barron, S. W. Barwick, V. Baum, R. Bay, J. J. Beatty, J. Becker Tjus, K. H.

Becker, S. BenZvi, D. Berley, E. Bernardini, D. Z. Besson, G. Binder, D. Bindig, E. Blaufuss, S. Blot, C. Bohm, M. Börner, F. Bos, S. Böser, O. Botner, E. Bourbeau, J. Bourbeau, F. Bradascio, J. Braun, M. Brenzke, H. P. Bretz, S. Bron, J. Brostean-Kaiser, A. Burgman, R. S. Busse, T. Carver, E. Cheung, D. Chirkin, A. Christov, K. Clark, L. Classen, S. Coenders, G. H. Collin, J. M. Conrad, P. Coppin, P. Correa, D. F. Cowen, R. Cross, P. Dave, M. Day, J. P. A. M. de André, C. De Clercq, J. J. DeLaunay, H. Dembinski, S. DeRidder, P. Desiati, K. D. de Vries, G. de Wasseige, M. de With, T. DeYoung, J. C. Díaz-Vélez, V. di Lorenzo, H. Dujmovic, J. P. Dumm, M. Dunkman, E. Dvorak, B. Eberhardt, T. Ehrhardt, B. Eichmann, P. Eller, P. A. Evenson, S. Fahey, A. R. Fazely, J. Felde, K. Filimonov, C. Finley, S. Flis, A. Franckowiak, E. Friedman, A. Fritz, T. K. Gaisser, J. Gallagher, L. Gerhardt, K. Ghorbani, P. Giommi, T. Glauch, T. Glüsenkamp, A. Goldschmidt, J. G. Gonzalez, D. Grant, Z. Griffith, C. Haack, A. Hallgren, F. Halzen, K. Hanson, D. Hebecker, D. Heereman, K. Helbing, R. Hellauer, S. Hickford, J. Hignight, G. C. Hill, K. D. Hoffman, R. Hoffmann, T. Hoinka, B. Hokanson-Fasig, K. Hoshina, F. Huang, M. Huber, K. Hultqvist, M. Hünnefeld, R. Hussain, S. In, N. Iovine, A. Ishihara, E. Jacobi, G. S. Japaridze, M. Jeong, K. Jero, B. J. P. Jones, P. Kalaczynski, W. Kang, A. Kappes, D. Kappesser, T. Karg, A. Karle, U. Katz, M. Kauer, A. Keivani, J. L. Kelley, A. Kheirandish, J. Kim, M. Kim, T. Kintscher, J. Kiryluk, T. Kittler, S. R. Klein, R. Koirala, H. Kolanoski, L. Köpke, C. Kopper, S. Kopper, J. P. Koschinsky, D. J. Koskinen, M. Kowalski, B. Krammer, K. Krings, M. Kroll, G. Krückl, S. Kunwar, N. Kurahashi, T. Kuwabara, A. Kyriacou, M. Labare, J. L. Lanfranchi, M. J. Larson, F. Lauber, K. Leonard, M. Lesiak-Bzdak, M. Leuermann, Q. R. Liu, C. J. Lozano Mariscal, L. Lu, J. Lünemann, W. Luszczak, J. Madsen, G. Maggi, K. B. M. Mahn, S. Mancina, R. Maruyama, K. Mase, R. Maunu, K. Meagher, M. Medici, M. Meier, T. Menne, G. Merino, T. Meures, S. Miarecki, J. Micallef, G. Momenté, T. Montaruli, R. W. Moore, R. Morse, M. Moulai, R. Nahnhauer, P. Nakarmi, U. Naumann, G. Neer, H. Niederhausen, S. C. Nowicki, D. R. Nygren, A. Obertacke Pollmann, A. Olivas, A. O'Murchadha, E. O'Sullivan, P. Padovani, T. Palczewski, H. Pandya, D. V. Pankova, P. Peiffer, J. A. Pepper, C. Pérez de los Heros, D. Pieloth, E. Pinat, M. Plum, P. B. Price, G. T. Przybylski, C. Raab, L. Rädel, M. Rameez, K. Rawl-

ins, I. C. Rea, R. Reimann, B. Relethford, M. Relich, E. Resconi, W. Rhode, M. Richman, S. Robertson, M. Rongen, C. Rott, T. Ruhe, D. Ryckbosch, D. Rysewyk, I. Safa, N. Sahakyan, T. Sälzer, S. E. Sanchez Herrera, A. Sandrock, J. Sandroos, M. Santander, S. Sarkar, S. Sarkar, K. Satalecka, P. Schlunder, T. Schmidt, A. Schneider, S. Schoenen, S. Schöneberg, L. Schumacher, S. Sclafani, D. Seckel, S. Seunarine, J. Soedingrekso, D. Soldin, M. Song, G. M. Spiczak, C. Spiering, J. Stachurska, M. Stamatikos, T. Stanev, A. Stasik, J. Stettner, A. Steuer, T. Stezelberger, R. G. Stokstad, A. Stößl, N. L. Strotjohann, T. Stuttard, G. W. Sullivan, M. Sutherland, I. Taboada, J. Tatar, F. Tenholt, S. Ter-Antonyan, A. Terliuk, S. Tilav, P. A. Toale, M. N. Tobin, C. Toennis, S. Toscano, D. Tosi, M. Tselengidou, C. F. Tung, A. Turcati, C. F. Turley, B. Ty, E. Unger, M. Usner, J. Vandenbroucke, W. Van Driessche, D. van Eijk, N. van Eijndhoven, S. Vanheule, J. van Santen, E. Vogel, M. Vraeghe, C. Walck, A. Wallace, M. Wallraff, F. D. Wandler, N. Wandkowsky, A. Waza, C. Weaver, M. J. Weiss, C. Wendt, J. Werthebach, S. Westerhoff, B. J. Whelan, N. Whitehorn, K. Wiebe, C. H. Wiebusch, L. Wille, D. R. Williams, L. Wills, M. Wolf, J. Wood, T. R. Wood, K. Woschnagg, D. L. Xu, X. W. Xu, Y. Xu, J. P. Yanez, G. Yodh, S. Yoshida, and T. Yuan.
Neutrino emission from the direction of the blazar TXS 0506+056 prior to the IceCube-170922A alert.
Science, 361(6398):147–151, July 2018.

[83] Adam R. Ingram and Sara E. Motta.
A review of quasi-periodic oscillations from black hole X-ray binaries: Observation and theory.
New Astronomy Reviews, 85:101524, September 2019.

[84] Xin Jin, Yanxia Zhang, Jingyi Zhang, Yongheng Zhao, Xue-bing Wu, and Dongwei Fan.
Efficient selection of quasar candidates based on optical and infrared photometric data using machine learning.
MNRAS, 485(4):4539–4549, June 2019.

[85] Guolin Ke, Qi Meng, Thomas Finley, Taifeng Wang, Wei Chen, Weidong Ma, Qiwei Ye, and Tie-Yan Liu.
Lightgbm: A highly efficient gradient boosting decision tree.
In *NIPS*, 2017.

[86] A. Keivani, K. Murase, M. Petropoulou, D. B. Fox, S. B. Cenko, S. Chaty, A. Coleiro, J. J. DeLaunay, S. Dimitrakoudis, P. A. Evans, J. A. Kennea, F. E. Marshall, A. Mastichiadis, J. P. Osborne, M. Santander, A. Tohuvavohu, and C. F. Turley.
A Multimessenger Picture of the Flaring Blazar TXS 0506+056: Implications for High-energy Neutrino Emission and Cosmic-Ray Acceleration.
ApJ, 864:84, September 2018.

[87] J. G. Kirk, F. M. Rieger, and A. Mastichiadis.
Particle acceleration and synchrotron emission in blazar jets.
A&A, 333:452–458, May 1998.

[88] T. M. Kneiske, T. Bretz, K. Mannheim, and D. H. Hartmann.
Implications of cosmological gamma-ray absorption. II. Modification of gamma-ray spectra.
A&A, 413:807–815, January 2004.

[89] Kovačević, M. , G. Chiaro, S. Cutini, and G. Tosti.
Optimizing neural network techniques in classifying Fermi-LAT gamma-ray sources.
MNRAS, 490(4):4770–4777, December 2019.

[90] M. Kovačević, G. Chiaro, S. Cutini, and G. Tosti.
Classification of blazar candidates of uncertain type from the Fermi LAT 8-yr source catalogue with an artificial neural network.
MNRAS, 493(2):1926–1935, April 2020.

[91] Pankaj Kushwaha, Arkadipta Sarkar, Alok C. Gupta, Ashutosh Tripathi, and Paul J. Wiita.
A possible γ-ray quasi-periodic oscillation of $\sim$314 days in the blazar OJ 287.
MNRAS, 499(1):653–658, November 2020.

[92] Julien Lefaucheur and Santiago Pita.
Research and characterisation of blazar candidates among the Fermi/LAT 3FGL catalogue using multivariate classifications.
A&A, 602:A86, June 2017.

[93] H. Z. Li, Y. G. Jiang, T. F. Yi, D. F. Guo, X. Chen, H. M. Zhang, Q. G. Gao, F. W. Lu, and J. Y. Ren.
The radio and γ-ray variability analysis of S5 0716+714.
Ap&SS, 363(3):45, March 2018.

[94] Shang Li, Zi-Qing Xia, Yun-Feng Liang, Neng-Hui Liao, and Yi-Zhong Fan.
Fast γ-Ray Variability in Blazars beyond Redshift 3.
ApJ, 853(2):159, February 2018.

[95] B. Lott, L. Escande, S. Larsson, and J. Ballet.
An adaptive-binning method for generating constant-uncertainty/constant-significance light curves with Fermi-LAT data.
A&A, 544:A6, August 2012.

[96] A. Mainzer, J. Bauer, R. M. Cutri, T. Grav, J. Masiero, R. Beck, P. Clarkson, T. Conrow, J. Dailey, P. Eisenhardt, B. Fabinsky, S. Fajardo-Acosta, J. Fowler, C. Gelino, C. Grillmair, I. Heinrichsen, M. Kendall, J. Davy Kirkpatrick, F. Liu, F. Masci, H. McCallon, C. R. Nugent, M. Papin, E. Rice, D. Royer, T. Ryan, P. Sevilla, S. Sonnett, R. Stevenson, D. B. Thompson, S. Wheelock, D. Wiemer, M. Wittman, E. Wright, and L. Yan.
Initial Performance of the NEOWISE Reactivation Mission.
ApJ, 792(1):30, September 2014.

[97] K. Mannheim.
The proton blazar.
A&A, 269:67–76, March 1993.

[98] K. Mannheim and P. L. Biermann.
Photomeson production in active galactic nuclei.
A&A, 221:211–220, September 1989.

[99] L. Maraschi, G. Ghisellini, and A. Celotti.
A Jet Model for the Gamma-Ray–emitting Blazar 3C 279.
ApJL, 397:L5, September 1992.

[100] L. Marcotulli, V. S. Paliya, M. Ajello, A. Kaur, D. H. Hartmann, D. Gasparrini, J. Greiner, A. Rau, P. Schady, M. Baloković, D. Stern, and G. Madejski.

High-redshift Blazars through NuSTAR Eyes.
ApJ, 839(2):96, April 2017.

[101] E. Massaro, A. Tramacere, M. Perri, P. Giommi, and G. Tosti.
Log-parabolic spectra and particle acceleration in blazars. III. SSC emission in the TeV band from Mkn501.
A&A, 448(3):861–871, March 2006.

[102] J. R. Mattox, D. L. Bertsch, J. Chiang, B. L. Dingus, S. W. Digel, J. A. Esposito, J. M. Fierro, R. C. Hartman, S. D. Hunter, G. Kanbach, D. A. Kniffen, Y. C. Lin, D. J. Macomb, H. A. Mayer-Hasselwander, P. F. Michelson, C. von Montigny, R. Mukherjee, P. L. Nolan, P. V. Ramanamurthy, E. Schneid, P. Sreekumar, D. J. Thompson, and T. D. Willis.
The Likelihood Analysis of EGRET Data.
ApJ, 461:396, April 1996.

[103] D. Mazin and M. Raue.
New limits on the density of the extragalactic background light in the optical to the far infrared from the spectra of all known TeV blazars.
A&A, 471(2):439–452, August 2007.

[104] Jonathan C. McKinney, Alexander Tchekhovskoy, and Roger D. Blandford.
General relativistic magnetohydrodynamic simulations of magnetically choked accretion flows around black holes.
MNRAS, 423(4):3083–3117, July 2012.

[105] Manuel Meyer, Jeffrey D. Scargle, and Roger D. Blandford.
Characterizing the Gamma-Ray Variability of the Brightest Flat Spectrum Radio Quasars Observed with the Fermi LAT.
ApJ, 877(1):39, May 2019.

[106] R. Middei, P. Giommi, M. Perri, S. Turriziani, N. Sahakyan, Y. L. Chang, C. Leto, and F. Verrecchia.
The first hard X-ray spectral catalogue of Blazars observed by NuSTAR.
MNRAS, 514(3):3179–3190, August 2022.

[107] A. Mücke and R. J. Protheroe.
A proton synchrotron blazar model for flaring in Markarian 501.

Astroparticle Physics, 15(1):121–136, March 2001.

[108] A. Mücke, R. J. Protheroe, R. Engel, J. P. Rachen, and T. Stanev.
BL Lac objects in the synchrotron proton blazar model.
Astroparticle Physics, 18:593–613, March 2003.

[109] K. Murase, F. Oikonomou, and M. Petropoulou.
Blazar Flares as an Origin of High-energy Cosmic Neutrinos?
ApJ, 865:124, October 2018.

[110] Aditya Narendra, Spencer James Gibson, Maria Giovanna Dainotti, Malgorzata Bogdan, Agnieszka Pollo, Ioannis Liodakis, Artem Poliszczuk, and Enrico Rinaldi.
Predicting the Redshift of Gamma-Ray Loud AGNs Using Supervised Machine Learning. II.
ApJSS, 259(2):55, April 2022.

[111] P. Padovani, D. M. Alexander, R. J. Assef, B. De Marco, P. Giommi, R. C. Hickox, G. T. Richards, V. Smolčić, E. Hatziminaoglou, V. Mainieri, and M. Salvato.
Active galactic nuclei: what's in a name?
A&AR, 25(1):2, August 2017.

[112] Paolo Padovani and Paolo Giommi.
The connection between x-ray- and radio-selected BL Lacertae objects.
ApJ, 444:567–581, 1995.

[113] Vaidehi S. Paliya.
The High-redshift Blazar S5 0836+71: A Broadband Study.
ApJ, 804(1):74, May 2015.

[114] Vaidehi S. Paliya, M. Ajello, H. M. Cao, M. Giroletti, Amanpreet Kaur, Greg Madejski, Benoit Lott, and D. Hartmann.
Blazars at the Cosmic Dawn.
ApJ, 897(2):177, July 2020.

[115] Vaidehi S. Paliya, M. Ajello, R. Ojha, R. Angioni, C. C. Cheung, K. Tanada, T. Pursimo, P. Galindo, I. R. Losada, L. Siltala, A. A. Djupvik, L. Marcotulli, and D. Hartmann.
Detection of a Gamma-Ray Flare from the High-redshift Blazar DA 193.
ApJ, 871(2):211, February 2019.

[116] Vaidehi S. Paliya, M. L. Parker, A. C. Fabian, and C. S. Stalin.
Broadband Observations of High Redshift Blazars.
ApJ, 825(1):74, July 2016.

[117] P. Peñil, A. Domínguez, S. Buson, M. Ajello, J. Otero-Santos, J. A. Barrio, R. Nemmen, S. Cutini, B. Rani, A. Franckowiak, and E. Cavazzuti.
Systematic Search for γ-Ray Periodicity in Active Galactic Nuclei Detected by the Fermi Large Area Telescope.
ApJ, 896(2):134, June 2020.

[118] P. Peñil, A. Domínguez, S. Buson, M. Ajello, J. Otero-Santos, J. A. Barrio, R. Nemmen, S. Cutini, B. Rani, A. Franckowiak, and E. Cavazzuti.
Systematic Search for γ-Ray Periodicity in Active Galactic Nuclei Detected by the Fermi Large Area Telescope.
ApJ, 896(2):134, June 2020.

[119] Donald P. Percival.
On estimation of the wavelet variance.
Biometrika, 82(3):619–631, 1995.

[120] M. Petropoulou and A. Mastichiadis.
Bethe-Heitler emission in BL Lacs: filling the gap between X-rays and γ-rays.
MNRAS, 447(1):36–48, February 2015.

[121] Elena Pian, Giuseppe Vacanti, Gianpiero Tagliaferri, Gabriele Ghisellini, Laura Maraschi, Aldo Treves, C. Megan Urry, Fabrizio Fiore, Paolo Giommi, Eliana Palazzi, Lucio Chiappetti, and Rita M. Sambruna.
BeppoSAX Observations of Unprecedented Synchrotron Activity in the BL Lacertae Object Markarian 501.
ApJL, 492(1):L17–L20, January 1998.

[122] Patryk Pjanka, Andrzej A. Zdziarski, and Marek Sikora.
The power and production efficiency of blazar jets.
MNRAS, 465(3):3506–3514, March 2017.

[123] T. S. Poole, A. A. Breeveld, M. J. Page, W. Landsman, S. T. Holland, P. Roming, N. P. M. Kuin, P. J. Brown, C. Gronwall, S. Hunsberger, S. Koch, K. O. Mason, P. Schady, D. vanden Berk, A. J. Blustin,

P. Boyd, P. Broos, M. Carter, M. M. Chester, A. Cucchiara, B. Hancock, H. Huckle, S. Immler, M. Ivanushkina, T. Kennedy, F. Marshall, A. Morgan, S. B. Pandey, M. de Pasquale, P. J. Smith, and M. Still.
Photometric calibration of the Swift ultraviolet/optical telescope.
MNRAS, 383(2):627–645, January 2008.

[124] D. A. Prokhorov and A. Moraghan.
A search for cyclical sources of γ-ray emission on the period range from days to years in the Fermi-LAT sky.
MNRAS, 471(3):3036–3042, November 2017.

[125] B. Rani, B. Lott, T. P. Krichbaum, L. Fuhrmann, and J. A. Zensus.
Constraining the location of rapid gamma-ray flares in the flat spectrum radio quasar 3C 273.
A&A, 557:A71, September 2013.

[126] J. N. Reeves, M. J. L. Turner, P. J. Bennie, K. A. Pounds, A. Short, P. T. O'Brien, Th. Boller, M. Kuster, and A. Tiengo.
The first XMM-Newton spectrum of a high redshift quasar - PKS 0537-286.
A&A, 365:L116–L121, January 2001.

[127] Helena X. Ren, Matteo Cerruti, and Narek Sahakyan.
Quasi-periodic oscillations in the γ-ray light curves of bright active galactic nuclei.
arXiv e-prints, page arXiv:2204.13051, April 2022.

[128] Frank M. Rieger.
On the Geometrical Origin of Periodicity in Blazar-type Sources.
ApJL, 615(1):L5–L8, November 2004.

[129] C. Righi, F. Tavecchio, and L. Pacciani.
A multiwavelength view of BL Lac neutrino candidates.
MNRAS, 484(2):2067–2077, April 2019.

[130] N. Sahakyan.
Lepto-hadronic γ-Ray and Neutrino Emission from the Jet of TXS 0506+056.
ApJ, 866:109, October 2018.

[131] N. Sahakyan.
Origin of the multiwavelength emission of PKS 0502+049.
A&A, 622:A144, February 2019.

[132] N. Sahakyan.
Broad-band study of high-synchrotron-peaked BL Lac object 1ES 1218+304.
MNRAS, 496(4):5518–5527, July 2020.

[133] N. Sahakyan.
Modelling the broad-band emission of 3C 454.3.
MNRAS, 504(4):5074–5086, July 2021.

[134] N. Sahakyan, V. Baghmanyan, and D. Zargaryan.
Fermi-LAT observation of nonblazar AGNs.
A&A, 614:A6, June 2018.

[135] N. Sahakyan and S. Gasparyan.
High energy gamma-ray emission from PKS 1441+25.
MNRAS, 470(3):2861–2869, September 2017.

[136] N. Sahakyan and P. Giommi.
The strange case of the transient HBL blazar 4FGL J1544.3-0649.
MNRAS, 502(1):836–844, March 2021.

[137] N. Sahakyan and P. Giommi.
A 13-yr-long broad-band view of BL Lac.
MNRAS, 513(3):4645–4656, July 2022.

[138] N. Sahakyan, P. Giommi, P. Padovani, M. Petropoulou, D. Bégué, B. Boccardi, and S. Gasparyan.
A multi-messenger study of the blazar PKS 0735+178: a new major neutrino source candidate.
arXiv e-prints, page arXiv:2204.05060, April 2022.

[139] N. Sahakyan, D. Israyelyan, and G. Harutyunyan.
A Multiwavelength Study of Distant Blazar PKS 0537-286.
Astrophysics, November 2020.

[140] N. Sahakyan, D. Israyelyan, G. Harutyunyan, S. Gasparyan, V. Vardanyan, and M. Khachatryan.

Modelling the time variable spectral energy distribution of the blazar CTA 102 from 2008 to 2022.
MNRAS, 517(2):2757–2768, December 2022.

[141] N. Sahakyan, D. Israyelyan, G. Harutyunyan, M. Khachatryan, and S. Gasparyan.
Multiwavelength study of high-redshift blazars.
MNRAS, 498(2):2594–2613, October 2020.

[142] D. Salvetti, G. Chiaro, G. La Mura, and D. J. Thompson.
3FGLzoo: classifying 3FGL unassociated Fermi-LAT γ-ray sources by artificial neural networks.
MNRAS, 470(2):1291–1297, September 2017.

[143] A. Sandrinelli, S. Covino, and A. Treves.
Gamma-Ray and Optical Oscillations in PKS 0537-441.
ApJ, 820(1):20, March 2016.

[144] A. Sandrinelli, S. Covino, A. Treves, et al.
Quasi-periodicities of BL Lacertae objects.
A&A, 615:A118, July 2018.

[145] A. Sandrinelli, S. Covino, A. Treves, E. Lindfors, C. M. Raiteri, K. Nilsson, L. O. Takalo, R. Reinthal, A. Berdyugin, V. Fallah Ramazani, V. Kadenius, T. Tuominen, P. Kehusmaa, R. Bachev, and A. Strigachev.
Gamma-ray and optical oscillations of 0716+714, MRK 421, and BL Lacertae.
A&A, 600:A132, April 2017.

[146] Arkadipta Sarkar, Alok C. Gupta, Varsha R. Chitnis, and Paul J. Wiita.
Multiwaveband quasi-periodic oscillation in the blazar 3C 454.3.
MNRAS, 501(1):50–61, February 2021.

[147] P. M. Saz Parkinson, H. Xu, P. L. H. Yu, D. Salvetti, M. Marelli, and A. D. Falcone.
Classification and Ranking of Fermi LAT Gamma-ray Sources from the 3FGL Catalog using Machine Learning Techniques.
ApJ, 820(1):8, March 2016.

[148] A. Shukla, K. Mannheim, S. R. Patel, J. Roy, V. R. Chitnis, D. Dorner, A. R. Rao, G. C. Anupama, and C. Wendel.
Short-timescale γ-Ray Variability in CTA 102.
ApJL, 854(2):L26, February 2018.

[149] J. Siebert, M. Matsuoka, W. Brinkmann, M. Cappi, T. Mihara, and T. Takahashi.
ASCA observations of high redshift quasars.
A&A, 307:8, March 1996.

[150] Marek Sikora, Mitchell C. Begelman, and Martin J. Rees.
Comptonization of Diffuse Ambient Radiation by a Relativistic Jet: The Source of Gamma Rays from Blazars?
ApJ, 421:153, January 1994.

[151] A. Sillanpaa, S. Haarala, M. J. Valtonen, B. Sundelius, and G. G. Byrd.
OJ 287: Binary Pair of Supermassive Black Holes.
ApJ, 325:628, February 1988.

[152] Emanuele Sobacchi, Mattia C. Sormani, and Antonio Stamerra.
A model for periodic blazars.
MNRAS, 465(1):161–172, February 2017.

[153] Mariusz Tarnopolski, Natalia Żywucka, Volodymyr Marchenko, and Javier Pascual-Granado.
A Comprehensive Power Spectral Density Analysis of Astronomical Time Series. I. The Fermi-LAT Gamma-Ray Light Curves of Selected Blazars.
ApJSS, 250(1):1, September 2020.

[154] M. Tavani, A. Cavaliere, Pere Munar-Adrover, and A. Argan.
The Blazar PG 1553+113 as a Binary System of Supermassive Black Holes.
ApJ, 854(1):11, February 2018.

[155] J. Timmer and M. Koenig.
On generating power law noise.
Astronomy and Astrophysics, 300:707, August 1995.

[156] Christopher Torrence and Gilbert P. Compo.

A Practical Guide to Wavelet Analysis.
Bulletin of the American Meteorological Society, 79(1):61–78, 01 1998.

[157] A. Tramacere, P. Giommi, M. Perri, F. Verrecchia, and G. Tosti.
Swift observations of the very intense flaring activity of Mrk 421 during 2006. I. Phenomenological picture of electron acceleration and predictions for MeV/GeV emission.
A&A, 501(3):879–898, July 2009.

[158] A. Tramacere, E. Massaro, and A. M. Taylor.
Stochastic Acceleration and the Evolution of Spectral Distributions in Synchro-Self-Compton Sources: A Self-consistent Modeling of Blazars' Flares.
ApJ, 739(2):66, October 2011.

[159] Andrea Tramacere.
JetSeT: Numerical modeling and SED fitting tool for relativistic jets, September 2020.

[160] C. Megan Urry and Paolo Padovani.
Unified Schemes for Radio-Loud Active Galactic Nuclei.
Publications of the Astronomical Society of the Pacific, 107:803, September 1995.

[161] C. Megan Urry and Paolo Padovani.
Unified Schemes for Radio-Loud Active Galactic Nuclei.
Publications of the Astronomical Society of the Pacific, 107:803, September 1995.

[162] M. J. Valtonen, K. Nilsson, C. Villforth, H. J. Lehto, L. O. Takalo, E. Lindfors, A. Sillanpää, V. P. Hentunen, S. Mikkola, S. Zola, M. Drozdz, D. Koziel, W. Ogloza, M. Kurpinska-Winiarska, M. Siwak, M. Winiarski, J. Heidt, M. Kidger, T. Pursimo, J. H. Wu, X. Zhou, K. Sadakane, D. Marchev, M. Nissinen, P. Niarchos, A. Liakos, K. Gazeas, S. Dogru, G. Poyner, M. Dietrich, R. Assef, D. Atlee, J. Bird, D. DePoy, J. Eastman, M. Peeples, J. Prieto, L. Watson, J. Yee, A. Mattingly, and J. Ohlert.
Tidally Induced Outbursts in OJ 287 during 2005-2008.
ApJ, 698(1):781–785, June 2009.

[163] J. Valverde and J. Forman.
Fermi-LAT detection of renewed gamma-ray activity from the FSRQ PKS 0537-286.
The Astronomer's Telegram, 15405:1, May 2022.

[164] G. G. Wang, J. T. Cai, and J. H. Fan.
A Possible 3 yr Quasi-periodic Oscillation in γ-Ray Emission from the FSRQ S5 1044+71.
ApJ, 929(2):130, April 2022.

[165] A. E. Wright, B. A. Peterson, D. L. Jauncey, and J. J. Condon.
PKS 0537-286: a high-redshift QSO with an extreme Lyman-continuum cutoff.
ApJL, 226:L61–L64, December 1978.

[166] Yijun Xu, Weirong Huang, Hui Deng, Ying Mei, and Feng Wang.
A Hybrid Method of Accurate Classification for Blazars of Uncertain Type in Fermi-LAT Catalogs.
ApJ, 895(2):133, June 2020.

[167] Jianping Yang, Gang Cao, Bing Zhou, and Longhua Qin.
Quasi-periodic Oscillation of Blazar PKS 1424-418 in γ-Ray Band.
Publications of the Astronomical Society of the Pacific, 133(1020):024101, February 2021.

[168] Shenbang Yang, Dahai Yan, Pengfei Zhang, Benzhong Dai, and Li Zhang.
Gaussian Process Modeling Fermi-LAT γ-Ray Blazar Variability: A Sample of Blazars with γ-Ray Quasi-periodicities.
ApJ, 907(2):105, February 2021.

[169] Zhenping Yi, Zesheng Chen, Jingchang Pan, Lili Yue, Yuxiang Lu, Jia Li, and A. Li Luo.
An Efficient Spectral Selection of M Giants Using XGBoost.
ApJ, 887(2):241, December 2019.

[170] G. Zamorani, J. P. Henry, T. Maccacaro, H. Tananbaum, A. Soltan, Y. Avni, J. Liebert, J. Stocke, P. A. Strittmatter, R. J. Weymann, M. G. Smith, and J. J. Condon.
X-ray studies of quasars with the Einstein Observatory II.

ApJ, 245:357–374, April 1981.

[171] D. Zargaryan, S. Gasparyan, V. Baghmanyan, and N. Sahakyan.
Comparing 3C 120 jet emission at small and large scales.
A&A, 608:A37, December 2017.

[172] Haiyun Zhang, Dahai Yan, Pengfei Zhang, Shenbang Yang, and Li Zhang.
A Quasi-periodic Oscillation in the γ-Ray Emission from the Non-blazar Active Galactic Nucleus PKS 0521-36.
ApJ, 919(1):58, September 2021.

[173] Peng-Fei Zhang, Da-Hai Yan, Neng-Hui Liao, and Jian-Cheng Wang.
Revisiting Quasi-periodic Modulation in γ-Ray Blazar PKS 2155-304 with Fermi Pass 8 Data.
ApJ, 835(2):260, February 2017.

[174] Peng-Fei Zhang, Da-Hai Yan, Jia-Neng Zhou, Yi-Zhong Fan, Jian-Cheng Wang, and Li Zhang.
A γ-ray Quasi-periodic Modulation in the Blazar PKS 0301-243?
ApJ, 845(1):82, August 2017.

[175] Peng-Fei Zhang, Da-Hai Yan, Jia-Neng Zhou, Jian-Cheng Wang, and Li Zhang.
Searching for Quasiperiodic Modulations in γ-Ray Active Galactic Nuclei.
ApJ, 891(2):163, March 2020.

[176] Jianeng Zhou, Zhongxiang Wang, Liang Chen, et al.
A 34.5 day quasi-periodic oscillation in γ-ray emission from the blazar PKS 2247-131.
Nature Communications, 9:4599, November 2018.

[177] Ke-Rui Zhu, Shi-Ju Kang, and Yong-Gang Zheng.
Searching for AGN and pulsar candidates in 4FGL unassociated sources using machine learning.
Research in Astronomy and Astrophysics, 21(1):015, January 2021.

[178] N. Żywucka, M. Tarnopolski, V. Marchenko, and J. Pascual-Granado.
Comprehensive power spectral density analysis of the Fermi-LAT gamma-ray light curves of selected blazars.

In *High Energy Astrophysics in Southern Africa 2021*, page 8, May 2022.